

The lateral photovoltage scanning method to probe  
spatial inhomogeneities in semiconductors: a  
joined numerical and experimental investigation.

Von der Fakultät 1 - MINT - Mathematik, Informatik, Physik,  
Elektro- und Informationstechnik  
der Brandenburgischen Technischen Universität Cottbus–  
Senftenberg  
genehmigte Dissertation  
zur Erlangung des akademischen Grades eines  
Dr. rer. nat.

vorgelegt von

**Stefan Kayser**

Geboren am 11.04.1988 in Hennigsdorf

Vorsitzender:	Prof. Dr. Götz Seibold
Gutachter:	Prof. Dr. Thomas Schröder
Gutachter:	Prof. Dr. Christian Wenger
Gutachter:	Prof. Dr. Michele Virgilio

Tag der mündlichen Prüfung: Montag den 08. 02. 2021



## Abstract

The Lateral-Photovoltage-Scanning-Method (LPS) operates well for Si, Ge and  $\text{Si}_{1-x}\text{-Ge}_x$  for an analysis in defect regions below one part per million, where Secondary Ion Mass Spectroscopy (SIMS) or X-Ray Fluorescence (XRF) signals fall below its detection limit. [Tau55, ALR<sup>+</sup>05, SLR96]

Although LPS is well established since 1999, it is still poorly investigated. We used a computational simulation finite volume (FVM) approach, solving the van-Roosbroeck equations in three dimensions using a MULTifrontal Massively Parallel sparse direct Solver MUMPS. The signal transport is simulated by solving the Maxwell equations in two dimension for different sample geometries.

It could be shown that a typical LPS-measurement is distorted due to the samples geometry (except cuboid). This distortion can be simulated, understood and recalculated, as discussed for trapezoidal or cylindrical samples. Also using the signal generation simulation of this measurement technique it can be shown, that the measurement signal is convoluted depending on the inherent minority charge carrier life time reducing the local resolution. An investigation of the local resolution were made using a Gaussian function as the convolution function of this method. A comparison of simulations to real measurements was discussed on silicon samples with boron implantation pattern.

In 1955 Tauc already stated that the bulk photovoltaic effect, causative for the LPS measurement set-up, could be used detecting any quantity, which affects the band structure of a semiconductor. As strain is coupled to the conduction and valence band profiles by the deformation potential theory by van-de-Walle [Van89], we investigated the possibility to detect strain variations using LPS simulations. For an n-type Si sample with an on-top stressor stripe (silicon-nitride) the strain distribution in Si got calculated by finite element simulation (FEM) using solid mechanics module. By directly converting the strain profile to a single conduction and valence band, FVM LPS simulations were performed. It could be shown, that the LPS voltage can be connected to hole traps caused by the conduction and valence band profile. Therefore we can finally conclude, that the LPS measurement set-up is suitable measuring conduction and valence band variations caused by strain.



## Zusammenfassung

Die Lateral-Photovoltage-Scanning-Methode (LPS) ist zur Analyse der Dotierstoffvariationen von Si, Ge und  $\text{Si}_{1-x}\text{-Ge}_x$  in Bereichen unter 1 ppm geeignet, in denen die Signale der Sekundärionen-Massenspektroskopie (SIMS) oder der Röntgenfluoreszenz (XRF) unter ihre Nachweisgrenze fallen. [Tau55, ALR<sup>+</sup>05, SLR96]

Obwohl die LPS-Methode seit 1999 etabliert ist, ist sie noch immer wenig erforscht. Um diese Methode besser zu verstehen, wurde mithilfe eines Finite-Volumen-Ansatz (FVM) simuliert und die van-Roosbroeck-Gleichungen in drei Dimensionen mit einem MULTifrontal Massively Parallel Sparse Solver MUMPS gelöst. Um den Signaltransport zu simulieren, werden die Maxwell-Gleichungen in zwei Dimensionen für verschiedene Probengeometrien gelöst. Durch diese Arbeit konnte gezeigt werden, dass eine typische LPS-Messung aufgrund der Probengeometrie (mit Ausnahme von quaderförmigen Proben) verzerrt ist. Diese Verzerrung kann simuliert, verstanden und berechnet werden, sowie für trapezförmige oder zylindrische Proben diskutiert. Mithilfe der Simulation zur Signalzeugung dieser Messtechnik wird gezeigt, dass das Messsignal in Abhängigkeit von der inhärenten Minoritätsladungsträger-Lebensdauer gefaltet ist, was die lokale Auflösung reduziert. Eine Untersuchung der lokalen Auflösung wurde unter Verwendung einer Gaußfunktion als Faltungsfunktion durchgeführt. Ein Vergleich von Simulationen mit realen Messungen wurde an Siliciumproben mit Bor-Implantationsmuster diskutiert.

Bereits 1955 stellte Tauc fest, dass der photovoltaische Effekt, der für das LPS-Signal ursächlich ist, zum Nachweis jeder Größe, die die Bandstruktur eines Halbleiters beeinflusst, genutzt werden kann. Da die Dehnung durch Deformationspotentiale nach von van-de-Walle [Van89] an die Leitungs- und Valenzbandprofile gekoppelt ist, wurde die Möglichkeit untersucht, Dehnungsvariationen mit Hilfe von LPS-Simulationen zu detektieren. Für eine n-Typ-Si-Probe mit aufgesetzten Verspannungstreifen (Siliciumnitrid) wurde die Dehnungsverteilung in Si mittels Finite-Elemente-Simulation (FEM) unter Verwendung eines Festkörpermechanik-Moduls in COMSOL berechnet. Durch direkte Umwandlung des Dehnungsprofils in ein einziges Leitungs- und Valenzband wurden FVM-LPS-Simulationen durchgeführt. Es konnte gezeigt werden, dass die LPS-Spannung mit Lochfallen verbunden werden kann, die durch das Leitungs- und Valenzbandprofil verursacht werden. Daraus lässt sich schließen, dass der LPS-Messaufbau geeignet wäre, Leitungs- und Valenzbandvariationen durch Dehnung hervorgerufen zu messen.



*"The great tragedy of Science - the slaying of a beautiful hypothesis by an ugly fact."*

**T. H. Huxley 1870**





# Symbol Explanation

Symbol	Explanation	Unit
$U_{LPS}$	LPS-voltage	nV
$U_{LPS,2D}$	simulated LPS-voltage by Maxwell equation	nV
$n, p$	electron-, hole density	$\text{cm}^{-3}$
$N_D^+, N_A^-$	density of ionized impurities	$\text{cm}^{-3}$
$N_D, N_A$	density of donors and acceptors	$\text{cm}^{-3}$
$\sigma$	conductivity	S/m
$\rho$	resistivity	$\Omega\text{cm}$
$E_F$	Fermi energy	eV
$E_C, E_V$	conduction/valence band energy	eV
$N_C, N_V$	effective DOS of conduction, valence band	$\text{cm}^{-3}$
$n_i$	intrinsic carrier density	$\text{cm}^{-3}$
$T$	temperature	300 K
$k_B$	Boltzmann constant	J/K
$v_{th}$	thermal velocity	cm/s
$q$	electric charge	C
$\epsilon$	dielectric constant	F/m
$\Phi$	electric potential	V
$G$	generation rate	$\text{s}^{-1}\text{cm}^{-3}$
$R$	recombination rate	$\text{s}^{-1}\text{cm}^{-3}$
$J_n, J_p$	current density of electrons, holes	$\text{Am}^{-2}$
$J_{Drift}, J_{Diff}, J_{Th}$	current density caused by drift, diffusion and thermal gradient	$\text{Am}^{-2}$
$\mu_{n,p}$	mobility of electrons, holes	$\text{cm}^2/\text{Vs}$
$D_{n,p}$	electric displacement field of electrons, holes	$\text{As}/\text{m}^2$
$R_{Dir}, R_{SRH}, R_{Aug}$	rate for direct, Shockley-Read-Hall and Auger recombination	$\text{s}^{-1}\text{cm}^{-3}$
$C_{Dir}$	direct recombination factor	$\text{m}^3/\text{s}$
$\gamma_{n,p}$	electron, hole degeneracy factor	.
$\tau_{n,p}$	electron, hole life time	$\mu\text{s}$
$n_d, p_d$	electron, hole density of state $d$	$\text{cm}^{-3}$
$E_i$	intrinsic energy level	eV
$E_T$	trap energy level	eV
$C_{Aug}^{n,p}$	Auger recombination factor for electrons, holes	$\text{m}^6/\text{s}$
$f_{mod}$	modulation frequency	kHz
$\Omega$	volume in 3D space	.
$\mathbf{u}$	continuously differentiable vector field	.
$\partial\Omega$	surface of volume $\Omega$	.

Symbol	Explanation	Unit
$R_{\text{Dir}}, R_{\text{SRH}}, R_{\text{Aug}}$	rate for direct, Shockley-Read-Hall and Auger recombination	$\text{s}^{-1}\text{cm}^{-3}$
$\mathbf{n}$	outward pointing normal field	.
$S$	surface of volume $\Omega$	.
$\omega$	part of volume $\Omega$	.
$P(x_f, y_f)$	coordinates of the laser spot	mm
$\sigma_{\text{eq}}$	equilibrium conductivity	S/m
$S(x)$	LPS signal	V
$g$	associated inverse Fermi integral	.
$\mathcal{F}_{1/2}$	Fermi-Dirac integral	.
$\Phi_{\text{n,p}}$	quasi Fermi potentials for electrons and holes	V
$\mathcal{R}$	reflectivity	.
$\mathcal{L}$	laser beam shape function	$\text{m}^{-3}$
$\sigma_L$	standard deviation of the Gaussian beam profile	$\mu\text{m}$
$F_1$	Fletcher mobility coefficients	$\text{m}^{-1}\text{V}^{-1}\text{s}^{-1}$
$F_2$	Fletcher mobility coefficients	$\text{m}^{-2}$
$\hat{L}, \hat{U}$	upper (lower) triangulation matrix	.
$f_{\text{mod}}$	modulation frequency of LPS measurement set-up	1 kHz
$\Gamma_{1,2}$	boundaries definition	.
$\Phi_{\text{in}}$	assumed dipole strength	V
$U_{\text{eff}}$	effective value of the LPS voltage	nV
$\gamma$	convolution function	.
$\boldsymbol{\sigma}_{ij}$	stress tensor	GPa
$\boldsymbol{\varepsilon}_{ij}$	strain tensor	.
$\Delta$	spin orbit split off energy	eV
$Y$	Young's modulus	GPa
$G$	Shear modulus	GPa
$\eta$	Poissons's ratio	.
$\Xi, b, d$	deformation potentials	eV
$\gamma_{1,2,3}$	Luttinger parameters	.

# List of Figures

1.1.	Historical data showing the number of transistors (in a logarithmic scale) fabricated in a dense integrated circuit as a function of time. The solid curve indicates, that the number of transistors double every 18 month. . . . .	1
1.2.	The "International Technology Roadmap for Semiconductors" (ITRS) illustrates the combined need of miniaturization of the digital functions ("More Moore") and functional diversification ("More than Moore"). [Rei17]. . . . .	3
2.1.	Band edge (a) and resistivity (b) profile along the $x$ -direction of an inhomogeneously doped $n$ -type semiconductor bar with negligible transverse thicknesses. In the top panel the illuminated portion of the sample (red vertical arrow) and the drifting of excess electrons (filled circles) and holes (empty circles) are also sketched. (c) Photogenerated voltage difference $U$ as a function of the excitation spot position $x_f$ (blue curve). The red curve represents the spatial integrated photovoltage (see text). . . . .	10
2.2.	1D adopted sample geometry. The redish region represents the illuminated portion of the sample; the two contacts are placed at the sample boundaries and are marked as a and a'. . . . .	11
2.3.	Photo-voltage in units of the saturation value $U_{\max}$ calculated as a function of $\Delta\sigma/\sigma(b)$ for different values of the $\sigma(c)/\sigma(b)$ ratio. . . . .	16
2.4.	Left panel: cuboid domain for a SCDE system. Right panel: discretization with an homogeneous cuboid grid of the domain shown in the left plot. . . . .	20
2.5.	Schematic of a cuboid sub-domain $\omega_i$ taken from [Mad07]. Capital and lower letters are used to define the six orthogonal lines passing through P, and the intersection points with the corresponding boundary surface, respectively. . . .	21
2.6.	Face contributions to the flux of the $-\nabla\Phi$ vector field outgoing through the surface of the $\omega_i$ volume.[Mad07]. . . . .	22
2.7.	Central difference scheme to evaluate the potential derivative at the central point of the $E$ cuboid face. The $P$ and $E$ letters represent the $x$ -coordinates of the central points of the neighbor cuboids. . . . .	22
2.8.	Scheme of the closed circuit configuration. . . . .	26
2.9.	Schematics of a representative non-uniform grid used in the simulations. Notice that the grid is more dense in the neighbor of the focal point set at $P(4.5\text{ mm}, 0\text{ mm}, 0\text{ mm})$ . The $y \rightarrow -y$ is exploited to reduce the simulated volume by a factor of two. . . .	27
2.10.	Scheme of the used LPS-measurement set-up. . . . .	28
2.11.	Graphical interface for the software which controls the acquisition of the LPS voltage signal. The windows allows to set $\Delta x$ , $\Delta y$ , $\Delta t$ , and the dimensions of the scanned area. . . . .	29
2.12.	Scheme of the lock-in-technique used to improve the signal-to-noise ratio when acquiring the photogenerated voltage signal. $S_{\text{in}}$ is the lock-in modulation signal and the $\Delta U$ is the modulated voltage difference between the rim contacts. . . .	29

2.13.	Left panel: LPS map of a FZ-Si n-type sample showing the typical striation pattern associated to the solid-liquid interface dynamics. Central panel: LPS map with a tracked isolines marked in red. Right panel: simulated temperature field (K) at a given time during the growth process. The bold isoline represents the position of the solid-liquid interface. Additionally shown in grey is the heat inducing inductor coil. . . . .	30
3.1.	Left panel: result of the simulations of the LPS-voltage relative to the parameter $a$ . Right panel: dependency of the simulated LPS-voltages on the slope parameter $a$ [KLB18]. . . . .	32
3.2.	Left panel: behaviour of the offset with respect to the width of the simulated sample. Right panel: dependency of the offset from the sample thickness. After an increase related to the penetration depth of the laser, a decreasing trend is visible [KLB18]. . . . .	33
3.3.	Two dimensional model of the LPS measurement setup. The silicon sample is marked blue, the copper wires in grey and the inner resistance of the volt meter in red. . . . .	34
3.4.	Dependency of $U_{LPS,2D}$ on the dipole strength represented as $\Phi_{in}$ . . . . .	35
3.5.	A constant behaviour is visible, which reveals a linear dependency of $\Phi_{in}$ to $U_{LPS,2D}$ . . . . .	35
3.6.	Sketch of the current lines in the Si sample. Here the colour of the vector indicates the strength of the current at that area. Red is set to a high and dark blue to low current. . . . .	36
3.7.	Dependency of the two dimensional LPS-voltage with respect to the Cu conductivity normalized by the Si conductivity. . . . .	37
3.8.	Dependency of the two dimensional LPS-voltage with respect to the doping concentration of Si. Here also a constant ratio of the conductances Cu/Si was kept constant. . . . .	37
3.9.	Dependency of the two-dimensional simulated LPS-voltage with respect to the sample length (black) and the sample width (red). . . . .	38
3.10.	Left panel: dependency of the simulated two dimensional LPS-voltage with respect to the sample width. Right panel:dependency of the simulated two dimensional LPS-voltage with respect to the sample thickness. . . . .	39
3.11.	Dependency of the two-dimensional LPS-voltage with respect to the observation (focal) point $P(x_f, y_f)$ . . . . .	40
3.12.	Left panel: Sketch of the wafer-like sample set-up used in the two-dimensional model. Right panel: a line scan along the horizontal diameter was simulated (black). A LPS-voltage normalized by the local sample width is shown in red. . . . .	40
3.13.	Analysis of a trapezoidal sample (hatched in grey). The dependency of the two-dimensional LPS-voltage with respect to the observation (focal) point $P(x_f, y_f)$ . The red dots represents a set of date, which is normalized by the local sample width. . . . .	41
3.14.	Left panel: LPS-measurement of an $80 \Omega\text{cm}$ sample with a rectangular shape $100\text{mm} \times 120\text{mm}$ . Right panel: a repetition ( $(18\text{mm} - 100\text{mm}) \times 120\text{mm}$ ) of this measurement after cutting. . . . .	41
3.15.	Comparison measured LPS-voltage with respect to the sample geometry. The red curve contains a simulated correction factor described in figure (3.13). . . . .	42
3.16.	Left panel: Sketch of a rectangular sample with a point-like contact. Right panel: horizontal line scan of the simulated LPS-voltage. . . . .	43

3.17. Left panel: Vertical line scan of the simulated LPS-Voltage. Right panel: dependency of the two-dimensional simulated LPS-voltage depending on the path length, the shortest way connecting the focal points to both contacts. . . . .	43
3.18. Left panel: $U_{LPS}$ line scan along the $x$ -direction from sample S0 at different laser power, as reported in the legend. Right panel: simulated LPS voltage obtained from the dopant profile derived from the $U_{LPS}$ signal shown in the left plot (red curve 5.5 mW). For comparison also the profile of the dopant gradient used in the simulation is reported (black curve). . . . .	44
3.19. Measured and simulated LPS voltages at fixed $(x_f, y_f)$ as a function of laser pump power for the unimplanted n-type sample. . . . .	45
4.1. SIMS measurement of the $^{11}\text{B}$ -concentration in the implanted region after RTA for sample with $N_{A,2} = 1 \times 10^{17} \text{ cm}^{-3}$ , compared with the theoretical estimation discussed in the text (red curve). Notice that the model properly describes the asymmetry of the measured profile. . . . .	48
4.2. SIMS map of the in-plane doping profile acquired after RTA with a penetration depth of 650 nm i.e. at the peak of the $z$ -distribution of dopants, from a sample with nominal stripe width of 90 $\mu\text{m}$ . In the inset a line scan along the transverse $x$ -direction is also shown together with a rectangular profile convolved with Gaussian functions with $\sigma = 12 \text{ nm}$ (red curve). . . . .	49
4.3. LPS grey-scale map acquired from sample S1. Darker (brighter) grey corresponds to negative (positive) $x$ -component of the gradient of the dopant concentration. . . . .	49
4.4. LPS (black curve) and integrated (red curve) LPS signal from S2 measured at $P = 20 \text{ mW}$ . The blue dashed curve refers to the right vertical axis and represents the doping profile. The large period modulation of the LPS signal and its inter-stripe secondary peaks are to be attributed to the contribution stemming from background doping striation. . . . .	51
4.5. Integrated LPS signal measured in S2 at different laser powers $P$ (symbols). The solid red curve represents the dopant profile, convolved with a Gaussian function whose standard deviation $\sigma_s$ is used as a fitting parameter to estimate the LPS spatial resolution at $P = 2.4 \text{ mW}$ . . . . .	51
4.6. Top left panel: numeric excess electron and hole carrier distribution, simulated at different pump powers for sample S2 with laser spot at the left interface of an implanted region ( $x = 64 \text{ nm}$ ) i.e. in a region featuring a positive dopant gradient. The distributions are plotted as a function of $x$ at the sample surface along a line passing through the laser spot center. Top right panel: the corresponding distribution for the net excess charge density $\rho = p - n$ are shown for $P = 2.5 \times 10^{-3} \text{ mW} - 2.5 \text{ mW}$ (left vertical axis) together with the static acceptor density $N_A$ (black curve, right vertical axis). Bottom left panel: valence (red curve) and conduction (black curve) band edge at equilibrium. Bottom right panel: the photoinduced screening field, calculated as a function of $x$ is shown.	53

4.7.	Left and central panel: numerical simulation for sample S1 of line scans along the $x$ -direction of the integrated LPS voltage, calculated at different laser powers. Plot (left panel) and (central panel) have been obtained considering and neglecting variations in the dopant concentration profile occurring along the $z$ -direction, respectively (see text). For each pump power, the dashed line represents the best fitting convolution of the in-plane dopant distribution (black solid line) with a Gaussian function whose standard deviation $\sigma_s$ is reported in the legend. Right panel: standard deviation for the best fitting Gaussian convolution profile as a function of the pump power, obtained with a $z$ -dependent doping profile (red circles) and with an homogeneous doping profile along the $z$ -direction (black square). The inset displays the $z$ -dependence of the dopant concentration used in the simulations. . . . .	54
4.8.	Measured (full symbols) and simulated (empty symbols) LPS resolution $\sigma_s$ as a function of pump power $P$ for S1 (black squares), S2 (red circles), and S3 (blue triangle). . . . .	55
5.1.	Scheme of the strain tensor notation system chosen for the further investigations	58
5.2.	Behaviour of the strain dependent band edge variation for HH, LH and SO as a function of strain in the hypothesis of in-plane biaxial strain (left panel) and [001] uniaxial strain (right panel). . . . .	62
5.3.	Left panel: effect of non-diagonal component $\epsilon_{xz}$ on valence band edge in presence of [001] tensile strain of 1 %. The dashed lines are the valence band edge for [001] tensile strain of 1 % without non-diagonal components, the full lines are the band profile with diagonal components. Right panel: resulting band edge variations depending on biaxial strain. . . . .	63
5.4.	Top panel: three dimensional sample geometry assuming an infinite length in the $y$ -direction. Bottom left panel: strain trace field generated by a $\text{Si}_3\text{N}_4$ stressor with 4 GPa initial in plane stress on top of a Si sample. Bottom right panel: strain profiles of the dominant $\epsilon_{xx}$ component evaluated at different depth levels.	65
5.5.	Single strain components for the geometry taken 100 nm below the top surface.	66
5.6.	Behavior of strain profile (top), conduction band (middle) and valence band (down) at both sides of the stripe. . . . .	67
5.7.	Left panel: LPS-voltage profile (left axis) and the therefore simulated effective valence band edge profile extracted at $z = 100\text{nm}$ . Right panel: LPS-voltage depending on the laser pump power at $x = 1.3705\text{mm}$ . . . . .	67
5.8.	Left panel: effective valence band edge profile for a (non)-illuminated sample marked in red (black). Right panel: calculated LPS-voltage with respect to the laser spot position. . . . .	68
5.9.	Charge carrier densities for electrons (holes) are shown in the left (right) panel.	69
5.10.	Left panel: net charge carrier concentration profiles. Right panel: shows the difference between the shown net charge carrier distributions. . . . .	69
5.11.	Left panel: lateral electric field. Right panel: its integration. . . . .	70
5.12.	Left panel: calculated LPS-voltage with respect to the laser spot position in quasi one dimensional sample geometry. As an inlay a semi-Gaussian profile is shown. Right panel: calculated LPS-voltage with respect to the laser spot position in two dimensional sample geometry. . . . .	72

# Table of Contents

<b>Preface</b>	<b>I</b>
Abstract . . . . .	I
Zusammenfassung . . . . .	III
Aphorism . . . . .	V
Symbol Explanation . . . . .	VII
List of Figures . . . . .	XII
Table of Contents . . . . .	XIV
<b>1. Microelectronics Today</b>	<b>1</b>
1.1. “More Moore” vs./and “More than Moore” . . . . .	1
1.2. Material Quality Improvements . . . . .	4
1.3. The Lateral Photovoltage Scanning Method - LPS . . . . .	6
<b>2. Theoretical Background and LPS set-up</b>	<b>9</b>
2.1. An intuitive picture of the Bulk Photovoltaic Effect . . . . .	9
2.2. Analytical theory of the bulk Photovoltaic Effect . . . . .	11
2.3. Numerical Model Equations . . . . .	15
2.4. Discretization procedures . . . . .	19
2.5. Sample Preparation and Measurement Set-up . . . . .	27
<b>3. Signal Generation and Transmission</b>	<b>31</b>
3.1. Proof of Principle of the Signal Generation Program . . . . .	31
3.2. Signal Transmission . . . . .	33
3.3. Doping striations and model validation . . . . .	43
3.4. Conclusion . . . . .	45
<b>4. Local Resolution of the LPS Measurements</b>	<b>47</b>
4.1. Sample preparation and SIMS characterization . . . . .	47
4.2. Spatial resolution of the LPS measurements . . . . .	50
4.3. Conclusion . . . . .	55
<b>5. Strain-field Measurement Simulation</b>	<b>57</b>
5.1. Theoretical Model . . . . .	58
5.2. Results and Discussion . . . . .	64
5.3. Conclusion . . . . .	72
<b>Postface</b>	<b>75</b>
Summary and Outlook . . . . .	75
Acknowledgement . . . . .	79
Scientific Visibility . . . . .	79

<b>Bibliography</b>	<b>81</b>
<b>Appendices</b>	<b>89</b>
A. Notes to the main text . . . . .	90
B. Code . . . . .	94





Despite its long lasting accuracy, the Moore prediction was always anticipated to lose validity due to limitations inherent to the process technology (as for instance the maximum achievable resolution for lithographic processing) or to the approaching of fundamental physical barriers when the device size becomes comparable to the atomistic scales. Indeed, since the 1970s, the general expectation has always been that the technology roadmap would be sustainable for just ten more years. But there's life in the old dog yet.

As a matter of fact in the present time Moore's Law has not lost validity yet. Targetting a reduction of power, performance, area and cost (PPAC) per unit of component, research efforts in the field has allowed to keep Moore's Law on track, following the so called "more Moore" approach. In particular the main goal is the transistor miniaturization, keeping the compatibility with the Complementary Metal-Oxide-Semiconductor (CMOS) standard. In this way, scaling down it's size, the maximum number of transistors hosted in a single chip can be increased. As a consequence systems on a single chip (SoC) featuring increasing degree of complexity can reach the market, as for instance witnessed by the recent release of the Raspberry Pi [RC19].

Following this miniaturization trend, current CMOS transistors feature gate length of the order of 7 nm [WLC<sup>+</sup>17], which corresponds to an array of just 13 atoms in a silicon lattice. Therefore, at this length scale further miniaturization seems to be limited by the atomic size and to an uncontrolled arrangement of their position inducing by the lithographic processes, which moreover has a resolution limit harshly below 10 nm [CYD<sup>+</sup>09]. Hence, it is not surprising that Intel and Nvidia among others proclaimed recently the end of Moore's Law [Tib19].

The approaching of these fundamental limits has driven research efforts toward alternative directions: "In the 21<sup>st</sup> century, the new challenge is not how many transistors can be built on a single chip, but rather how to integrate diverse circuits together predictably, harmoniously and cost effectively" was already stated in 2000 at the Bell Laboratories [Tai00]. These diverse integrated circuits has to be connected and are therefore build in packages, applying to the so called System-in-Package (SiP) procedure. This kind of technologies are usually referred as the "More than Moore"<sup>2</sup> approach since in this cases the performance increase does not rely on down-scaling but is related to diversification of transistors and circuits. According to ITRS reports the "More than Moore" approach typically allows non-digital-functionalities (e.g., sensors, actuators, RF communicators) to migrate from the system on board level to a particular package level (SiP) or chip-level (SoC).

The actual landscape of the semiconductor industry can be represented by the scheme in Fig. 1.2, where the two lines of development high light the fruitful coexistence of the "More Moore" and "More than Moore" paradigm. In other words, in the next future higher value hybrid systems are expected to be realized by the combination of SiP and SoC systems thanks to research progress in miniaturization and diversification.

---

<sup>2</sup>IRTS2009

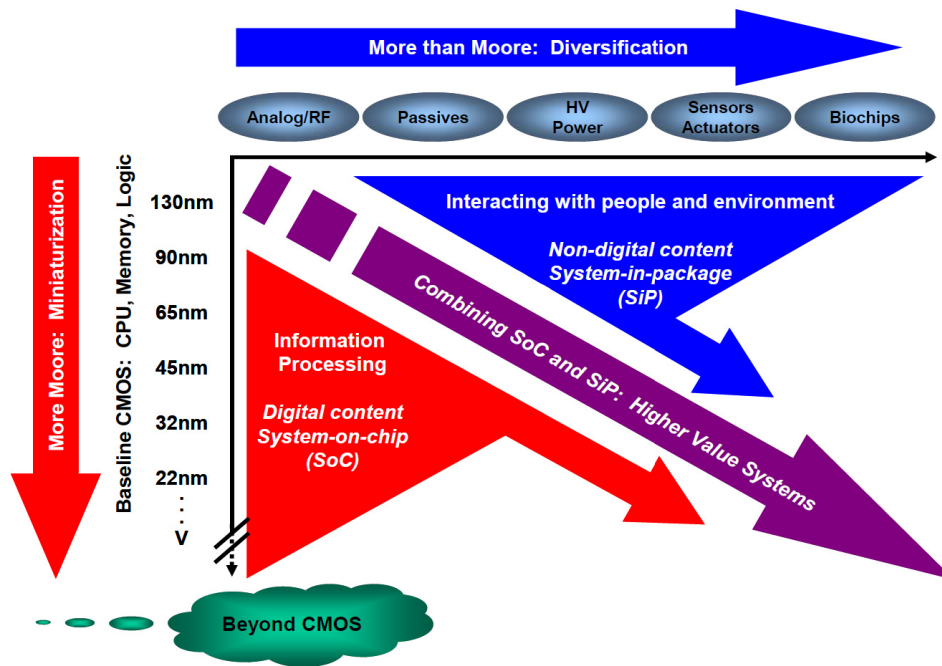


Fig. 1.2: The "International Technology Roadmap for Semiconductors" (ITRS) illustrates the combined need of miniaturization of the digital functions ("More Moore") and functional diversification ("More than Moore"). [Rei17].

The realization of the objectives indicated in Fig. 1.2 places a plethora of challenges in material science. Of particular relevance for the presented contest, are those related to the improvement of the substrate material. From this perspective, Silicon has always been the workhorse in the CMOS technology. Despite silicon substrates have been introduced more than 70 years ago, driven by advances in PPAC, the growth of the crystal material, the substrate preparation and the associated characterization techniques are still an active research field. In parallel, and in line with the "More than Moore" approach also a lot of new substrate materials are actively investigated, thus increasing the set of available wafers to chose from, when a specific functionality is targeted. For instance, high power devices are expected to outperform when grown on  $\beta$ -Ga<sub>2</sub>O<sub>3</sub> [BGW18, HJ18] thanks to the higher break down voltage with respect to silicon featured by this new material. As another example, chips embedding photonic functionalities require III-V based substrates due to the poor optical emission properties of group IV crystals [SPZ07].

Of course of paramount importance in this field is the capability of realizing large atomically flat substrates featuring an high quality crystal material with an excellent degree of spatial uniformity. To this aim we stress that lattice defects, such as misfits dislocations or atomic impurity related to (un)intentional background doping, may be electrically active and then influence the transistor performances, especially when their size is reduced. For instance, it is has been shown that random doping fluctuations occurring in the gate material of an ensemble of < 20 nm transistors, cause a critical broadening of the threshold voltage distribution [BM16, Toc10]. Moreover, due to local differences in the thermal conductivity associated to an inhomogeneous material, temperature fluctuation may occur along the gate channel, negatively impacting on the sub threshold leakages.

## 1.2. Material Quality Improvements

Motivated by the quest for an increase in substrate quality, the need to explore novel semiconductor materials, or the cost benefits associated to an enlargement of the wafer area, well established crystal growth techniques, as for instance the Czochralski approach (Cz), which dates 1918 [Czo18], still attract a considerable amount of research efforts, in line with the PPAC objectives. As a matter of fact, nowadays, beside continuously improving traditional growth approaches, innovative procedures are also explored. To this aim new growth machine concepts are introduced, and sophisticated numerical simulations of the crystal dynamics developed to achieve a deeper understanding of the growth process [DFR13, DBSR17]. Finally, research effort are also oriented to improve the structural characterization techniques used to assess the crystal quality and its impact on the electrical or thermal properties [ACC<sup>+</sup>06, PDLV<sup>+</sup>99, SB02, OMTO92, LR97].

Research in crystal growth is historically well established in Berlin, as witnessed by the presence of the Leibniz Institute for Crystal Growth, a member of the Forschungsverbund Berlin and a leading player in this field, contributing to keep alive the legacy of Czochralski which settled in the city from Poland at the beginning of the XX century to develop his famous method.

To better appreciate the relevance of the Cz-approach, it's worth to remember that nowadays more than 95 % of the silicon single crystals are grown using this technique [Zul01], and diameters up to 450 mm are routinely achieved [LK11]. According to the Cz-method, a seed crystal is dipped in a melt and slowly pulled out toward a lower temperature region to cool down in order to crystallize with a lattice orientation controlled by the seed. During this process, the temperature fields, the rotation and the pulling velocity, together with the overall melt volume can be tuned in order to optimize the crystal volume and quality [TUT92, KEWH89].

Since the melt and the seed are usually made by the same material, a finite temperature difference between the melt (liquid phase) and the seed crystal (solid phase) must be maintained during the growth for thermodynamic reasons, in order to maintain these two separate phases. This temperature gradient induce a thermal shock in the fuse material which generates lattice dislocations that in the case of silicon propagate mainly along the [110] crystal direction. With the scope of exploiting this preferential orientation, in 1958 William Dash engineered the final crystal shape placing a neck in the growth direction [Das59]. As a result the defect lines were driven toward the surface and dislocation free silicon single crystals were obtained.

Another technological issue, limiting the crystal quality in the Cz-growth approach is related to the interaction of the melt with the surrounding crucible. As a matter of fact, due to this interaction, crucible particle, usually oxygen and carbon aggregates are incorporated into the melt. Consequently, Cz-grown materials feature higher concentration of these two elements with respect to crystals grown by means of alternative crucible free approaches [Shi86]. When the concentration of crucible material in the melt is high enough formation of oxygen and carbon precipitates are observed, which negatively affect the electrical transport properties, limiting the mobility and lowering the charge carrier life time [New00]. Due to the current quality standard required by the semiconductor industry, managing this negative effect represents today an open challenge, even after more than one hundred years from the introduction of the Cz-technique [RNM<sup>+</sup>17].

Mainly to overcome this limitation, a different growth approach for silicon crystals has been proposed and pioneered in the '50 by Pfann [Pfa52] in the effort to avoid the presence of the

crucible. Soon after Theuerer further developed this approach, and patented it in 1962 with the name of "Floating-Zone-Method" (FZ) [The62]. The core idea is that, a vertical rod made of high pure poly crystalline material is slowly pulled down towards the center of an horizontal heating coil. In a neighbour of the coil, the high temperature field partially melts the silicon rod. The melt, which surrounds the external surface, flows downward without any contact interaction with the coil, and subsequently, when it reaches a lower temperature region below the coil plane solidifies. Combining the FZ-approach with the necking technique introduced by Dash's virtually dislocation free single crystals has been obtained [Syl62]. To figure out the high level of maturity of this technology, one should consider that nowadays this kind of material, with diameter up to 200 mm, is commercially available [DNH<sup>+</sup>14]. On the other hand the floating zone technique also represents the method of choice to achieve record purity crystals material needed for very specific applications. For instance we mention that meteorologic applications, that IKZ FZ-Si<sup>28</sup> crystal are used to define the Avogadro constant [BPRA10] and the mass unit since May 2019. However, the main drawback of the FZ-approach, which prevents its extensive application, is related to the need of high quality feed rod making the technique too expensive for the mass market [Zul94].

To avoid both the need for an expensive feed material and the contamination caused by the direct interaction with a crucible material, a novel method to grow silicon crystals, named "SiGrEt", has been proposed by the Leibniz Institute for Crystal Growth in 2017 [Lor19, DMZ<sup>+</sup>17]. As in the classic Cz-approach, the crystal is pulled out from a furnace using a seed attached to a rod moving upward. In this case however, the crucible is filled with commercial silicon granulate which is kept in the solid phase everywhere expect for the central zone. It follows that contamination in the melt region are avoid since the surrounding solid region prevents a direct interaction of the fuse with the crucible walls. To achieve this goal, an high frequency electromagnetic coil inductor is placed close to the external surface of the crucible in order to produce an appropriate temperature field by a proper engineering of the inductor shape and penetration depth of the electro magnetic radiation. The development of such inductor requires numerical simulations to estimate the resulting temperature field since the local temperature depend in a complex manner also on the growth kinetics (which of course is influenced by the e.m. field) and the other growth parameters, such as the rod translation and rotation velocity. The validation of this numerical estimates and more in general the optimization of the SiGrEt approach, demand for an accurate experimental technique able to measure the temperature field during the growth. Notice that the demonstration of such technique would be of great value in a broader context, since also the optimization of the Cz- and FZ-method would benefit from the capability of measuring with sufficient spatial resolution the growth temperature.

To probe the temperature field one can try to asses some physical quantity which influences in a significant manner the crystallization process and at the same time is critically dependent on the  $T$  spatial variation. Variations in the background doping concentration fulfill both these properties since "temperature fluctuations at the solid-liquid interface lead to unsteady growth and backmelting. These result in microscopic impurity variations in the crystal, also called [...] striations" [Zul94]. Detecting these microscopic impurity variation by a fast and cheap mapping technique, would allow to reconstruct the spatial profile of the solid-liquid interface which in turn contains the desired information about the temperature field. Moreover, the measured solid-liquid interface profile could be also direct benchmarked against numerical data obtained simulating the whole growth kinetics, thus allowing to validate the theoretical models [KNL<sup>+</sup>91, CO98, VFM07]. Finally, a precise, fast, cheap and possible non-destructive measurement of the background doping profile is valuable by itself since it can be used to asses the degree of spatial homogeneity in the final wafer material.

### 1.3. The Lateral Photovoltage Scanning Method - LPS

Traditionally, the local doping concentration is measured assessing its effect on the electrical resistivity after the crystal has been sawed into individual wafers or into a set of longitudinal cuts by a four-point-probe resistivity set-up [Val54]. The main drawback of this technique is the relatively poor spatial resolution (few mm [Oss19]) and the rather long acquisition time. Despite lateral resolution can be improved to approach the micrometer scale by using spreading resistance imaging, this goal is achieved at the expenses of even longer acquisition times [MD66, Dic66]. Moreover since the probes are put in contact with the wafer surface, the measurement may alter the surface properties. As an alternative to map the dopant distribution in the wafer material, the secondary ion mass spectroscopy (SIMS) approach can be also adopted. However, this technique is intrinsically destructive and its sensitivity in detecting light mass dopants as for instance boron, is limited to the rather high density of about  $N_A > 1 \times 10^{15} \text{ cm}^{-3}$ . [CNF<sup>+</sup>85].

To overcome these limitations, an optoelectrical measurement procedure, known as the **Lateral-Photovoltage-Scanning Method (LPS)**, has been proposed in 1997 [LR97], targeting the non-destructive detection at room temperature of doping inhomogeneities at the wafer-scale. Interestingly, beside being very cost-effective and fast, this tabletop set-up is especially suitable for low dopant concentrations ( $10^{12} \text{ cm}^{-3} - 10^{16} \text{ cm}^{-3}$ ), thus considerably extending the range accessible by SIMS.

The LPS technique exploits the phenomenon of the bulk photovoltaic effect, first analytically investigated by Tauc in 1955 [Tau55]. When a semiconductor layer, featuring a doping concentration gradient, is illuminated by an electromagnetic radiation of an appropriate wavelength, the photogenerated electrons and holes randomly diffuse and at the same time drift under the action of an electric field. In fact, the concentration gradient induces a spatially varying internal electric field, which sets a preferred direction for the movement of the charge carriers. In turn this drift term produces a voltage difference at the sample boundary which can be easily detect in an close circuit configuration if ohmic contacts are placed on the sample. Soon after Tauc's theory, his predictions were experimentally confirmed using a germanium crystal by Oroshnik and coworker [OM60]. Some time later Lüdge and Riemann correlated the photovoltaic effect in a Si sample to striations caused by crystallization interface oscillations occurring during the crystal growth and gave to their measurement set-up the name of LPS-method [LR97]. The LPS apparatus, soon became the technique of choice for detecting doping inhomogeneities in semiconductor wafers [ALR<sup>+</sup>05, ALRS02].

Remarkably, we believe that the LPS mapping technique could be extended spanning a broader field of applications than just the probing of doping striations. As a matter of fact, relying on the theoretical framework developed by Tauc, one can conclude that the LPS method is suitable to asses the spatial variation at the  $\mu\text{m}$  scale of any material property, which affects the band structure of a semiconductor, triggering in this way a drift force acting on the photogenerated carriers. Despite this fact was already noted by Tauc in his pioneering paper, no experimental attempts in this direction have ever been reported in the literature. Just to mention some

possibilities, it would be very interesting to exploit the benefits in terms of fastness, cheapness and compactness of the LPS approach, to probe non-uniform lattice strain fields or the spatial dependence of the excess carrier lifetime.

Applications as a characterization tool can be then envisaged to assess the strain field in micro structures since the lattice deformation controls the valence and conduction band edge profile [Van89]. Also spatially dependent variations in the excess carrier lifetime, reducing the symmetry of the excess electron and hole carrier density could trigger a charge unbalance, resulting in a detectable photoinduced voltage difference between the sample boundaries. This may be of practical relevance to probe radiation-induced crystal damages, which limit the performances of detector devices used in high energy physics experiments[BDS<sup>+</sup>91, DHM<sup>+</sup>06]. Exploiting the same effect, application of LPS as a tool to measure variations in the excess carrier lifetime related to a spatial dependence of the crystal quality in a plastically relaxed buffer layer, can be envisaged. As a matter of fact to grow semiconductor devices, thick buffer material are routinely used when a lattice mismatch occurring between the active layer and the wafer crystal need to be accommodated [SDML10]. In this situations, especially when a multistep homoepitaxy growth procedure is adopted [CDB<sup>+</sup>10], the dislocation density along the growth direction, induced in the buffer layers by plastic relaxation of the elastic energy, is quite inhomogeneous. As a consequence also the excess carrier lifetime displays a spatial dependence which can be in principle probed by LPS experiments performed with vertical cut samples.

In order to give to the LPS technique a more robust foundation, and to explore novel application for this measurement apparatus, a deeper theoretical understanding of the physical effects governing the relation between the photo-induced voltage and sample inhomogeneities is required. On the same foot, the ultimate achievable spatial resolution of the method and its connection with the sample material parameters governing the charge unbalance demands further investigations. Indeed, the theory of the photovoltaic effect at the basis of the LPS method has been developed within an analytical approach, with the introduction of a number of simplifying assumptions such as 1D sample geometry, uniform mobility, constant Shockley-Read-Hall recombination (SRH), and rectangular illumination profile. Notice that the set of these constraints is not fully self-consistent, since for instance the doping inhomogeneity may induce a non-negligible spatial variation of the mobility and of the non-radiative recombination rate. Moreover, the 1D approximation is obviously inadequate to assess the effects related to the distribution of the photogenerated excess carriers, which in real application have a non-trivial decay profile along the in-plane and out-of-plane directions. Consider also that it is not true a priori that the SRH recombination is always the dominant mechanism governing the recombination dynamics, since also contributions from the Auger or surface recombination, which have been excluded in the Tauc analytic theory, may play an important role. For what concerns the assessment of the LPS spatial resolution, analytical results by Tauc are of little help. On the other hand from the experimental side a serious investigation has not been reported yet, despite the fact that shedding light on the relevant physical effects and material parameters which control the LPS spatial resolution, and understanding its connection with the spatial extension of the photogenerated excess carrier distribution, represents a valuable piece of information for the further developments of this characterization technique.

Motivated by the above consideration, the present work aims at filling this knowledge gap. To achieve this objective a joint theoretical and experimental investigation has been carried out. This has required the development from scratch of a numerical finite volume (FV) simulation model realized using the COMSOL Multiphysics<sup>®</sup> environment which will be presented in chapter 2, where the semiconductor equations adopted to describe the excess carrier dynam-

ics under steady state optical excitation are reported. This numerical approach allowed us to consider fully 3D sample geometries, avoiding all the simplifying assumption required by an analytical treatment. In Chapter 2 a compact description of the experimental LPS set-up used in this thesis and of the measurement procedure adopted are also provided. Chapter 3 is devoted to the description of the LPS signal generation both from an experimental and theoretical point of view. We deeply test the relation occurring between the LPS signal and the value at the illumination spot of the dopant gradient. Geometrical effects associated to the 3D character of the sample and to the shape of the contacts placed at the two sample boundaries are also discussed. Finally in Chapter 3 we also investigate the dependance of the LPS signal from the pump laser power illuminating the sample.

To asses the LPS spatial resolution, a set of inhomogeneous samples, intentionally doped by means of ion implantation, in order to produce a stripe array profile with sharp undoped/doped interfaces has been prepared. LPS experimental data from this set of samples, benchmarked against their numerical counterpart provided by our model, are presented in Chapter 4, together with a discussion about sample fabrication and structural characterization.

Novel LPS applications are envisaged in Chapter 5 where focus has been given on the case study of strain detection in silicon micro structures featuring 2D periodic array of external stressors. The associated strain field has been assessed by means of FV mechanical simulation, produced starting from the elastic constants of the stressor and strained materials. Relying on the deformation potential theory, the spatially resolved impact of this strain field on the band structure has been calculated and these data used to feed the COMSOL simulation in order to predict the resulting LPS map. To close the loop, a critical comparison of the LPS map with the input strain field is present at the end of the Chapter.

Our conclusions and perspectives are reported in Chapter 6. More technical details about the model and Tauc's theory have been deferred in a dedicated appendix at the end of the manuscript, while the preface contains a list of adopted symbols, a table of figures and contents.



# Chapter 2

## Theoretical Background and LPS set-up

In this chapter, after giving an intuitive picture of the physics at the basis of the bulk photovoltaic effect, we summarize the main findings obtained by Tauc to describe analytically the set up of a voltage difference at the boundary of an optically excited inhomogeneous semiconductor crystal. Subsequently we introduce the coupled differential equation system at the basis of the numerical model developed in this thesis, discussing in detail all the generation and recombination mechanisms governing the excess carrier dynamics that have been included in the simulations. Discretization procedures used to solve the model equation system are also reported in some detail, while more technical aspects have been separately presented in Appendix A. Finally, we illustrate the LPS-measurement set-up used to acquire data discussed in chapter 3 and 4.

### 2.1. An intuitive picture of the Bulk Photovoltaic Effect

To intuitively illustrate the basic physics underlying the bulk photovoltaic effect, we will refer to the simplifying case of a 1D geometry. We assume that the spatial variation of some material property in a semiconductor, as for instance its doping concentration, affects the band edge profile. Suppose that at equilibrium, this inhomogeneity produces a bending of the potential profile, similar to the one shown in Fig. 2.1(a) for the case of an  $n$ -type crystal whose dopant concentration peaks at the center of the sample. This inhomogeneity is accompanied by a non-uniform resistivity profile, which has been sketched Fig. 2.1(b).

When the system is locally excited with a well-focused continuous wave optical source (red vertical arrow in the top panel of Fig. 2.1), the photogenerated electron and holes drift toward opposite directions, due to the presence of a gradient in the band profile which acts as an effective electrical field for both types of carriers. These opposites drifts are responsible for a charge separation, which in turn induces an electrical dipole, localized in a neighbor of the laser spot. The dipole magnitude is expected to be an increasing function of the local value of the band edge gradient.

It follows that a potential difference  $U$  between the two sample edges is generated by the electric field associated to the photoinduced dipole. Since the sign and intensity of  $U$  depends on the local band bending, one can be easily convinced that the potential difference, measured sweeping the laser spot along the  $x$  direction, considered as a function of the laser focus position  $x_f$  has the qualitative behavior depicted by the blue curve in the bottom panel of Fig. 2.1. It follows that the spatially integrated photovoltage  $\int_0^x U(x_f) dx_f$ , where we have supposed that the left contact is placed at  $x = 0$ , is a function which closely track the resistivity profile. This latter quantity in turn can be straight-fully related to the doping concentration profile. This fact is the working

principle of the LPS method.

From the above consideration it is apparent that the photogenerated potential difference  $U$  can be interpreted as resulting from a screening effect of the internal electrical field. To this aim we notice also that at equilibrium, the inhomogeneous material, being locally neutral, features a zero voltage difference at the boundaries. A quantitative description of the bulk photovoltage effect has been first proposed in 1955 by Tauc [Tau55], who developed a simple analytic theory, focusing on the case of non-uniform doping profiles in 1D semiconductors. Neglecting the spatial variation of the excess carrier lifetimes and mobility, and introducing other simplifying assumptions (discussed in the following), Tauc proved that the photovoltage  $U(x_f)$  is directly proportional to the resistivity gradient  $d\rho/dx$  evaluated at  $x = x_f$ . This statement is in agreement with the intuitive picture discussed above since in the spatial regions where  $d\rho$  is an increasing function of  $x$ , the doping concentration decreases. Assuming also that the photogenerated carrier distribution is far apart from the sample boundaries, Tauc demonstrated that the voltage for  $n$ - and  $p$ -type materials  $U_{n,p}(x_f)$ , measured as the difference between the right and left contact potential when the illuminated spot is in  $x_f$ , can be written as:

$$U_{n,p}(x_f) = \pm \frac{2k_B T}{q(1 + \frac{\mu_n}{\mu_p})} \cdot \oint \Delta\sigma \cdot \frac{d\rho}{dx} dx \quad (2.1)$$

where  $q$  is the absolute value of the elementary charge,  $\mu_n$  and  $\mu_p$  are the electron and hole mobility, respectively, and the upper (lower) sign refers to  $n$ -( $p$ ) type systems. In Eq. (2.1),  $\Delta\sigma$  is the photoinduced variation of the conductance and then the integral has to be calculated over the narrow region where the excess carrier distribution is not zero.

If the electron and hole mobilities depend only weakly on the spot position, it follows that integrating both members in Eq. (2.1) from the left contact set at  $x = 0$  up to a given position  $x$ , the function obtained is roughly directly proportional to the resistivity  $\rho(x)$ . This result supports the conclusion that the LPS apparatus can be used to relate in a direct manner the spatially integrated photovoltage maps to the local variations in the doping concentration.

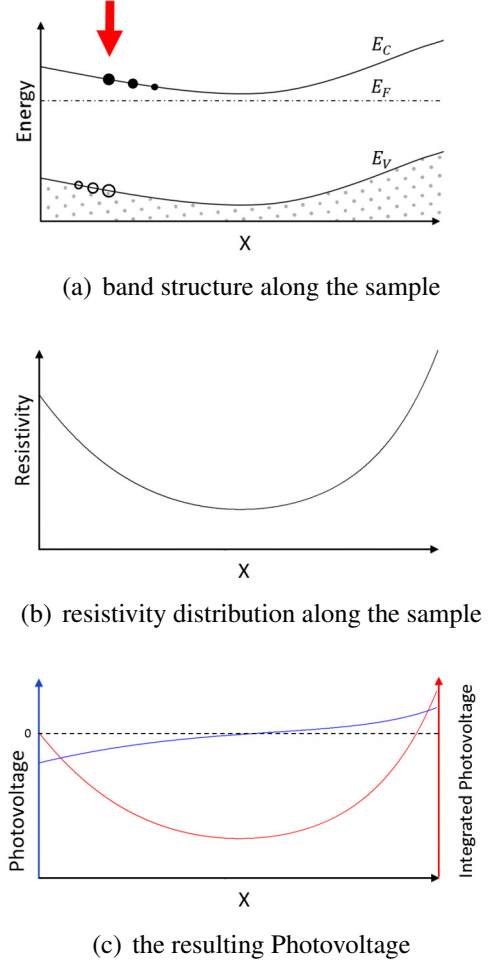


Fig. 2.1: Band edge (a) and resistivity (b) profile along the  $x$ -direction of an inhomogeneously doped  $n$ -type semiconductor bar with negligible transverse thicknesses. In the top panel the illuminated portion of the sample (red vertical arrow) and the drifting of excess electrons (filled circles) and holes (empty circles) are also sketched. (c) Photogenerated voltage difference  $U$  as a function of the excitation spot position  $x_f$  (blue curve). The red curve represents the spatial integrated photovoltage (see text).

## 2.2. Analytical theory of the bulk Photovoltaic Effect

In this Section we summarize the theoretical framework first developed by Tauc [Tau55] and subsequently adopted by other authors[OM60] to interpret their experimental findings. Focus is given to inhomogeneities associated to spatial dependent doping concentrations. As a starting point we assume a 1D ring sample geometry as shown in Fig 2.2, assuming that the area  $\overline{bc}$  is illuminated with monochromatic light. The sample contacts, where the photoinduce voltage difference  $U = \Phi_{a'} - \Phi_a$  is detected, are placed at the two boundaries and in the figure are marked as  $a$  and  $a'$ . It is assumed also that the contact positions are far enough from the illuminated region to prevent the excess carrier density reaching them. Furthermore we suppose that the sample thickness is sufficiently small compared to the reciprocal of the absorption coefficient in the direction of the radiating field; on the same foot also the transverse direction is assumed much thinner with respect to the beam diameter, so that the pump generation rate can be assumed constant in the entire  $\overline{bc}$  volume. In continues wave (CW) illumination condition, excess electrons and holes are generated with a steady rate, and the related density  $n$  and  $p$  result to be enlarged by  $\Delta n$  with respect to the equilibrium values  $n_{eq}$  and  $p_{eq}$ .

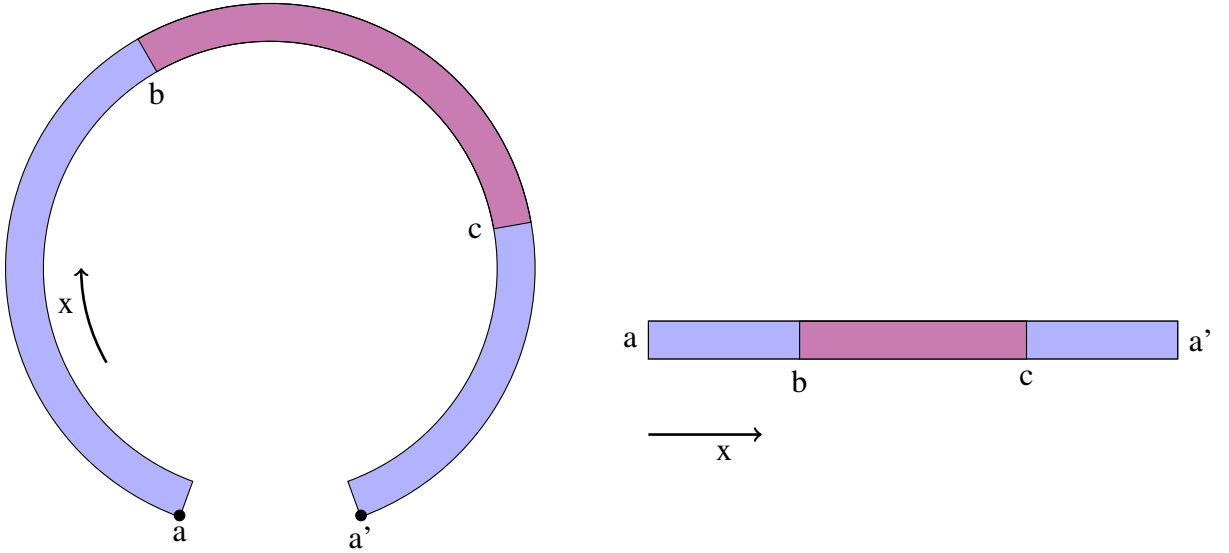


Fig. 2.2: 1D adopted sample geometry. The redish region represents the illuminated portion of the sample; the two contacts are placed at the sample boundaries and are marked as  $a$  and  $a'$ .

For stationary conditions, in the two channel representation it holds

$$\frac{dJ_p}{dx} = -\frac{dJ_n}{dx} = -\frac{q\Delta n}{\tau} + qG \quad (2.2)$$

$$J_p = q\mu_p \left( pE - \frac{k_B T}{q} \nabla_x p \right) \quad (2.3)$$

$$J_n = q\mu_n \left( nE + \frac{k_B T}{q} \nabla_x n \right) \quad (2.4)$$

$$p = p_{eq} + \Delta n, \quad n = n_{eq} + \Delta n, \quad (2.5)$$

the  $p$  and  $n$  indexes refers to hole and electron respectively,  $J(x)$  is the current density,  $\mu$  the mobility,  $q$  the elementary electric charge,  $k_B$  the Boltzmann constant,  $E(x)$  the total internal

electric field, and  $T$  the lattice temperature.  $G(x)$  represents the pump-induced generation rate while the recombination dynamics controlled by the SRH mechanism with a non-radiative lifetime  $\tau$ .

Summing Eq. (2.3) to (2.4) since  $J_p + J_n = 0$  one obtains for the electric field

$$E = \frac{k_B T}{q} \frac{\mu_p \nabla_x p - \mu_n \nabla_x n}{\mu_p p + \mu_n n}. \quad (2.6)$$

As we are interested in the potential difference  $U = \Phi_{a'} - \Phi_a$ , integration of the former Eq. (2.6) gives

$$U = \oint E dx = \frac{k_B T}{q} \oint \frac{\mu_p \nabla_x p - \mu_n \nabla_x n}{\mu_p p + \mu_n n} dx. \quad (2.7)$$

where in our ring geometry the integral has been performed on a closed circuit from  $a$  to  $a'$ . Relying on the Eq. (2.7) we now evaluate  $U$  for three different situations: *i*) a non-illuminated semiconductor; *ii*) illuminated homogeneous semiconductor; *iii*) inhomogeneous illuminated semiconductor. In the first two cases, as one can intuitively expect a zero value for the voltage difference is found while a detectable photovoltage effect may occur only for *iii*).

***i*) non-illuminated semiconductor** In the absence of a perturbation that drives the system out of equilibrium

$$n(x) = n_{\text{eq}}(x) \quad , \quad p(x) = p_{\text{eq}}(x) = \frac{n_i(x)^2}{n(x)} \quad (2.8)$$

where  $n_i(x)$  is the intrinsic charge carrier concentration at  $T$  which as  $n_{\text{eq}}$  and  $p_{\text{eq}}$  is a spatial dependent quantity in non-homogeneous samples. Combining the above relations with Eq. (2.7) we find

$$\begin{aligned} U &= \frac{k_B T}{q} \oint \frac{\mu_p \nabla_x \frac{n_i^2}{n_{\text{eq}}} - \mu_n \nabla_x n_{\text{eq}}}{\mu_p \frac{n_i^2}{n_{\text{eq}}} + \mu_n n_{\text{eq}}} dx = \frac{k_B T}{q} \oint \frac{-\mu_p \frac{n_i^2}{n_{\text{eq}}^2} \nabla_x n_{\text{eq}} - \mu_n \nabla_x n_{\text{eq}}}{\mu_p \frac{n_i^2}{n_{\text{eq}}^2} n_{\text{eq}} + \mu_n n_{\text{eq}}} dx \\ &= \frac{k_B T}{q} \oint \frac{-\nabla_x (n_{\text{eq}}) \left( \mu_p \frac{n_i^2}{n_{\text{eq}}^2} + \mu_n \right)}{n_{\text{eq}} \left( \mu_p \frac{n_i^2}{n_{\text{eq}}^2} + \mu_n \right)} dx = \frac{k_B T}{q} \oint \frac{-\nabla_x n_{\text{eq}}}{n_{\text{eq}}} dx \\ &= -\frac{k_B T}{q} \left( \ln n_{\text{eq}}|_{a'} + \ln n_{\text{eq}}|_a \right) = 0. \end{aligned} \quad (2.9)$$

This proves that, a voltage difference in our ring geometry can occur in illuminated samples only.

***ii*) homogeneous semiconductor** Now we consider a sample with homogeneous dopant concentration:

$$\nabla_x p_{\text{eq}} = \nabla_x n_{\text{eq}} = 0. \quad (2.10)$$

Using  $p(x) = p_{\text{eq}} + \Delta n(x)$  and  $n = n_{\text{eq}} + \Delta n(x)$ , where the notation evidences that now only the excess carrier density is a spatial dependent quantity, and exploiting the hypothesis that mobility does not vary in a significant way in the region featuring a non-negligible  $\Delta n(x)$ , we find:

$$\begin{aligned}
U &= \frac{k_B T}{q} \int \frac{\mu_p \nabla_x (p_{eq} + \Delta n) - \mu_n \nabla_x (n_{eq} + \Delta n)}{\mu_p (p_{eq} + \Delta n) + \mu_n (n_{eq} + \Delta n)} dx \\
&= (\mu_p - \mu_n) \frac{k_B T}{q} \int \frac{\nabla_x \Delta n}{\mu_p p_{eq} + n_{eq} \mu_n + (\mu_p + \mu_n) \Delta n} dx.
\end{aligned}$$

By partial fraction decomposition the above integral can be separated into three contributions, which can easily be integrated:

$$\begin{aligned}
U &= (\mu_p - \mu_n) \frac{k_B T}{q} \left( \int \frac{a_1}{\mu_p p_{eq}} dx + \int \frac{a_2}{n_{eq} \mu_n} dx + \int \frac{a_3}{(\mu_p + \mu_n) \Delta n} dx \right) \\
a_1 &= \frac{\nabla_x \Delta n}{(\mu_n + \mu_p) \mu_n n_{eq} \Delta n} \quad a_2 = a_1 \frac{\mu_n n_{eq}}{\mu_p p_{eq}} \quad a_3 = -a_1 \frac{(\mu_n + \mu_p) \Delta n}{\mu_p p_{eq}}. \quad (2.11)
\end{aligned}$$

As a matter of fact, each of this three contribution has the same functional form of Eq. (2.9) with the substitution  $\Delta n(x) \rightarrow n_{eq}(x)$ . As a consequence also for the case of an illuminated homogeneous sample we come to the conclusion that no photovoltage  $U$  can be produced independently of the beam position and profile.

*iii) inhomogeneous illuminated semiconductor* To discuss the case of an illuminated inhomogeneous semiconductor sample we separate the contribution in the spatial dependent electrical conductivity which originates from the presence of an excess carrier density setting  $\sigma(x) = \sigma_{eq}(x) + \Delta\sigma(x)$ . Relying on the assumption that mobility is a spatially invariant quantity, unaffected by the excess carrier density, the following relations hold:

$$\sigma_{eq} = \frac{1}{\rho_{eq}} = q\mu_n n_{eq} + q\mu_p p_{eq}, \quad (2.12)$$

$$\Delta\sigma = q(\mu_n + \mu_p)\Delta n, \quad n_{eq} p_{eq} = n_i^2 \quad \rightarrow \quad \frac{1}{n_{eq}} \frac{dn_{eq}}{dx} = -\frac{1}{p_{eq}} \frac{dp_{eq}}{dx}. \quad (2.13)$$

Plugging Eqs. (2.13) into Eq.(2.7) we get for  $U$

$$\begin{aligned}
U &= \frac{k_B T}{q} \int \frac{\mu_p \nabla_x (p_{eq} + \Delta n) - \mu_n \nabla_x (n_{eq} + \Delta n)}{\mu_p (p_{eq} + \Delta n) + \mu_n (n_{eq} + \Delta n)} dx \\
&= -\frac{k_B T}{q} \int \frac{\mu_p \frac{p_{eq}}{n_{eq}} \nabla_x n_{eq} + \mu_n \nabla_x n_{eq} - (\mu_p - \mu_n) \nabla_x \Delta n}{\sigma_{eq} + \Delta\sigma} dx \\
&= -\frac{k_B T}{q} \left( \int \frac{\sigma_{eq}}{\sigma_{eq} + \Delta\sigma} \frac{\nabla_x n_{eq}}{n_{eq}} dx - \frac{\mu_p - \mu_n}{\mu_p + \mu_n} \int \frac{1}{\sigma_{eq} + \Delta\sigma} \nabla_x \Delta\sigma dx \right). \quad (2.14)
\end{aligned}$$

To proceed further we assume weak illumination condition so that:  $\frac{\sigma_{eq}}{\sigma_{eq} + \Delta\sigma} \approx 1 - \frac{\Delta\sigma}{\sigma_{eq}}$ . Using  $\rho_{eq} = 1/\sigma_{eq}$  and  $\int \frac{1}{\sigma_{eq}} \nabla_x \Delta\sigma dx = -\int \Delta\sigma \nabla_x \rho_{eq} dx$ , the two integrals in Eq. 2.14 can be recast as:

$$U = -\frac{k_B T}{q} \left( \int -\frac{\Delta\sigma}{\sigma_{eq}} \frac{\nabla_x n_{eq}}{n_{eq}} dx + \frac{\mu_p - \mu_n}{\mu_p + \mu_n} \int \Delta\sigma \nabla_x \rho_{eq} dx \right). \quad (2.15)$$

Finally we exploit the relation:

$$\frac{\nabla_x n_{eq}}{n_{eq}} = \pm \frac{\nabla_x \sigma_{eq}}{\sigma_{eq}} = \mp \sigma_{eq} \nabla_x \rho_{eq}, \quad (2.16)$$

where the upper and lower sign refers to  $p$ - and  $n$ -type materials, respectively, to get:

$$U_{n,p} = -\frac{k_B T}{q} \left( \oint \pm \Delta \sigma \nabla_x \rho_{eq} dx + \frac{\mu_p - \mu_n}{\mu_p + \mu_n} \oint \Delta \sigma \nabla_x \rho_{eq} dx \right) \quad (2.17)$$

$$= \mp \frac{2\mu_{p,n} k_B T}{q(\mu_p + \mu_n)} \cdot \oint \Delta \sigma \cdot \frac{d\rho_{eq}}{dx} dx. \quad (2.18)$$

The above relation can be conveniently expressed in terms of the equilibrium carrier density since this allows to link, assuming local quasi neutrality condition, the photogenerated voltage with the spatial profile of the dopants

$$U_{n,p}(x_f) = \pm \frac{2\mu_{p,n} k_B T}{q(\mu_p + \mu_n)} \cdot \oint \Delta \sigma \cdot \frac{dn_{eq}}{n_{eq}^2 dx} dx = \mp \frac{2\mu_{p,n} k_B T}{q(\mu_p + \mu_n)} \oint \Delta \sigma \cdot \frac{1}{N_{D,A}^2} \frac{dN_{D,A}}{dx} dx. \quad (2.19)$$

From Eq. (2.19), which describes the same relation anticipated in Section 2.1, it is apparent that scanning the focal position  $x_f$ , the photogenerated voltage  $U$  can be used to probe the local value of the dopant gradient, with a spatial resolution which is controlled by the narrow region where the pump induced conductivity variation  $\Delta \sigma(x)$  is not zero. As a matter of fact, in a LPS measurement as a first step the pump position  $x_f$  is scanned along a line connecting the contact  $a$  and  $a'$  and the associated  $U_{n,p}(x_f)$  voltage difference recorded. Subsequently to assess the local value of the donor/acceptor density  $N_{D,A}(x)$ , the LPS algorithm calculate the signal  $S(x)$  performing for each  $x$  the spatial integration

$$S(x) = \int_a^x U_{n,p}(x') dx' \quad (2.20)$$

From the Eq. 2.19 we get for  $S(x)$

$$S(x) \propto \int_a^{a'} \int_a^{a'} \frac{\Delta \sigma(x', x'')}{N_{D,A}^2(x'')} \frac{dN_{D,A}}{dx''} dx' dx'' \quad (2.21)$$

where we used  $\Delta \sigma(x', x'')$  the variation of the conductivity at  $x''$  due to an illuminated spot centered in  $x'$ . Assuming that  $\Delta \sigma$  can be approximated with a rectangular shape function according to  $\Delta \sigma(x', x'') = \overline{\Delta \sigma} \cdot [\Theta(x'' - x' - w/2) - \Theta(x'' - x' + w/2)]$  where  $\overline{\Delta \sigma}$  is an average spatially constant value and  $w$  is the width of the interval centered in the focal spot  $x''$  where  $\Delta \sigma$  differs from zero, the following equation holds:

$$S(x) \propto \overline{\Delta \sigma} \int_{x-w/2}^{x+w/2} \frac{1}{N_{D,A}^2(x')} \frac{dN_{D,A}(x')}{dx'} dx' = \overline{\Delta \sigma} \frac{1}{N_{D,A}} \Big|_{x-w/2}^{x+w/2} \quad (2.22)$$

$$\propto \overline{\Delta \sigma} \rho_{eq} \Big|_{x-w/2}^{x+w/2} = w \overline{\Delta \sigma} \nabla_x \rho_{eq} \quad (2.23)$$

This relation represents the theoretical basis of the LPS method and roots back to 1955 when Tauc first derived the theory of the bulk photovoltaic effect for inhomogeneously doped material. However, as already noticed, his analytical approach required different simplifying assumptions as 1D geometry, uniform illumination and weak excitation condition. Moreover, as shown above, to relate the LPS signal  $S(x)$  to the resistivity gradient, quite drastic assumptions have been made to approximate  $\Delta \sigma(x', x'')$ . It worth to notice that the translation invariance introduced for  $\Delta \sigma(x', x'')$  is somehow not consistent with the material inhomogeneity itself, since both the spatial extension and the average value of  $\overline{\Delta \sigma}$  may significantly depend on the

local value of the doping density. Furthermore, while Tauc in developing his theory had in mind the case of an illuminated window featuring a finite width, nowadays in real application a well focused laser beam is commonly used to excite the material. Therefore the excess carrier distribution and the accompanying spatial profile of the conductance variation  $\Delta\sigma(x', x'')$  may significantly differ from the rectangular profile assumed to derive Eq. (2.23). The fully numerical approach described in the following sections allowed us to overcome also these limiting assumptions. Nevertheless, the analytical results derived here remains a useful guideline to interpret numerical data.

For this reason, it worth to elaborate further Eq. (2.14) in order to describe beyond the weak signal approximation used in the former Section, also the functional dependence of the photo-generated signal on the power of the pump beam. To this aim for simplicity we focus on the case of an illuminated  $n$ -type inhomogeneously doped material, assuming as above that the excess carrier distribution has a nearly rectangular profile. We define this excited spatial range as  $\overline{bc}$ . In Appendix A it is shown that the closed circuit integrals in Eq.2.7 can be recast in terms of integrals extending over the  $\overline{bc}$  range, only. Therefore, since only the  $\overline{bc}$  interval becomes relevant, in order to achieve an analytical expression for  $U$ , a linear approximation for the spatially varying conductivity can be introduced, assuming  $\sigma_{\text{eq}} = \sigma_0 + \zeta x$ . Under this hypothesis, and using  $\nabla_x n_{\text{eq}}/n_{\text{eq}} = \nabla_x \sigma_{\text{eq}}/\sigma_{\text{eq}}$ , in Appendix A it is shown that Eq. (2.14) gives

$$U = -\frac{k_B T}{q} \frac{2}{\frac{\mu_n}{\mu_p} + 1} \ln \left[ \frac{1 + \frac{\Delta\sigma}{\sigma_0 + \zeta c}}{1 + \frac{\Delta\sigma}{\sigma_0 + \zeta b}} \right] = -\frac{k_B T}{q} \frac{2}{\frac{\mu_n}{\mu_p} + 1} \ln \left[ \frac{1 + \frac{\Delta\sigma}{\sigma(c)}}{1 + \frac{\Delta\sigma}{\sigma(b)}} \right] \quad (2.24)$$

$$= -\frac{k_B T}{q} \frac{2}{\frac{\mu_n}{\mu_p} + 1} \left( \ln \left[ \frac{\sigma(c)}{\sigma(b)} \right] - \ln \left[ \frac{\sigma(c) + \Delta\sigma}{\sigma(b) + \Delta\sigma} \right] \right). \quad (2.25)$$

This result indicates that the photovoltage features a saturation value  $U_{\text{max}} = \frac{k_B T}{q} \frac{2}{\frac{\mu_n}{\mu_p} + 1} \ln \left[ \frac{\sigma(c)}{\sigma(b)} \right]$  controlled by the resistivity variation in a neighbor of the illuminated spot, as graphically illustrated in Fig. 2.3, where  $U/U_{\text{max}}$  has been calculated as a function of  $\Delta\sigma/\sigma(b)$  for different values of the ratio  $\sigma(c)/\sigma(b)$ . The asymptotic behaviour of  $U$  is explained considering that the excess carriers tend to screen the local band bending, and then in the limit of  $\Delta n \rightarrow \infty$  the contribution to the signal originating from further excess carriers becomes negligible. In the opposite regime i.e. when  $\Delta n \ll \min(n_{\text{eq}}(b), n_{\text{eq}}(c))$ , screening effects are absent and consequently Eq. (2.23) indicates a linear behavior of the photogenerated signal as a function of the conductivity variation. If also this latter quantity varies linearly with the pump power the detected signal in this weak excitation regime is predicted to be proportional to the laser fluency.

## 2.3. Numerical Model Equations

### 2.3.1. Equation System

The fully numerical simulation of the LPS measurement is based on the self-consistent solution of the van-Roosbroeck semiconductor equation system which describes the spatially resolved electron  $n$  and hole  $p$  total carrier density and the associated electrical potential  $\Phi$  [Van50, Van53]. These quantities are linked by Poisson's equation

$$-\nabla \cdot (\epsilon \nabla \Phi) = q(p - n + N_D^+ - N_A^-) \quad (2.26)$$

where  $\epsilon$  is the static permittivity and  $N_A^-$  ( $N_D^+$ ) is the numerical concentration of ionized acceptor (donor) atoms which for our purpose is set equal to the impurity concentration  $N_A$  ( $N_D$ ). The

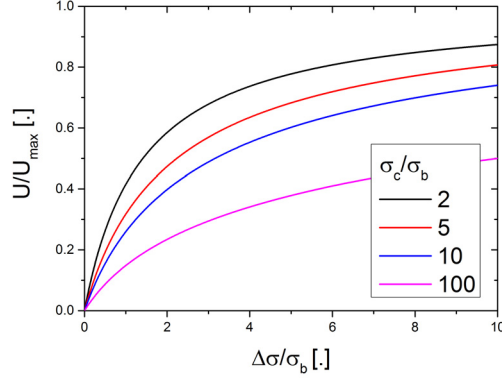


Fig. 2.3: Photo-voltage in units of the saturation value  $U_{\max}$  calculated as a function of  $\Delta\sigma/\sigma(b)$  for different values of the  $\sigma(c)/\sigma(b)$  ratio.

continuity equations for charge carriers in the two-channel approximation reads

$$\frac{\partial n}{\partial t} - \frac{1}{q} \nabla \cdot \mathbf{J}_n = G - R \quad (2.27)$$

$$\frac{\partial p}{\partial t} - \frac{1}{q} \nabla \cdot \mathbf{J}_p = G - R. \quad (2.28)$$

In the above equations  $\mathbf{J}_n$  and  $\mathbf{J}_p$  is the current density for electrons and holes, respectively, and  $G$  and  $R$  represent the generation and recombination rates. Since all the experiments are performed at room temperature (RT), we neglect contributions to the current due to the presence of temperature gradients in a neighbour of the laser spot. Therefore the current results from the combination of drift  $\mathbf{J}_{\text{Drift}}$  and diffusive  $\mathbf{J}_{\text{Diff}}$  motion according to

$$\mathbf{J} = \mathbf{J}_{\text{Drift}} + \mathbf{J}_{\text{Diff}} + \mathbf{J}_{\text{Fk}} \quad (2.29)$$

$$\mathbf{J}_{\text{Drift}} = \mathbf{J}_{n,\text{Drift}} + \mathbf{J}_{p,\text{Drift}} = q(n\mu_n \nabla E_C + p\mu_p \nabla E_V) \quad (2.30)$$

$$\mathbf{J}_{\text{Diff}} = \mathbf{J}_{n,\text{Diff}} + \mathbf{J}_{p,\text{Diff}} = q(D_n \nabla n - D_p \nabla p), \quad (2.31)$$

where we have separated the hole and electron terms. The local bending of the conduction  $\nabla E_C$  and valence  $\nabla E_V$  band edge acts as the drift field driving  $\mathbf{J}_{\text{Drift}}$ ; the spatial dependent diffusion constants  $D$  are calculated according to the generalized Einstein equations [Com13]:

$$\text{electrons: } \frac{D_n}{\mu_n} = \frac{k_B T}{q} g \left( \frac{n}{N_c} \right) \quad (2.32)$$

$$\text{holes: } \frac{D_p}{\mu_p} = \frac{k_B T}{q} g \left( \frac{p}{N_v} \right). \quad (2.33)$$

In the above expression the function  $g = g(n/N_c)$  is associated to the inverse Fermi-Dirac-integral and  $N_v$  and  $N_c$  are the effective density of states in the valence and conduction band, respectively [Com13].

### 2.3.2. Recombination Mechanisms

In this section we elucidate the different contribution to the recombination rate  $R$  in the right-hand-side of the Eqs. (2.27) and (2.28). As a matter of fact in our model the total rate  $R$



contains contributions from radiative  $R_{\text{Rad}}$ , Shockley-Read-Hall  $R_{\text{SRH}}$ , Auger  $R_{\text{Au}}$  and surface recombination  $R_{\text{S}}$  channels

$$R = R_{\text{Rad}} + R_{\text{SRH}} + R_{\text{Au}} + R_{\text{S}}. \quad (2.34)$$

Preliminary to the description of each channel, it is useful to define the equilibrium intrinsic carrier density  $n_i$  as

$$n_i = \gamma_n \gamma_p \sqrt{N_C N_V} \cdot \exp \left[ -\frac{E_g}{2k_B T} \right]. \quad (2.35)$$

Here  $E_g$  is the (spatially constant) energy gap and  $\gamma_n$  and  $\gamma_p$  are given by

$$\gamma_n = \frac{\mathcal{F}_{1/2} \left( -\frac{E_c - \varphi_{f,n}}{k_B T} \right)}{\exp \left[ -\frac{E_c - \varphi_{f,n}}{k_B T} \right]}, \quad \gamma_p = \frac{\mathcal{F}_{1/2} \left( -\frac{\varphi_{f,p} - E_v}{k_B T} \right)}{\exp \left[ -\frac{\varphi_{f,p} - E_v}{k_B T} \right]},$$

where  $\varphi_{f,n}$  and  $\varphi_{f,p}$  are the quasi Fermi potentials for electrons and holes, respectively and  $\mathcal{F}_{1/2}$  is the Fermi-Dirac integral [Com13].

**Radiative Recombination** The radiative recombination of excess carriers in an out of equilibrium semiconductor is governed by the spontaneous photon emission process, accompanied by the annihilation of an electron/hole pair. The associated rate  $R_{\text{Rad}}$  is a two body process and can be phenomenologically described introducing a  $C_{\text{Rad}}$  coefficient as

$$R_{\text{Rad}} = C_{\text{Rad}}(np - n_i^2). \quad (2.36)$$

**SRH Recombination** The Shockley-Read-Hall recombination mechanism describes the interaction of a charge carrier with a lattice defect, in our case mainly boron/phosphorus impurities. To evaluate the  $R_{\text{SRH}}$  rate, four processes are usually considered:

- 1<sup>st</sup> trapping of an electron from the conduction band by an empty trap state
- 2<sup>nd</sup> emitting of an electron to the conduction band by a filled trap state
- 3<sup>rd</sup> emitting of a hole to the valence band by an empty trap state
- 4<sup>th</sup> trapping of a hole by filled trap with an electron state

Similar to the radiative recombination, the SRH-mechanism always involve the creation or annihilation of an electron/hole pair. Hence, the recombination rates for electrons  $R_{\text{SRH}}^n$  and holes  $R_{\text{SRH}}^p$  have to be equal and can be expressed in terms of electron  $\tau_e$  and hole  $\tau_h$  trap capture time as [Com13]

$$R_{\text{SRH}} = R_{\text{SRH}}^n = R_{\text{SRH}}^p = \frac{np - n_i^2}{\tau_p(n + n_d) + \tau_e(p + p_d)}, \quad (2.37)$$

where  $n_d$  and  $p_d$  are the charged trap densities obtained from

$$n_d = n_i \exp \left[ \frac{E_t - E_i}{k_B T} \right], \quad (2.38)$$

$$p_d = n_i \exp \left[ \frac{E_i - E_t}{k_B T} \right], \quad (2.39)$$

having indicated with  $E_i$  and  $E_t$  the intrinsic and trap energy levels, respectively. Notice that in Si, which features very low radiative efficiency due to the indirect character of the fundamental gap, the SRH channel is often the main mechanism controlling the excess carrier lifetime. Consequently by changing the impurity concentration which influences  $R_{\text{SRH}}$ , the carrier lifetime can be varied by several order of magnitude.

**Auger Recombination** The Auger recombination process is a three particle phenomenon. In fact, the residual energy associated to the annihilation of an electron/hole pair in an Auger event is transferred to a third carrier. For this reason the rate  $R_{\text{Au}}$ , which again must be equal for electron and holes, is a cubic function in the carrier concentrations and is given by the following expression

$$R_{\text{Au}} = R_{\text{Au}}^n = R_{\text{Au}}^p = (C_{\text{Au}}^n n + C_{\text{Au}}^p p)(np - n_i^2). \quad (2.40)$$

In the above equation the two coefficients  $C_{\text{Au}}^n$   $C_{\text{Au}}^p$  are effective quantity which depend on the temperature and the band structure and are related to scattering events involving two electrons and one hole or two holes and one electron, respectively.

**Surface Recombination** The surface recombination process is due to the presence of dangling bonds at the crystal boundaries. When carriers reach the surface at a rate controlled by their thermal velocity, they can be reflected back or alternatively a recombination process may occur. Therefore the surface recombination rate  $R_S$  is proportional to the local value of the excess carrier density  $\Delta n$ . Since the recombination probability depends also on the specific property of the surface  $R_S$  obeys

$$R_S = S_{\text{eff}} \Delta n|_{\partial\Omega}. \quad (2.41)$$

where  $\partial\Omega$  indicates the excess carrier density evaluated at the sample boundary and  $S_{\text{eff}}$  is an effective parameter known as surface recombination velocity which can greatly vary with the surface quality. For this reason, while the values of all the other material parameters adopted in the simulations discussed in the following chapters are taken from the literature, the surface velocity used in the model have been experimentally determined as reported later.

### 2.3.3. Generation Rate

To take into account the complete 3D geometry we describe the generation rate  $G$  of Eqs. (2.27) and (2.28) due to the laser pump beam as

$$G = N_{\text{ph}} \mathcal{L}(x, y, z) \quad (2.42)$$

where  $N_{\text{ph}}$  is the rate of impinging photon and  $\mathcal{L}(x, y, z)$  is a normalized function normalized to one which reproduces the laser 3D beam profile inside the material. Considering the reflection coefficient  $\mathcal{R}$ , the impinging photon rate close to the internal surface as a function of the laser power  $P$  and photon wavelength  $\lambda$  is given by

$$N_{\text{ph}} = (1 - \mathcal{R}) \frac{P\lambda}{hc}. \quad (2.43)$$

At the adopted photon energies we used for the air/Si interface reflectivity the value of 0.34. As for the beam shape we describe it as a two dimensional Gaussian in-plane ( $xy$ ) profile, exponentially decaying in the direction perpendicular to the sample surface (set at  $z = 0$ ):

$$\mathcal{L}(x, y, z) = \frac{A_c}{2\pi\sigma^2} \exp \left[ -A_c |z| - \frac{(x - x_f)^2}{2\sigma_L^2} - \frac{(y - y_f)^2}{2\sigma_L^2} \right], \quad (2.44)$$

where  $4\sigma_L = 1/e^2$  having indicating with  $e$  the spot size and with  $A_c$  the inverse penetration depth.

The value of these parameters together with the laser power and wavelength adopted to simulate our experimental conditions are reported in Tab. 2.1.

laser wave length [nm]	laser power [mW]	penetration depth [ $\mu\text{m}$ ]	$1/e^2$ -spot size [ $\mu\text{m}$ ]
830	170	15.4	5
685	20	4.7	5

Table 2.1: Laser beam parameters used in the model to simulate the LPS measurements in Si.

### 2.3.4. Mobility

Charge carrier mobility is calculated according to the Matthiessen's rule summing contribution from different scattering channels. In our model we considered interaction with acoustic phonons and ionized impurities, together with electron-electron and hole-hole scattering. Therefore we have

$$\frac{1}{\mu} = \frac{1}{\mu_{\text{ar}}} + \frac{1}{\mu_{\text{cc}}}. \quad (2.45)$$

where  $\mu_{\text{ar}}$  is the mobility calculated according to the so called Arora model [AHR82] which takes into account the phonon and charged impurity channels, while  $\mu_{\text{cc}}$  is the mobility obtained considering the carrier-carrier scattering, as reported in Ref.[Fle57].

Evaluating for  $T = 300\text{K}$  the relation for Si samples reported in [AHR82] which describes the electron and hole mobility as a function of the doping density and lattice temperature we get

$$\mu_{\text{n,ar}} \left[ \frac{\text{cm}^2}{\text{Vs}} \right] = 89 + \frac{1323}{1 + 0.8 \cdot 10^{-17} \cdot N_{\text{D}}^+ [\text{cm}^{-3}]} \quad (2.46)$$

$$\mu_{\text{p,ar}} \left[ \frac{\text{cm}^2}{\text{Vs}} \right] = 55 + \frac{429}{1 + 0.4 \cdot 10^{-17} \cdot N_{\text{A}}^- [\text{cm}^{-3}]}. \quad (2.47)$$

The carrier-carrier limited mobility  $\mu_{\text{cc}}$  for Si at RT as a function of the electron and hole concentrations reads

$$\mu_{\text{cc}} = \frac{F_1}{\sqrt{np} \ln [1 + (np)^{-1/3} \cdot F_2]}, \quad (2.48)$$

where  $F_1$  and  $F_2$  are constants, whose value as been reported in Table symbol explanation list. As a final remark we notice that in the above expression we neglect terms related to interaction with neutral impurities since no relevant contributions are expected for temperatures above 80 K.

## 2.4. Discretization procedures

In the previous section we have defined the equations implemented in the numerical model that we have developed to simulate the spatial distribution of the carrier densities and the resulting electrostatic potential, featured by an optically excited inhomogeneous semiconductor in steady state conditions. We devote this section to describe how  $n(r)$ ,  $p(r)$  and  $\Phi(r)$  are calculated using a well established 3D Finite-Volume approach, in the COMSOL Multiphysics 5.4 environment, relying on numerical routines contained in the module "semiconductor" [Com13].

The basis of our model is the system of coupled differential equations (SCDE) given by Eqs. (2.26-2.31). To numerically solve SCDE usually three main different approaches can be adopted i.e. the Finite-Volume-Method (FVM), the Finite-Element-Method (FEM), or the Finite- Difference-Method (FDM). A part from minor differences all these methods rely on discretization procedures performed in the direct space, and hence requires as a preliminary step the definition of a proper grid, representing the domain volume where the target variable are defined. The node density of the grid must be tailored to assure that numerical convergence, taking also into account the required accuracy and the limitations related to unaffordable simulation times or RAM availability. If the variable have to respect constrains related to the presence of space invariants, usually the FVM approach is the most convenient choice to exploit them, resulting in reduced computation times. Since this is our case, in the numerical model we have implemented the FVM method. Therefore, in the following we briefly present the FVM approach, directly specialized to the SCDE at the basis of the LPS simulations. The interest reader can find more details on FVM for instance in Ref. [Mad07].

### 2.4.1. The Finite Volume Method

As a first step we introduce the notation used to describe the discrete grid. For simplicity but without loss to generality we focus on the case of a cuboid domain  $\Omega$  (Fig. 2.4) left panel which is partitioned by means of a set of  $N$  not-overlapping cuboid sub-domains  $\{\omega_i\}$  with  $i = 1, \dots, N$  as shown in Fig. 2.4 right panel. Therefore we have

$$\Omega = \bigcap_{i=1}^N \omega_i \quad \text{with } \omega_i \cup \omega_j = \emptyset \text{ for } i \neq j \quad (2.49)$$

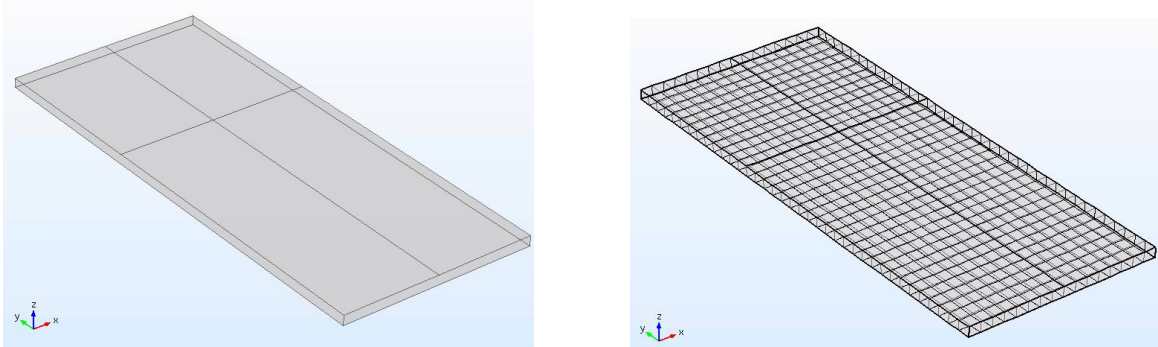


Fig. 2.4: Left panel: cuboid domain for a SCDE system. Right panel: discretization with an homogeneous cuboid grid of the domain shown in the left plot.

Three indices  $l, m, n$  are used to identify the spatial coordinates  $(x_l, y_m, z_n)$  of the central point  $P_l$  of  $\omega_l$ . Therefore the notation  $\omega_{lmn}$  can alternatively be used to indicate the  $i$ -th sub-domain. The boundaries along the three orthogonal directions of the cuboid sub-domain  $\omega_{lmn}$  centered in  $P_{lmn}$  are defined introducing half-integers as

$$x \in [x_{l-\frac{1}{2}} \quad x_{l+\frac{1}{2}}] \quad (2.50)$$

$$y \in [y_{m-\frac{1}{2}} \quad y_{m+\frac{1}{2}}] \quad (2.51)$$

$$z \in [z_{n-\frac{1}{2}} \quad z_{n+\frac{1}{2}}] \quad (2.52)$$

and its dimension along the three axes of the reference frame shown in Fig. 2.5 are indicated as  $\Delta x$ ,  $\Delta y$  and  $\Delta z$ .

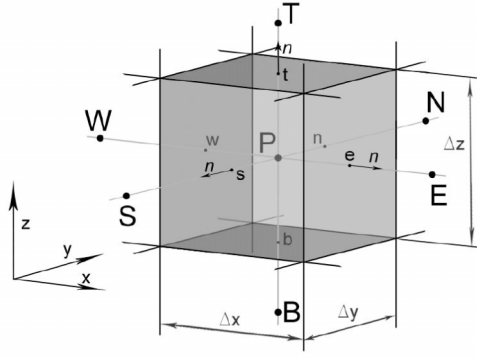


Fig. 2.5: Schematic of a cuboid sub-domain  $\omega_i$  taken from [Mad07]. Capital and lower letters are used to define the six orthogonal lines passing through P, and the intersection points with the corresponding boundary surface, respectively.

In Fig. 2.5 capital letters are used to specify both the six orthogonal lines perpendicular to the cuboid faces, passing through P and the central position of the associate neighbor cuboids. Using them we can indicate also the corresponding boundary cuboid faces. For instance  $\partial\omega_{i,W}$  is the boundary face along the West direction of the  $i$ -th cuboid, whose central coordinates are  $(x_i, y_i, z_i)$ . Using the half-integer notation the same boundary surface can also be indicated as  $\partial\omega_{i-\frac{1}{2},w}$ .

We now use the grid to discretize the SCDE at the basis of our model. Preliminary, it is useful to recall that the divergence theorem applied to the volume integral performed over the  $\omega_i$  sub-domain of the divergence of a vector field  $\mathbf{u}$ , enclosed by the oriented surface  $\partial\omega_i$  gives

$$\int_{\omega_i} \nabla \cdot \mathbf{u} d\omega = \oint_{\partial\omega_i} \mathbf{u} \cdot \boldsymbol{\eta} dS. \quad (2.53)$$

where  $\boldsymbol{\eta}$  is the vector orthogonal to the surface element  $dS$ .

Using this relation in combination with Eq. (2.26) we get

$$-\int_{\omega_i} \left( \frac{\partial^2 \Phi}{\partial x^2} + \frac{\partial^2 \Phi}{\partial y^2} + \frac{\partial^2 \Phi}{\partial z^2} \right) d\omega = - \oint_{\partial\omega_i} \left( \frac{\partial \Phi}{\partial x} \eta_x + \frac{\partial \Phi}{\partial y} \eta_y + \frac{\partial \Phi}{\partial z} \eta_z \right) dS \quad (2.54)$$

$$= \int_{\omega_i} \frac{q}{\epsilon} (p - n) d\omega + \int_{\omega_i} \frac{q}{\epsilon} (N_D - N_A) d\omega \quad (2.55)$$

$$= \int_{\omega_i} \frac{q}{\epsilon} (p - n) d\omega + C_i \quad (2.56)$$

where we have indicated as  $C_i$  the integral containing the donor densities to emphasise that it does not depend on the  $n(r)$  and  $p(r)$  variables.

Explicitly writing the contribution to the surface flux from the six cuboid faces (see Fig. 2.5) one obtains

$$\begin{aligned} & \left( \frac{\partial \Phi}{\partial x} \right)_w \Delta y \Delta z + \left( \frac{\partial \Phi}{\partial y} \right)_s \Delta x \Delta z + \left( \frac{\partial \Phi}{\partial z} \right)_b \Delta x \Delta y \\ & - \left( \frac{\partial \Phi}{\partial x} \right)_e \Delta y \Delta z - \left( \frac{\partial \Phi}{\partial y} \right)_n \Delta x \Delta z - \left( \frac{\partial \Phi}{\partial z} \right)_t \Delta x \Delta y = \int_{\omega_i} \frac{q}{\epsilon} (p - n) d\omega + C_i \end{aligned} \quad (2.57)$$

where the derivative are calculated at the face points specified in Fig. 2.6

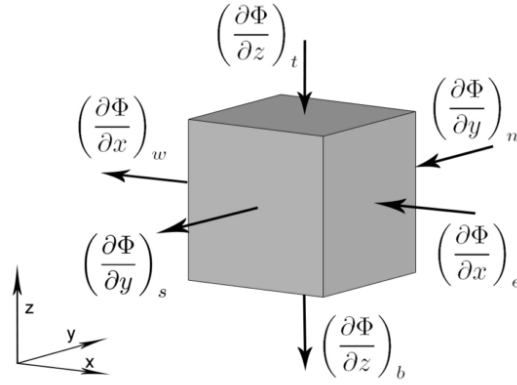


Fig. 2.6: Face contributions to the flux of the  $-\nabla\Phi$  vector field outgoing through the surface of the  $\omega_i$  volume.[Mad07].

To the first order in the cuboid dimension the derivatives in Eq. (2.57) can be express in term of the electrostatic potential  $\Phi$  at the central points of the neighbor volumes. This linearization is usually referred to as the Central-Differencing-Scheme (CDS). For instance for the derivative of the potential at the East face  $\left(\frac{\partial\Phi}{\partial x}\right)_e$  it holds (see Fig 2.7)

$$\left(\frac{\partial\Phi}{\partial x}\right)_e \approx \frac{\Phi_E - \Phi_P}{x_E - x_P} = \frac{\Phi_E - \Phi_P}{\delta x_e}, \quad (2.58)$$

where  $\delta x_e$  is equal to  $\overline{PE}/2$  that, for the case of non-uniform grid, is a spatial dependent quantity.

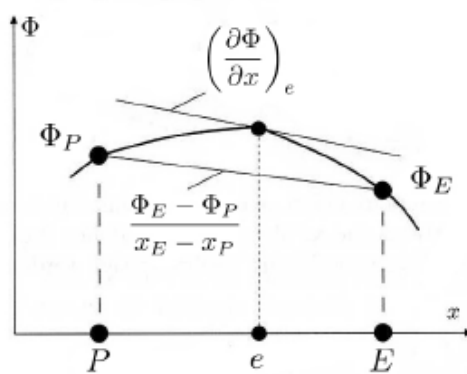


Fig. 2.7: Central difference scheme to evaluate the potential derivative at the central point of the  $E$  cuboid face. The  $P$  and  $E$  letters represent the  $x$ -coordinates of the central points of the neighbor cuboids.

Plugging Eq. (2.58) into (2.57) gives

$$a_P\Phi_P = a_E\Phi_E + a_N\Phi_N + a_T\Phi_T + a_W\Phi_W + a_S\Phi_S + a_B\Phi_B + b_P \quad (2.59)$$

with the  $a$  and  $b$  coefficients defined as

$$\begin{aligned}
a_E &:= \frac{\Delta y \Delta z}{(\delta x)_e}, & a_N &:= \frac{\Delta x \Delta z}{(\delta y)_n}, & a_T &:= \frac{\Delta x \Delta y}{(\delta z)_t}, \\
a_W &:= \frac{\Delta y \Delta z}{(\delta x)_w}, & a_S &:= \frac{\Delta x \Delta z}{(\delta y)_s}, & a_B &:= \frac{\Delta x \Delta y}{(\delta z)_b}, \\
b_P &:= \int_{\omega_i} \frac{q}{\varepsilon} (p - n) d\omega_i + C.
\end{aligned} \tag{2.60}$$

with  $\delta x_j = \overline{PJ}/2$  and  $a_P = a_E + a_N + a_T + a_W + a_S + a_B$  of the cuboid  $i$ . Eq. (2.59) for the  $\omega_i$  cuboid centered in  $P$  can be written in a more compact form

$$a_P^i \Phi_P^i - \sum_c a_c^i \Phi_c^i = b_P^i, \tag{2.61}$$

where the  $c$  index runs over the six neighbor cells of the  $\omega_i$  volume,  $\Phi_c^i$  is the potential calculated at the center of the  $c$  neighbor cuboid, and  $a_c^i$  is the length factor defined in the above equations, associated to the cuboid face shared between the  $i$  and  $c$  cells. The above expression can be recast in matrix format as  $\hat{A} \cdot \Phi = \mathbf{b}$ , where the  $\hat{A}$  is a sparse matrix of the order  $N \times N$ . For instance when the  $i$  basis order is chosen so that the  $i-1$  and  $i+1$  elements represent the W and E neighbors of the  $\omega_i$  volume respectively, the matrix representation can be written as

$$\underbrace{\begin{pmatrix} a_P^1 & -a_E^1 & 0 \dots & 0 & -a_W^1 & 0 \dots & 0 & -a_{FL}^1 & 0 \dots \\ -a_W^2 & a_P^2 & -a_E^2 & 0 & & & & & \\ & \cdot & \cdot & \cdot & & & & & \\ & & & \cdot & -a_W^i & a_P^i & -a_E^i & & \\ & & & & \cdot & \cdot & \cdot & & \\ & & & & & \cdot & \cdot & \cdot & \\ & & & & & & \cdot & \cdot & \\ & & & -a_{FL}^N & -a_E^i & 0 & -a_W^N & a_P^N & \end{pmatrix}}_{\hat{A}} \cdot \underbrace{\begin{pmatrix} \Phi_P^1 \\ \cdot \\ \cdot \\ \Phi_P^{i-1} \\ \Phi_P^i \\ \Phi_P^{i+1} \\ \cdot \\ \cdot \\ \Phi_P^N \end{pmatrix}}_{\Phi} = \underbrace{\begin{pmatrix} b_P^1 \\ \cdot \\ \cdot \\ b_P^{i-1} \\ b_P^i \\ b_P^{i+1} \\ \cdot \\ \cdot \\ b_P^N \end{pmatrix}}_{\mathbf{b}}$$

where  $a_{FL}^i$  represents a generic coupling term of the  $i$ -potential with the potential value which refers to a neighbour cell located along a direction different from the WE one.

Since the value of the  $\mathbf{b}$  vector in the right hand side of Eq. (2.61) is not known, to close the model equation system we have to derive the discretized version of the relations expressing the charge conservation condition. For this purpose, it is preliminary necessary to write the local value of the currents as a function of the drift field and of the charge densities in the neighbor cells. For stationary condition this has been done relying on the Scharfetter-Gummel scheme [SG69, Fre04] as detailed in the following where for simplicity we will temporarily refer to an unipolar 1D system. The starting point is the continuity equation

$$\frac{\partial n}{\partial t} = -\frac{\partial J}{\partial x} = 0 \tag{2.62}$$

whose discretized version is

$$\frac{\partial n_i}{\partial t} = \frac{J_{i-1/2} - J_{i+1/2}}{\Delta x}. \tag{2.63}$$

where again half integer indexes are used to represent physical variables calculated at the cell boundary surface. Setting  $v = -\mu \frac{d\Phi}{dx}$ ,  $J$  is given by

$$J = -D \frac{\partial n}{\partial x} + vn(x). \quad (2.64)$$

Multiplying both members of the above relation by  $\exp[-v(x-x_i)/D]$  and integrating over the  $[x_i, x_{i+1}]$  one obtains

$$\begin{aligned} \int_{x_i}^{x_{i+1}} J \exp[-v(x-x_i)/D] dx &= -D \int_{x_i}^{x_{i+1}} \frac{\partial}{\partial x} (n \exp[-v(x-x_i)/D]) dx \\ J_{i+1/2} \int_0^{\Delta x} \exp[-vx'/D] dx' &= -D (n \exp[-v(x-x_i)/D]) \Big|_{x_i}^{x_{i+1}} \\ J_{i+1/2} \frac{D}{v} (\exp[-v\Delta x/D] - 1) &= D (n_i - n_{i+1} \exp[-v\Delta x/D]), \end{aligned}$$

under the assumption that  $J$  is practically constant over the integration domain. Thus, considering also hole conduction we get for the current densities  $J_n$  and  $J_p$  the relations first derived by Scharfetter and Gummel:

$$J_{n,i+1/2} = v_n \frac{n_i - n_{i+1} \exp[-v_n \Delta x / D_n]}{1 - \exp[-v_n \Delta x / D_n]} \quad (2.65)$$

$$J_{p,i+1/2} = v_p \frac{p_i - p_{i+1} \exp[v_p \Delta x / D_p]}{1 - \exp[v_p \Delta x / D_p]}. \quad (2.66)$$

where  $v_n = -\mu_n \frac{d\Phi}{dx}$  and  $v_p = \mu_p \frac{d\Phi}{dx}$ .

Now, referring again to the 3D geometry we write the charge conservation in the  $\omega_p$  cuboid

$$0 = \frac{1}{\Delta x \Delta y \Delta z} \int_{\omega} -\frac{1}{q} \nabla \cdot \mathbf{J} d\omega + \frac{1}{\Delta x \Delta y \Delta z} \int_{\omega} (G - R) d\omega. \quad (2.67)$$

Exploiting the divergence theorem and setting  $M_p = \frac{1}{\Delta x \Delta y \Delta z} \int_{\omega_p} (G - R) d\omega$  we get

$$\frac{1}{\Delta x} (J_e + J_w) + \frac{1}{\Delta y} (J_s + J_n) + \frac{1}{\Delta z} (J_b + J_t) = qM_p \quad (2.68)$$

where  $J_c$  represents the normal component of the electron or hole current density  $\mathbf{J}$ , calculated at the  $c$  boundary surface of the  $P$  cuboid. In the case of electron current densities, those latter quantities, by means Eq. (2.65) can be written as

$$\begin{aligned} J_e(P \rightarrow E) &= -v_n^e \frac{n_e - n_p \exp\left(-\frac{v_n^e \Delta x}{D_n^e}\right)}{1 - \exp\left(-\frac{v_n^e \Delta x}{D_n^e}\right)} & J_w(P \rightarrow W) &= v_n^w \frac{n_p - n_w \exp\left(-\frac{v_n^w \Delta x}{D_n^w}\right)}{1 - \exp\left(-\frac{v_n^w \Delta x}{D_n^w}\right)} \\ J_s(P \rightarrow S) &= -v_n^s \frac{n_s - n_p \exp\left(-\frac{v_n^s \Delta y}{D_n^s}\right)}{1 - \exp\left(-\frac{v_n^s \Delta y}{D_n^s}\right)} & J_n(P \rightarrow N) &= v_n^n \frac{n_p - n_n \exp\left(-\frac{v_n^n \Delta y}{D_n^n}\right)}{1 - \exp\left(-\frac{v_n^n \Delta y}{D_n^n}\right)} \\ J_b(P \rightarrow B) &= -v_n^b \frac{n_b - n_p \exp\left(-\frac{v_n^b \Delta z}{D_n^b}\right)}{1 - \exp\left(-\frac{v_n^b \Delta z}{D_n^b}\right)} & J_t(P \rightarrow T) &= v_n^t \frac{n_p - n_t \exp\left(-\frac{v_n^t \Delta z}{D_n^t}\right)}{1 - \exp\left(-\frac{v_n^t \Delta z}{D_n^t}\right)} \end{aligned}$$



where the adopted notation emphasizes that the currents are calculated along the out-going directions with respect to the cuboid  $P$ , and a superscript has been added to the velocities to indicate the direction along which the potential derivative is calculated. For instance, for the east and west direction  $v_n^e = -\mu \frac{d\Phi}{dx}$ , and  $v_n^w = +\mu \frac{d\Phi}{dx}$ , respectively. Similarly, for the north and south directions it holds  $v_n^s = -\mu \frac{d\Phi}{dy}$ , and  $v_n^n = +\mu \frac{d\Phi}{dy}$ . Finally a superscript in the diffusion constant indicate the  $P$  neighbor cell, where the  $D$  value is calculated. The corresponding set of equations for hole current density can be easily obtained using Eq. (2.66). Plugging the above relations into Eq. (2.65), after a simple but lengthy algebra it can be proven that

$$\alpha_p n_p - \sum_c \alpha_c n_c = qM_P \quad (2.69)$$

with the  $\alpha$  coefficients are:

$$\alpha_p = \left( \frac{1}{\Delta x} \frac{v_n^w (1 - EX(v_n^e \Delta x)) - v_n^e EX(v_n^w \Delta x) (1 - EX(v_n^w \Delta x))}{(1 - EX(v_n^e \Delta x)) (1 - EX(v_n^w \Delta x))} + \frac{1}{\Delta y} \frac{v_n^n (1 - EX(v_n^s \Delta y)) - v_n^s EX(v_n^n \Delta y) (1 - EX(v_n^n \Delta y))}{(1 - EX(v_n^s \Delta y)) (1 - EX(v_n^n \Delta y))} + \frac{1}{\Delta z} \frac{v_n^t (1 - EX(v_n^b \Delta z)) - v_n^b EX(v_n^t \Delta z) (1 - EX(v_n^t \Delta z))}{(1 - EX(v_n^b \Delta z)) (1 - EX(v_n^t \Delta z))} \right)$$

$$\alpha_e = \frac{1}{\Delta x} \frac{-v_n^e (1 - EX(v_n^w \Delta x))}{(1 - EX(v_n^w \Delta x)) (1 - EX(v_n^e \Delta x))} \quad \alpha_w = \frac{1}{\Delta x} \frac{v_n^w (1 - EX(v_n^e \Delta x))}{(1 - EX(v_n^e \Delta x)) (1 - EX(v_n^w \Delta x))}$$

$$\alpha_s = \frac{1}{\Delta y} \frac{-v_n^s (1 - EX(v_n^n \Delta y))}{(1 - EX(v_n^n \Delta y)) (1 - EX(v_n^s \Delta y))} \quad \alpha_n = \frac{1}{\Delta y} \frac{v_n^n (1 - EX(v_n^s \Delta y))}{(1 - EX(v_n^s \Delta y)) (1 - EX(v_n^n \Delta y))}$$

$$\alpha_b = \frac{1}{\Delta z} \frac{-v_n^b (1 - EX(v_n^t \Delta z))}{(1 - EX(v_n^t \Delta z)) (1 - EX(v_n^b \Delta z))} \quad \alpha_t = \frac{1}{\Delta z} \frac{v_n^t (1 - EX(v_n^b \Delta z))}{(1 - EX(v_n^b \Delta z)) (1 - EX(v_n^t \Delta z))}$$

where to achieve a more compact notation we have introduced the function  $EX(v_n^c \zeta) = \exp\left(-\frac{v_n^c \zeta}{D_n^c}\right)$

The analogous equation system for the hole density in the  $P$  and its neighbor cells is

$$\alpha'_p p_p - \sum_c \alpha'_c p_c = qM_P \quad (2.70)$$

with similar expressions for the  $\alpha$  coefficients.

In conclusion, Eqs.(2.61, 2.69 and 2.70) can be regarded as a  $3N$  linear system equations, where  $N$  is the number of cuboids. However, we remember that the values for the electron and hole diffusion constant and mobility, together with the recombination terms entering the equation system are also function of the carrier densities. As a consequence, a self-consistent procedure must be used to calculate  $n, p$ , and the electrostatic potential  $\Phi$ . Therefore, at each discrete step  $t$  of this iterative procedure, the output values from the previous step  $\Phi_{t-1}, n_{t-1}, p_{t-1}$  are used to calculate the coefficients of the equation system defined by Eqs.(2.61, 2.69 and 2.70), whose solution returns the actualized  $\Phi_t, n_t, p_t$  values. To this aim, at each step also the quasi-Fermi levels in the valence and conduction band need to be evaluated in order to asses the recombination rate. The iterative procedure stops when the relative variation of  $\Phi_t, n_t, p_t$  with respect to the previous step in all the cells remains lower than a fixed threshold, usually set at  $10^{-5}$ .

As concluding remarks, we notice that in our simulations the focal position of the pump laser

beam scans a region of the sample which, referring to the scale given by the excess carrier diffusion length, is well separated from the rim contacts  $\Gamma_1$  and  $\Gamma_2$ , placed at the two sample boundaries. For this reason we can assume that the carrier densities at the contacts keep their equilibrium values.

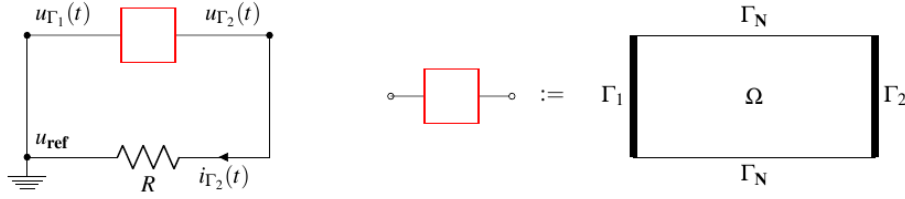


Fig. 2.8: Scheme of the closed circuit configuration.

Moreover, the potential in the contact area must remain constant, and we chose to set it to zero at the  $\Gamma_1$  side. Under CW illumination and in the closed circuit configuration the current flows along the  $\Gamma_1$ - $\Gamma_2$  shown in Fig. 2.8 direction while no contribution to  $J$  comes from the other sample surfaces ( $\Gamma_N$ ). Another consistency check that can be performed at the end of a simulation is given by the spatial invariance of the  $\int_{\partial\Omega} \mathbf{J} \cdot \mathbf{n} dS$  integral, representing the total current flowing through any sample section between  $\Gamma_1$  and  $\Gamma_2$ .

Finally, for what concerns the mesh geometry, both uniform and inhomogeneous grids have been tested. In the first case, one can benefit from the fact that once the mesh has been defined, it can be used to simulate the photo-induced voltage for an entire set of focal spot positions. However, since the excitation is mainly localized in a neighbor of the laser spot, an adaptive inhomogeneous mesh, is more suitable to increase the numerical precision. To this aim non-uniform grids centrosymmetric with respect to the focal point, as the representative one shown in Fig. 2.9, have been calculated. The cons of this choice is related to the fact that for each focal point a new mesh must be computed. To precisely describe effects related to the  $z$ -dependence of the excitation density, we rely on 3D grids which in the adaptive case are chosen finer close to the top surface (see Fig.2.9) since both the penetration depth and the diffusion length are much smaller than the typical sample thickness.

## 2.4.2. Matrix Solver

To conclude the discussion of the discretization procedure adopted in our model, we briefly comment on the numerical recipe adopted to solve the  $3N$  linear equation system. Since Eqs.(2.61, 2.69 and 2.70) are associated to sparse matrices due to the fact that only neighbor cells are coupled, to efficiently perform the matrix inversion we rely on the **M**Ultifrontal **M**assively **P**arallel **S**olver-MUMPS[ADLK01, AGLP06]. MUMPS solve linear equations systems  $\hat{A} \cdot \mathbf{x} = \mathbf{b}$  using a direct method based on a multifrontal approach which performs a Gaussian factorization

$$\hat{A} = \hat{L} \cdot \hat{U} \quad (2.71)$$

where  $\hat{L}$  is a lower triangular matrix and  $\hat{U}$  an upper triangular matrix. To this aim three main steps are required: i) Analysis; ii) Factorization, and iii) Solution.

**Analysis** In this step an ordering on the symmetrized pattern  $\hat{A} + \hat{A}^T$  and a symbolic factorization takes place. A mapping of the multifrontal computational graph, named elimination

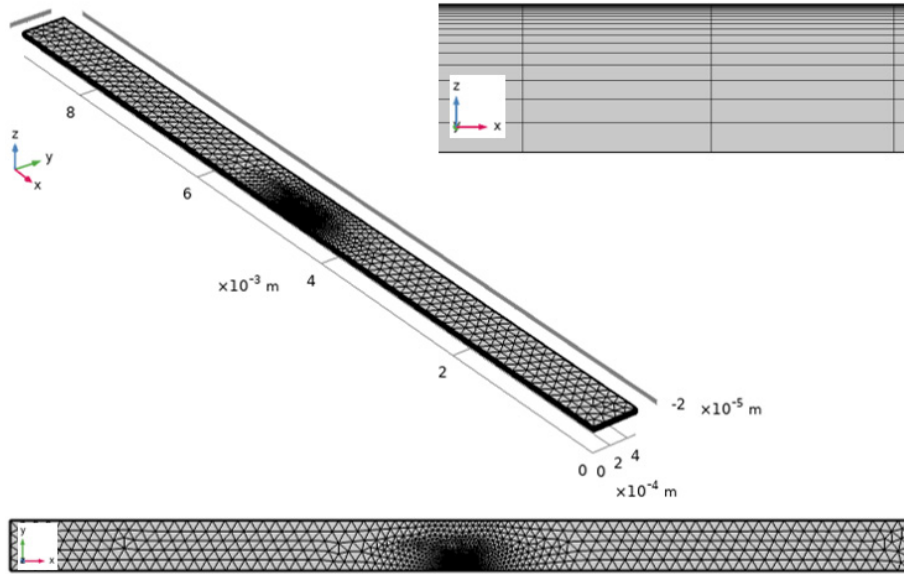


Fig. 2.9: Schematics of a representative non-uniform grid used in the simulations. Notice that the grid is more dense in the neighbor of the focal point set at  $P(4.5 \text{ mm}, 0 \text{ mm}, 0 \text{ mm})$ . The  $y \rightarrow -y$  is exploited to reduce the simulated volume by a factor of two.

tree, will be created during this factorization. Using this elimination tree, the algorithm estimates the number of operations and memory necessary for the factorization and solution. The preprocessed matrix  $\hat{A}_{\text{pre}}$  is here defined.

**Factorization** Now  $\hat{A}_{\text{pre}} = \hat{L} \cdot \hat{U}$  is computed with numerical factorization, which are sequences of dense factorization on frontal matrices. The following pivoting can be done in three different ways: standard pivoting, two-by-two-pivoting and static pivoting. For each factorization the algorithm decides which method is chosen according to the associated values of the elimination tree, hence the name "multifrontal approach".

**Solution** Using the factor matrices obtained within the factorization process, the solution  $\mathbf{x}_{\text{pre}}$  of  $\hat{L} \cdot \hat{U} \cdot \mathbf{x}_{\text{pre}} = \mathbf{b}_{\text{pre}}$  is obtained. Here  $\mathbf{x}_{\text{pre}}$  and  $\mathbf{b}_{\text{pre}}$  are associated to  $\hat{A}_{\text{pre}}$ . The solution is calculated by means of a forward elimination step  $\hat{L} \cdot \mathbf{y} = \mathbf{b}_{\text{pre}}$  and subsequently a backwards elimination step  $\hat{U} \cdot \mathbf{x}_{\text{pre}} = \mathbf{y}$ . Through the final post processing of  $\mathbf{x}_{\text{pre}}$ , the solution  $\mathbf{x}$  of the original linear equation system (2.71) is obtained. Finally, an iterative refinement and an error estimation process of the backward elimination step can be used to increase the numerical quality of the solution.

## 2.5. Sample Preparation and Measurement Set-up

The LPS set-up used in this work is schematically illustrated in Fig. 2.10. Measurements are performed at room temperature in air. The investigated Si samples are prepared to have parallel top and bottom surfaces lying in the  $xy$  plane. Rim ohmic contacts are fabricated at the two vertical surfaces indicated in Fig. 2.10. To this aim, the Si surfaces are first mechanically ground to remove the native oxide. Subsequently, an eutectic  $\text{Ga}_{0.75}\text{In}_{0.25}$  [CWDW08, AA91]) layer is transferred to the surfaces before connecting the Si material with brass contacts. Since the eutectic  $\text{Ga}_{0.75}\text{In}_{0.25}$  work function (4.3 eV) is similar to the one of Si (4.6 eV), almost ohmic

behaviour is obtained. As will be seen later, it is advisable to always cover the whole Si surfaces with the indium-gallium eutectic to avoid distorting measurement effects. The sample is fixed on top of a surface that can be shifted in the  $xy$  plane by means of computer controlled electrical engine and one of the two contact is grounded. Optical excitation is produced by means of a single mode well focused laser beam, impinging normal to the top surface with wavelength of 685 nm or 830 nm. The spot size close to the top surface is of the order of  $5\mu\text{m}$  and the output power can be increased up to 170 mW, corresponding to a maximum power density of  $5400\text{ W/cm}^2$ . Notice that large laser power may be necessary to achieve a sufficient signal to noise ratio, especially when measuring samples with very short excess carrier lifetimes. On the other hand, one has to keep in mind that large laser power negatively affect the LPS spatial resolution as extensively discussed in Chapter 4.

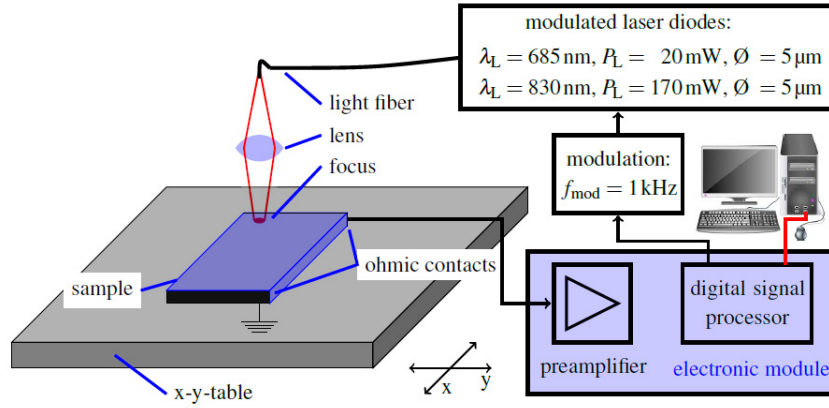


Fig. 2.10: Scheme of the used LPS-measurement set-up.

Moving the spot position  $(x_f, y_f)$  across the sample surface a photogenerated voltage map is recorded through a customized control software (see Fig. 2.11) using lock-in amplification (see Fig. 2.12). The associated image features a tunable spatial resolution  $(\Delta x, \Delta y)$ , which has to be chosen much smaller than the physical resolution of the LPS measurement. The user can define a time constant  $\Delta t$ , which controls the number of acquired data point  $N$  per pixel according to the relation  $N = \Delta t \cdot f_{\text{mod}}$ , where  $f_{\text{mod}}$  is the frequency of the lock-in amplifier. The shift velocity along the  $x$ -direction of the movable table is then automatically set at  $v = \Delta x / \Delta t$  and the map is acquired as an array of 1D  $x$ -scan lines, separated by  $\Delta y$ . It follows that each pixel of the LPS map image represent the average of  $N$  different measurements. A typical wafer scale experiment features  $\Delta x = 100\mu\text{m}$ ,  $\Delta y = 100\mu\text{m}$ ,  $\Delta t = 25\text{ ms}$ , resulting in a total acquisition time of 7h to map a surface area of about  $10\text{ cm} \times 10\text{ cm}$  with  $N = 25$  independent data points for each pixel.

We conclude this chapter showing in the left panel of Fig. 2.13 a typical grey-scale LPS map acquired with a n-type FZ-Si sample featuring an average resistivity of  $\rho \approx 80\Omega\text{cm}$ . In Fig. 2.13 the resistivity inhomogeneities associated to the dynamics of the solid-liquid interface manifest themselves as striations with lighter (darker) regions corresponding to a positive (negative) component of the doping gradient along the  $x$ -direction. The observed curvature of the striations can be directly compared with numerical data for the temperature field, obtained when simulating the FZ growth process Fig. 2.13. As a simplified case we show in the right panel of Fig. 2.13 the calculated temperature field for a similar FZ-Si sample, where the bold isoline represents the position of solid-liquid interface at a certain time. This can be compared to the tracked isolines in the LPS map, as the resistivity variations manifest themselves in the shape of the solid-liquid-interface (see central panel of Fig. 2.13).

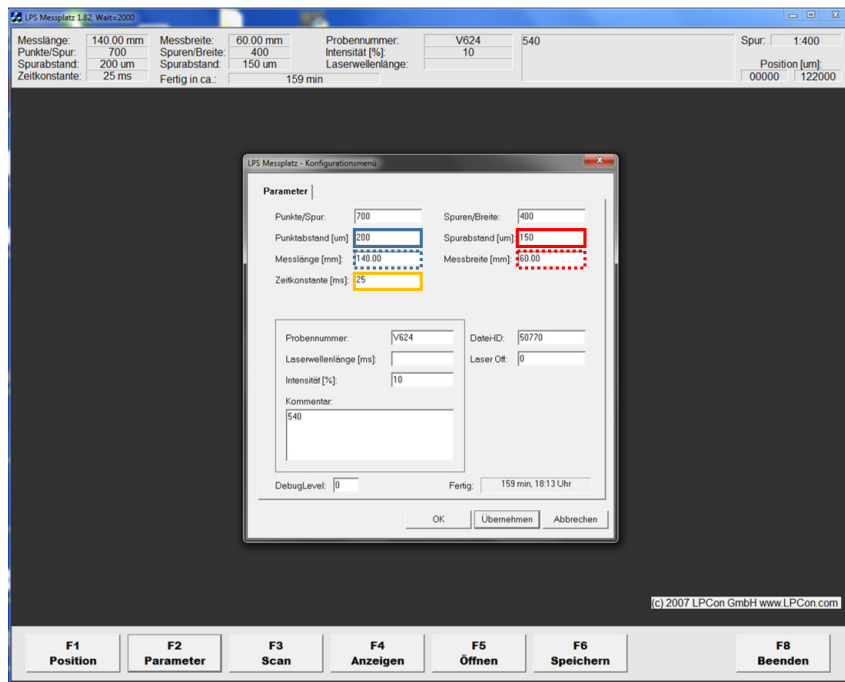


Fig. 2.11: Graphical interface for the software which controls the acquisition of the LPS voltage signal. The windows allows to set  $\Delta x$ ,  $\Delta y$ ,  $\Delta t$ , and the dimensions of the scanned area.

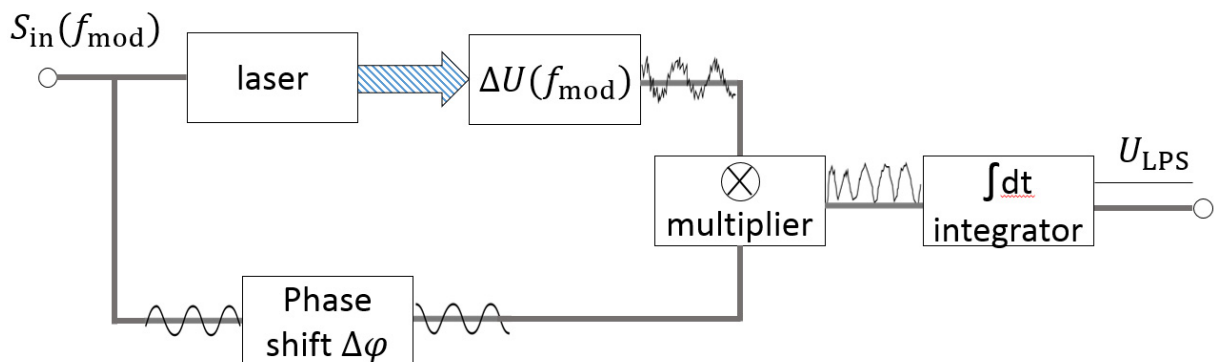


Fig. 2.12: Scheme of the lock-in-technique used to improve the signal-to-noise ratio when acquiring the photogenerated voltage signal.  $S_{in}$  is the lock-in modulation signal and the  $\Delta U$  is the modulated voltage difference between the rim contacts.

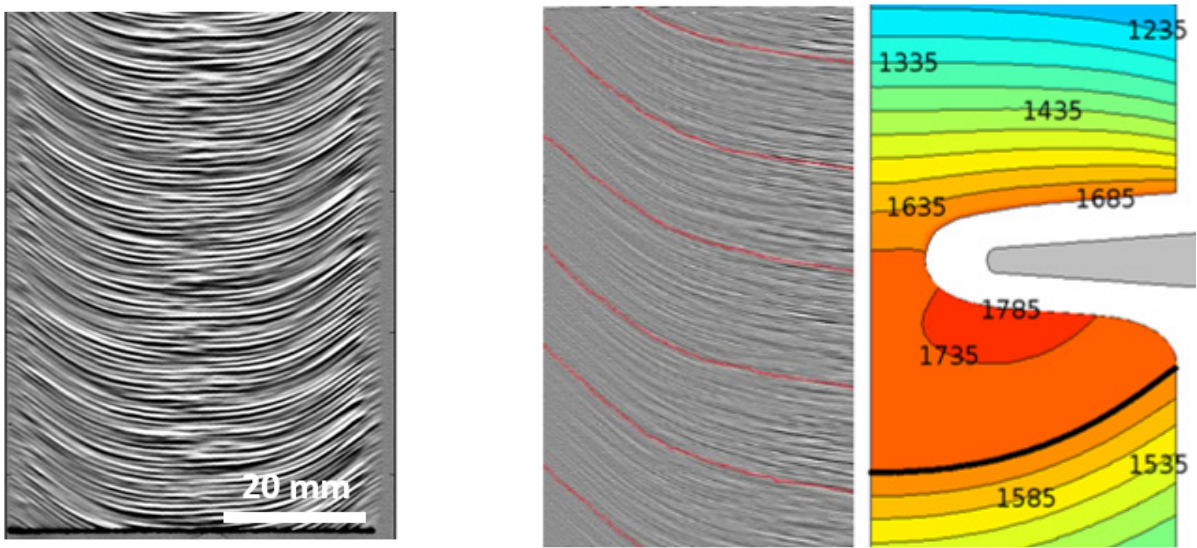


Fig. 2.13: Left panel: LPS map of a FZ-Si n-type sample showing the typical striation pattern associated to the solid-liquid interface dynamics. Central panel: LPS map with a tracked iso-lines marked in red. Right panel: simulated temperature field (K) at a given time during the growth process. The bold isoline represents the position of the solid-liquid interface. Additionally shown in grey is the heat inducing inductor coil.

# Chapter 3

## Signal Generation and Transmission

This chapter will show a way to deal with a coming up scaling problem. A typical limiting factor is the used laser spot, implemented as a 2D Gaussian function with  $\sigma_L = 1.25 \mu\text{m}$ , which has to be resolved properly by the mesh. On the other hand, the sample sizes can easily reach length scales of about 30cm. Even using a mesh geometry as introduced in Fig. 2.9, will not deal with this problem on an effective computational time scale.

Therefore the idea of separating the problem is introduced. A first main program will deal with the signal generation on a small suitable scale. Signal generation means to solve the van Roosbroeck Eq. system (2.26-2.28), detecting the potential difference at the edges of this small sample. Another program, which will be introduced later, will use this potential difference as an input parameter and will solve for the potential difference at the large sized sample edges.

### 3.1. Proof of Principle of the Signal Generation Program

The following section contains measurements, results and figures already published [KLB18]. As basic proof of the model, we show that a voltage difference between the sample edges is generated in an inhomogeneous Si sample by an applied laser. Therefore discussed is the simplest case, which can be described by using Taucs Eq. (2.19). Here a homogeneous Si sample is assumed with a linear gradient of the doping distribution. As opposed to the homogeneously illumination assumed by Tauc, we are investigating a local illumination by a focussed laser in the shape of a two dimensional Gaussian distribution. Tauc described that the bulk photovoltaic effect is proportional to conductance variation:

$$U_{LPS} \propto \nabla_x \frac{1}{\rho} = \nabla_x q(\mu_n n + \mu_p p). \quad (3.1)$$

In the case of an  $80 \Omega\text{cm}$  phosphorous doped sample we can assume that,  $N_D \approx n \gg p$  which reduces the former formula to:

$$U_{LPS} \propto q\mu_n \nabla_x N_D. \quad (3.2)$$

For the subsequent analysis, the electron mobility was kept constant.

The crystal is assumed to have a doping profile of phosphorus, caused by segregation  $N_{D, \text{seg}}$ , which is characterized by a macroscopic gradient along the sample length and by local fluctuations. This profile is modelled by the formula:

$$N_D^+ = N_{D, \text{seg}} + N_{D, \text{fluct}} = N_{D,0} \left( 1 + \frac{a}{L}x + b \cdot f(x,y,z) \right), \quad (3.3)$$

where  $N_{D,0}$  is the background level of the dopant concentration,  $L = 2.4\text{mm}$  is the sample length,  $x$  the length coordinate,  $a$  a control parameter for setting the macroscopic gradient of the dopant profile. The fluctuations of the doping concentration caused by temperature inhomogeneities are assumed as sinusoidal and reduced by the prefactor  $b = 1 \times 10^{-5}$ . The constant macroscopic gradient of the dopant profile, i.e. the linear behaviour of the profile, is assumed due to the small sample length: indeed there is a rather exponential distribution due to the segregation of, e.g., phosphorus in the melt during crystal growth.

The computation of the simulated LPS-voltage is shown in Fig. 3.1 left panel for different values of the control parameter  $a$ . During this, the focus of the laser has moved between  $x_f \in 0.9 - 1.2\text{mm}$ . The computation yields a nearly constant LPS-voltage for each  $a$ -value when  $x_f$  was varied.

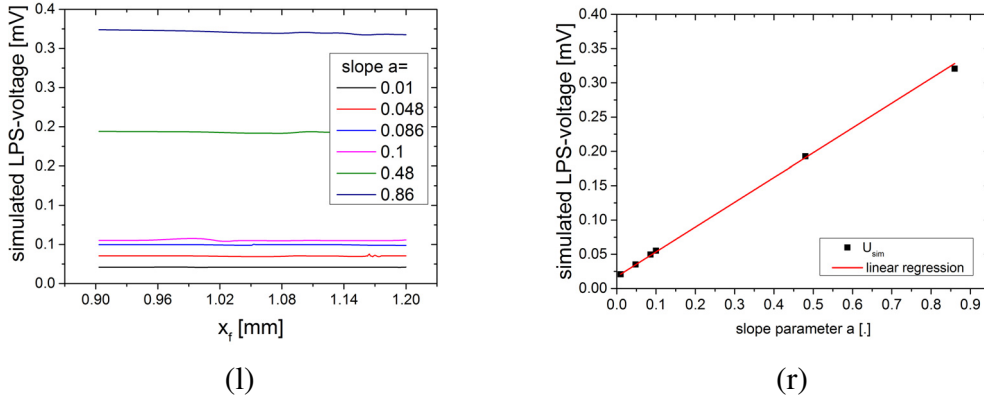


Fig. 3.1: Left panel: result of the simulations of the LPS-voltage relative to the parameter  $a$ . Right panel: dependency of the simulated LPS-voltages on the slope parameter  $a$ [KLB18].

Fig. 3.1 right panel shows the proportionality between the simulated LPS-voltage and the gradient of the dopant profile  $a$ . Additionally, Fig. 3.1 right panel reveals an offset of the LPS-voltage for  $U_{\text{Sim}}|_{a=0}$ . In that case only the sin-shaped dopant fluctuations remain, hence, the offset cannot have physical reasons. Therefore, analysed is whether the offset depends on the model itself. Accordingly offset voltage will be discussed by enlarged sample width ( $> 150\mu\text{m}$ ) and thickness ( $> 2\mu\text{m}$ ). As shown in Fig. 3.2 left panel, enlarging the sample width by a factor of 10 reduces the offset roughly by the same factor, however, the reduction of the offset is not a linear function of the sample width.

The effect of the thickness on the offset is more complicated, see Fig. 3.2 right panel: as long as the sample thickness is below the penetration depth ( $15.4\mu\text{m}$ ), thickness enlargement increases the total number of charge carriers and the offset voltage is rising. But even before reaching the saturation of the total number of charge carriers, which may be reached at a thickness  $\approx 3 \cdot 15.4\mu\text{m}$ , where 95% of the charge carriers are absorbed, the offset decreases. The enlargement from the rather small thickness ( $2\mu\text{m}$ ) with maximum offset ( $\approx 9\mu\text{m}$ ) to a thickness of  $200\mu\text{m}$  reduces the offset by a factor of eight. In the last case, the sample thickness is much larger than the penetration depth of the laser, hence the non-reflected energy of the laser is absorbed (99.9998%) by the semiconductor and transmission is highly suppressed. Combining the increased thickness and width of the sample, the offset is reduced by a factor of 80 and, thus is negligible. The linear dependency of the simulated LPS-voltage on  $a$  and the knowledge that  $U_{\text{LPS}} \propto \nabla_x N_{\text{D}}^+$  allows the following relation:

$$U_{\text{Sim}} \propto a \propto \nabla_x N_{\text{D}}^+ \propto U_{\text{LPS}} \quad (3.4)$$



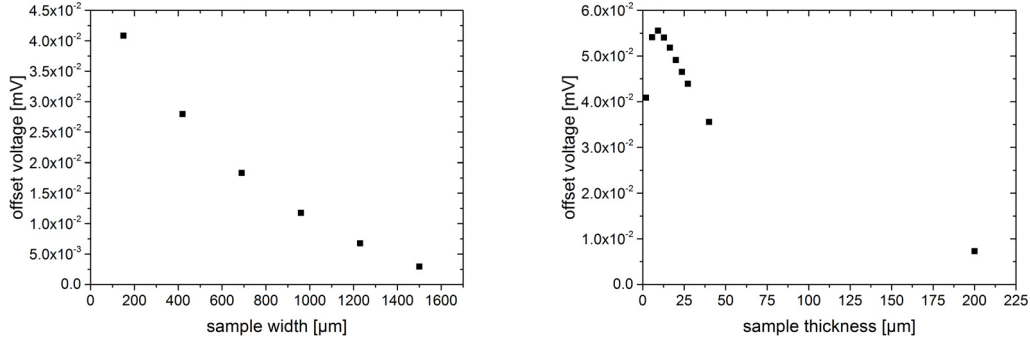


Fig. 3.2: Left panel: behaviour of the offset with respect to the width of the simulated sample. Right panel: dependency of the offset from the sample thickness. After an increase related to the penetration depth of the laser, a decreasing trend is visible [KLB18].

As could be seen, the simulated LPS-voltage is proportional to the theoretical description by Tauc. A concern is, that the simulated sample size is in the order of millimetres but usually sample sizes occur in the order of several centimetres as wafers or plates. Here the question occurs whether the sample size and/or the shape influence the LPS measurements. Also interesting is whether there is an influence of the detection of the LPS-voltage to the measurement signal. Therefore, it is necessary to separate the generation of the LPS-voltage to its detection, which will be discussed now.

## 3.2. Signal Transmission

To analyze larger sample sizes, we have to reduce the model. Therefore we assume:

- The generation of the LPS-signal takes place in a local area around the focal point.
- In this region we have already solved the van-Roosbroeck equation system.
- The remaining Si sample behaves as a passive electrical device.

### 3.2.1. Model

Especially the last point leads to a conductance for n-type Si

$$\sigma_{\text{Si}}(x, y) = q \left( \mu_p \frac{n_i^2}{n} + \mu_n n \right) = \text{const}, \quad (3.5)$$

which reduces the equation system essentially. We can use electrical circuit equation systems to solve for. This requires the current conservation  $\nabla \mathbf{J} = 0$ . Here  $\mathbf{J}$  describes the current density through all devices in the circuit. The Poisson equation is reduced to  $\mathbf{E} = -\nabla \Phi$  and connected by the Ohms law to the conductance  $\mathbf{j} = \sigma \mathbf{E}$ .

A reduced two dimensional model is shown in Fig. 3.3. The Si sample is marked in blueish colour, the Cu wires in grey and the inner resistance of the volt meter detecting the LPS-voltage in red. The white central rectangle is the area where we already solved the van Roosbroeck equations using the method shown in the former section. So the potential

difference of the generated dipole is known and included as  $\Phi_{in}$ . The potential of the other edge is set to the ground level. The centre of this area is defined as the former focal point  $P_f(x_f, y_f)$  of the laser.

The Si sample is connected by ohmic contacts to Cu wires, which closes the electric circuit to the inner resistance of the volt meter:

$$U_{LPS,2D} = \overline{\Phi}|_{\Gamma_1} - \overline{\Phi}|_{\Gamma_2}. \quad (3.6)$$

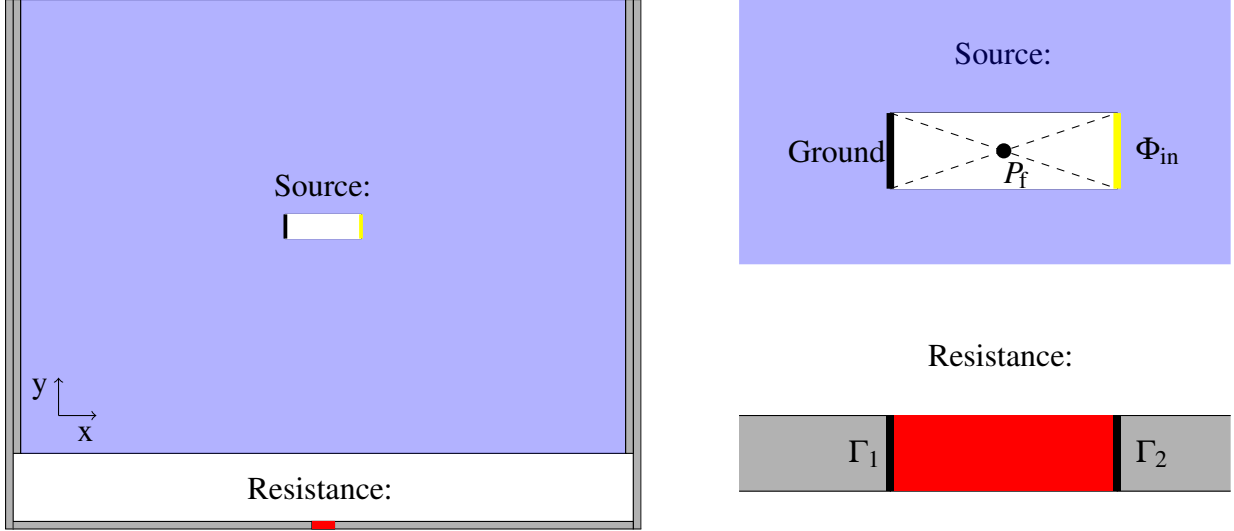


Fig. 3.3: Two dimensional model of the LPS measurement setup. The silicon sample is marked blue, the copper wires in grey and the inner resistance of the volt meter in red.

As boundary condition ohmic contacts between Si, Cu and the inner resistance are assumed. The electric potential shall be  $0 = \Phi|_{\text{Ground}}$  and  $\Phi_{in} = \Phi|_{\text{Source}}$ . The remaining boundaries are treated as isolated rims  $0 = \mathbf{n} \cdot \mathbf{j}$ .

### 3.2.2. Basic Analysis

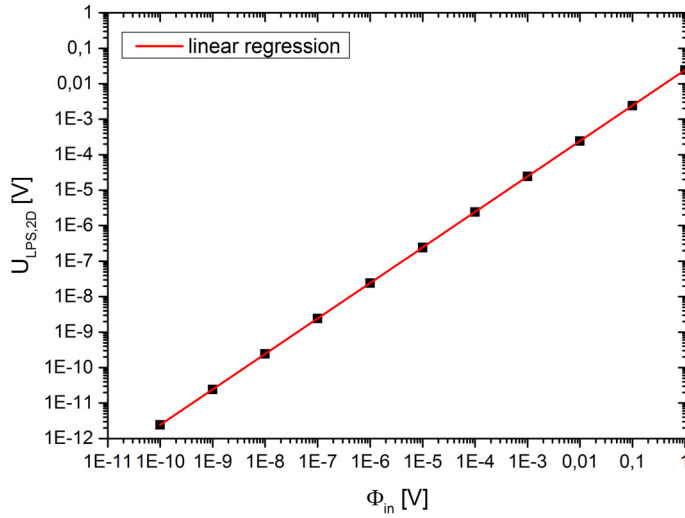
We start with basic analysis of the model, which are required for further investigations. At first we are looking at the influence of the dipole strength represented by the  $\Phi_{in}$  on the  $U_{LPS,2D}$ . In Fig. 3.4 a linear behaviour in a double logarithmic scale already proves for twelve orders of magnitude a functional dependency like:

$$U_{LPS,2D} = c_1 \cdot \Phi_{in}^{c_2} \quad (3.7)$$

Here  $c_1$  and  $c_2$  are constants. If we also consider figure (3.5), we can determine  $c_1 \approx 0.025$  and  $c_2 = 1$ . This linear behaviour is desirable due to the fact, that influences on the dipole strength  $\Phi_{in}$  directly influence the measured voltage  $U_{LPS,2D}$  and vice versa. The measurability of  $U_{LPS,2D}$  can be considered as a lower boundary of the measurability of the LPS-voltage. In this way it is preferable to have a large  $c_1$ , which correlates to the transmission losses  $\Phi_{in} \rightarrow U_{LPS,2D}$ .

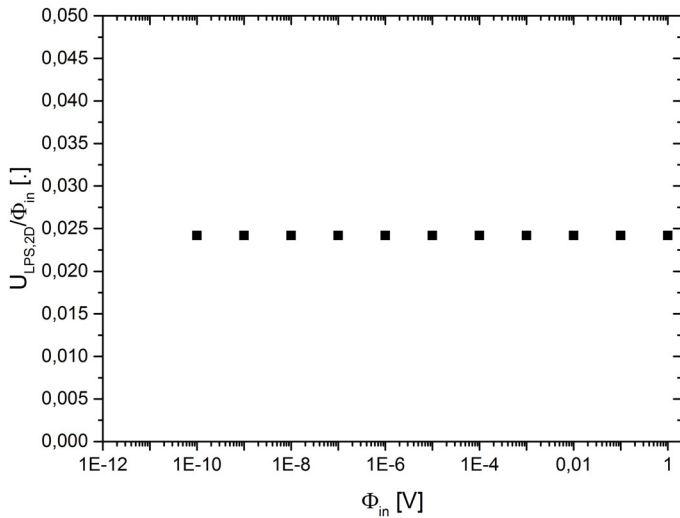
The open questions are:

- Where does this losses come from?
- What influences this transmission losses?



Symbol	Value
$L$	20 cm
$B$	15 cm
$\Phi_{in}$	
$\sigma_{Si}$	7.4 S/m
$\sigma_{Cu}$	$6 \times 10^7$ S/m
$\sigma_R$	$1 \times 10^{-6}$ S/m
$x_f$	$L/2$
$y_f$	$B/2$
shape	rectangular

Fig. 3.4: Dependency of  $U_{LPS,2D}$  on the dipole strength represented as  $\Phi_{in}$ .



Symbol	Value
$L$	20 cm
$B$	15 cm
$\Phi_{in}$	
$\sigma_{Si}$	7.4 S/m
$\sigma_{Cu}$	$6 \times 10^7$ S/m
$\sigma_R$	$1 \times 10^{-6}$ S/m
$x_f$	$L/2$
$y_f$	$B/2$
shape	rectangular

Fig. 3.5: A constant behaviour is visible, which reveals a linear dependency of  $\Phi_{in}$  to  $U_{LPS,2D}$

In Fig. 3.6 there is shown the used 2 dimensional model as a scheme. A voltage measurement is assumed to be currentless, which is realized by a large inner resistance. This also means, that in the Si sample closed current lines are formed, which can be seen in the vectorial sketch of the currents inside of the Si sample in Fig. 3.6. As a current is equalizing potential differences, this closed current lines diminish the potential difference at the ohmic contacts, which is equal to  $U_{LPS,2D}$ , because of the extremely high conductance of Cu used as contact material.

This example is shown for a homogeneous conductance for the Si sample, which seems to oppose the generation of the dipole, which is generated due to conductance inhomogeneities. As seen before, the inner closed current lines define the measured potential difference at the ohmic rim contact. With the assumption, that the gradient of the conductance is low in scales of the dipole length ( $\sigma_{\text{Si}}(x) \approx \sigma_{\text{Si}}(x+l)$ ), a linear change in conductance does not effect circular currents inside of the Si sample and hence the  $U_{\text{LPS},2\text{D}}$ .

So this two dimensional model can be used also for samples with a small macroscopic gradient, as they often occur in length cuts of doped Si crystals. Here segregation effects in the melt influence the incorporation of doping atoms, which can be estimated mostly by using linear functions.

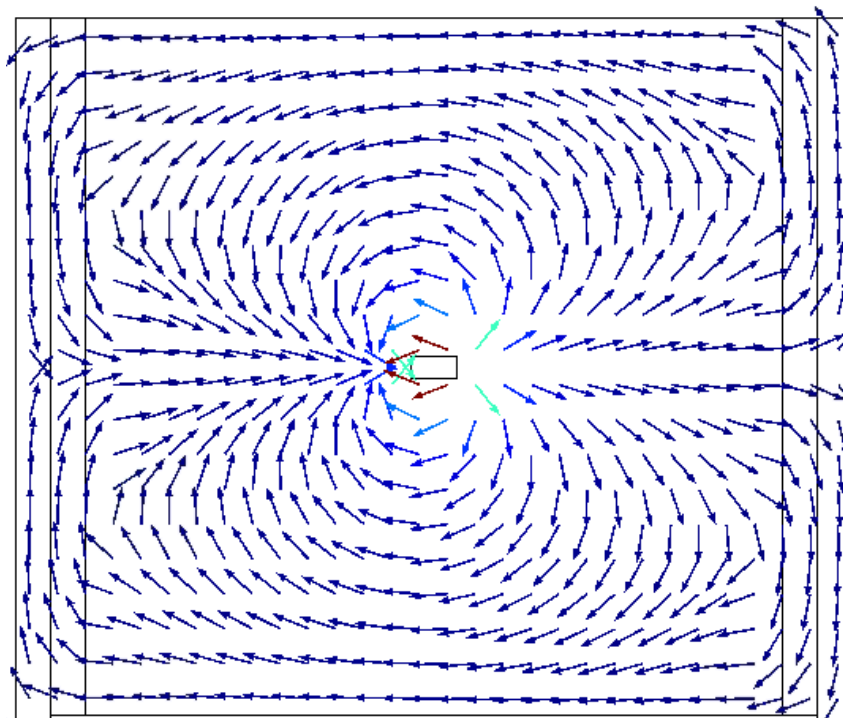


Fig. 3.6: Sketch of the current lines in the Si sample. Here the colour of the vector indicates the strength of the current at that area. Red is set to a high and dark blue to low current.

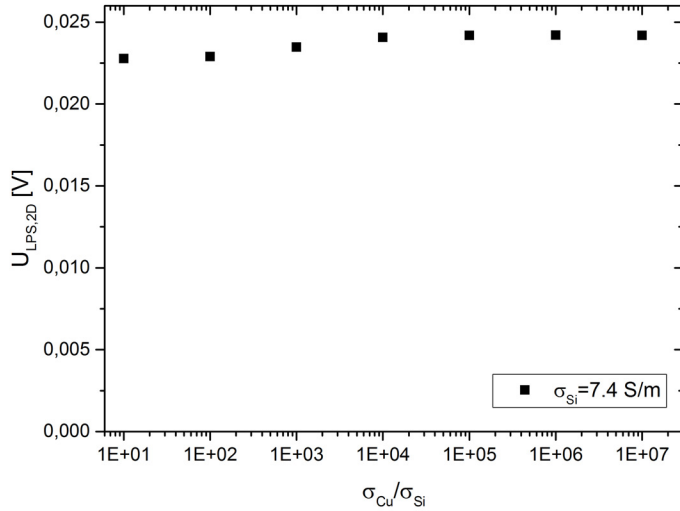
With this argumentation, that the inner current lines define the measurable  $U_{\text{LPS},2\text{D}}$  we expect no influence by different resistivity of the sample. To verify this assumption, we have to split the analysis in two parts by numerical reasons:

$$U_{\text{LPS},2\text{D}} \stackrel{?}{=} f(\sigma_{\text{Cu}}) \quad \text{with constant } \sigma_{\text{Si}} \quad (3.8)$$

$$U_{\text{LPS},2\text{D}} \stackrel{?}{=} f(N_{\text{A}}) \quad \text{with constant } \sigma_{\text{Si}}/\sigma_{\text{Cu}}. \quad (3.9)$$

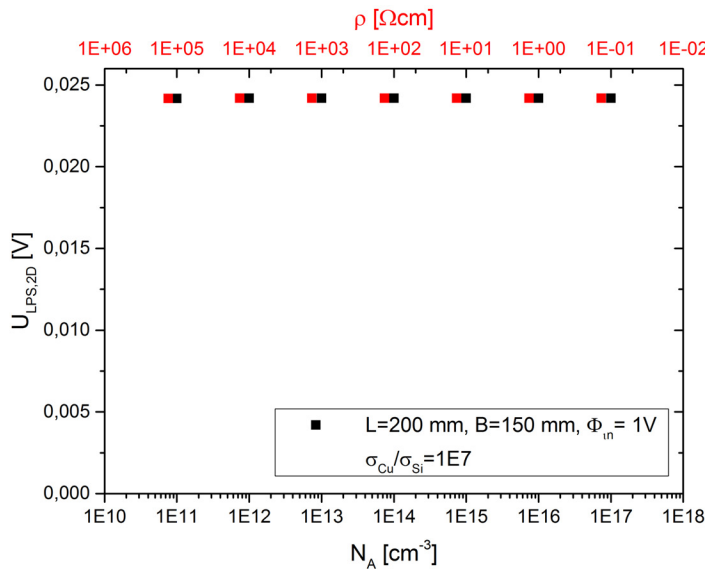
Fig. 3.7 shows the analysis of the dependency described in Eq. (3.8). Just a slight negligible dependency occurs. This can be described by Fig. 3.6. Here two types of closed inner circle lines occur, lines which attach the Cu contact, lines which are closed inside of the Si sample. The ratio of both changes minimally by increasing the conductance of Cu, which is the effect seen in Fig. 3.7.

The dependency of equation (3.9) is shown in figure (3.8), where a constant behaviour is manifested.



Symbol	Value
$L$	20 cm
$B$	15 cm
$\Phi_{in}$	1 V
$\sigma_{Si}$	7.4 S/m
$\sigma_{Cu}$	
$\sigma_R$	$1 \times 10^{-6}$ S/m
$x_f$	$L/2$
$y_f$	$B/2$
shape	rectangular

Fig. 3.7: Dependency of the two dimensional LPS-voltage with respect to the Cu conductivity normalized by the Si conductivity.



Symbol	Value
$L$	20 cm
$B$	15 cm
$\Phi_{in}$	1 V
$\sigma_{Si}$	
$\sigma_{Cu}$	$6 \times 10^7$ S/m
$\sigma_R$	$1 \times 10^{-6}$ S/m
$x_f$	$L/2$
$y_f$	$B/2$
shape	rectangular

Fig. 3.8: Dependency of the two dimensional LPS-voltage with respect to the doping concentration of Si. Here also a constant ratio of the conductances Cu/Si was kept constant.

The combined Fig. 3.7 and 3.8 clarify that the resistivity of the Si does not effect the signal transport, which fits to our assumption.

This shows, that the measurement set up is suited well for the detection of the photovoltaic effect. In addition the discussed two-dimensional model has been established well describing the effects. Now we are analysing proportional constant  $c_1$ , which can also be interpreted as the transmission coefficient of Eq. (3.7) with respect to the sample size. This means, we are looking whether some samples are better adapted to the LPS-measurement.

### 3.2.3. Sample Geometry Effects

In Fig. 3.9 the dependency of the  $U_{LPS,2D}$  with respect to the sample length (black) and width (red) is shown. In both cases a decreasing behaviour of  $U_{LPS,2D}$  with the sample size can be seen. As the black curve reaches a plateau after  $\approx 3$  mm, the red curve keeps decreasing constantly. A sample length in the region of the dipole length sets the potential (ground and source) directly on the ohmic contacts, which results consequently in  $c_1 = 1$ . Despite that edge effect no dependency of  $U_{LPS,2D}$  of the sample length is detectable.

The red curve also started with  $c_1 \approx 1$  in the millimetre region. This can be understood, due to the fact, that the two dimensional model then changes to a simple branchless circuit, where the current is preserved. This preserved current and the fact, that the resistance in the volt metre is much larger then all other remaining resistances result in the fact, that  $c_1 \approx 1$ .

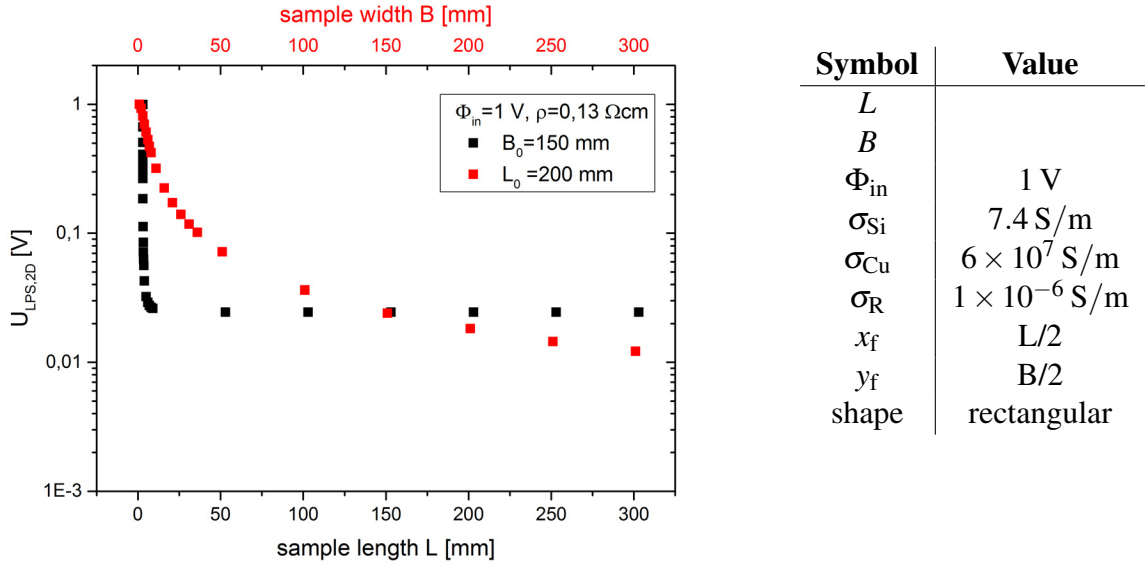


Fig. 3.9: Dependency of the two-dimensional simulated LPS-voltage with respect to the sample length (black) and the sample width (red).

The functional behaviour of  $U_{LPS,2D}$  with respect to the sample width can be seen in Fig. (3.10 left panel). Here  $B_S$  is the width of the dipole. A linear dependency is fitted with respect to the inverted sample width, resulting in:

$$c_1 = f(1/B). \quad (3.10)$$

With small changes to the model, we can also analyze the effect of the sample thickness. Therefore we have to change the focal point to  $P_f(L/2, B)$ , now the former y-direction (see Fig. 3.3) can be assumed as the sample thickness. The results of  $U_{LPS,2D}$  depending on the sample thickness are shown in Fig. 3.10 right panel. Here a linear dependency is determinable. Due to the small region, samples of interest have thickness lower than a millimetre, also a hyperbolic behaviour comparable to the dependency of the sample width can not be neglected. This can be shown here:

$$1 - ax = \sum_{n=0}^1 (-a)^n x^n \rightarrow \sum_{n=0}^{\infty} (-a)^n x^n = \frac{1}{1 + ax}. \quad (3.11)$$

So the same functional dependency can describe the shown effects. This seems to be logical as both (sample width and sample thickness) can be transferred into each other by a rotation of 90 degree.

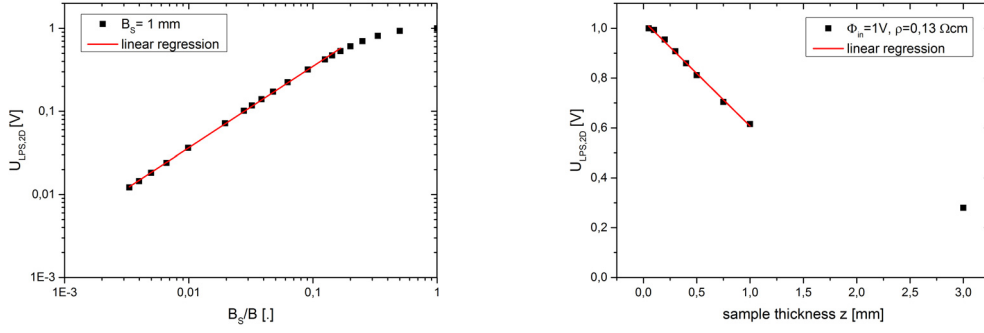


Fig. 3.10: Left panel: dependency of the simulated two dimensional LPS-voltage with respect to the sample width. Right panel: dependency of the simulated two dimensional LPS-voltage with respect to the sample thickness.

That means for a the measurability of LPS, which benefits from a large signal, that:

- thin samples are preferred,
- a low sample width is preferred
- and the sample length does not influence the measurement.

For an analysis of the shape of the solid liquid interface of a grown crystal, sample length and width are fixed by the crystal diameter and the length. But the thickness of the sample can be modified freely. So there is no reason for an LPS-measurement using thick samples.

Most samples used for LPS have two-dimensional geometric shapes of a rectangle (as length cuts of crystal), a circle (as wafers) and a trapeze (as cones of a starting/ending section of a crystal growth process). Interesting is, whether the geometric structure of the sample leads to specific characteristics with respect to the LPS-measurement. Also unknown is, whether the sample geometry will lead to a distorted measurement ( $c_1 = f(x_f, y_f)$ ). In this case, the functional behaviour is highly desired to rescale the distortion.

The results of this investigation are shown in Fig. 3.11 for a rectangular shaped sample. Here we show two central line scans (black  $y_f = B/2$ , red  $x_f = L/2$ ). Except the region close to the sample edges we could not determine an influence of  $c_1$  with respect to  $x_f$  or  $y_f$ , which also means no distortion in the measurement. But at the edges both dependencies behave differently. As we can see an increase in the  $U_{LPS,2D}$  depending on  $x_f$ , which is motivated by the fact, that a whole Cu contact will be set to the corresponding potential. In oppose  $U_{LPS,2D}$  decreases depending on  $x_f$ . Due to symmetry:

$$U_{LPS,2D}(B)|_{\text{edge}} = U_{LPS,2D}(2B) \xrightarrow{U_{LPS,2D} = f(1/B)} \frac{1}{2} U_{LPS,2D}(B). \quad (3.12)$$

As we have already shown:  $U_{LPS,2D} = f(1/B)$ . So how does a sample shape such as a symmetrical trapezoid ( $B = f(x)$ ) and circle effect the results shown for a rectangular structure?

To answer this open question we first analysed a wafer-like structure, sketched in Fig. (3.12 left panel). The radius of the shown circle is  $r = 75$  mm. The results of  $U_{LPS,2D} = f(x_f)$  along the diameter are plotted in black in Fig. (3.12 right panel). Here a monotonically increasing with respect to  $|x_f - r|$  can be seen. The red curve is normalized by the actual sample size, reveals a nearly constant behaviour. This result means for LPS-measurements on wafer, that the measurement is distorted, but can be rescaled.

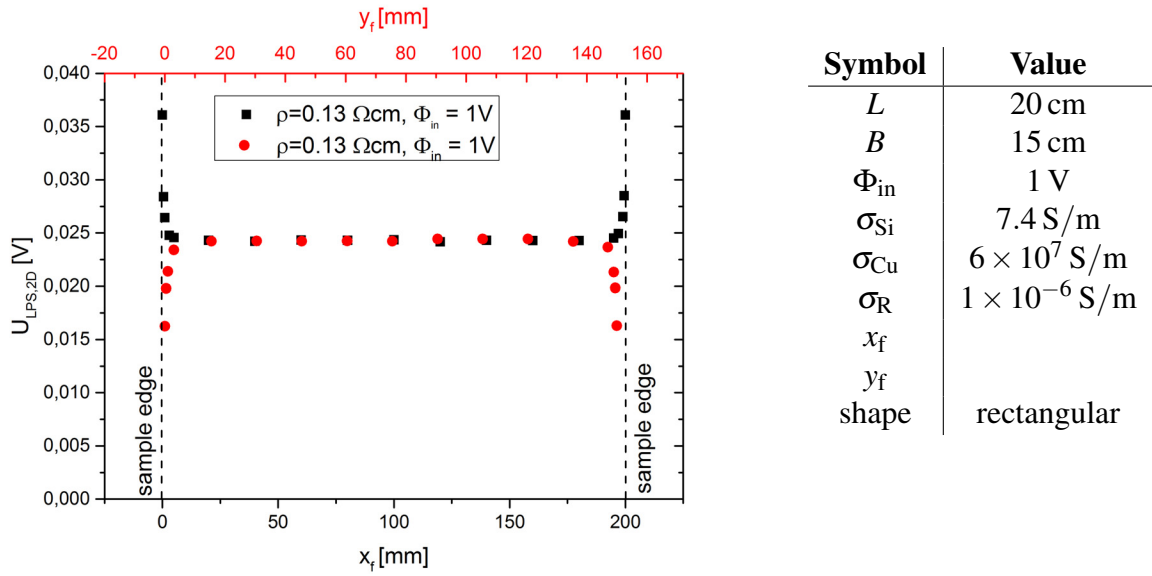


Fig. 3.11: Dependency of the two-dimensional LPS-voltage with respect to the observation (focal) point  $P(x_f, y_f)$ .

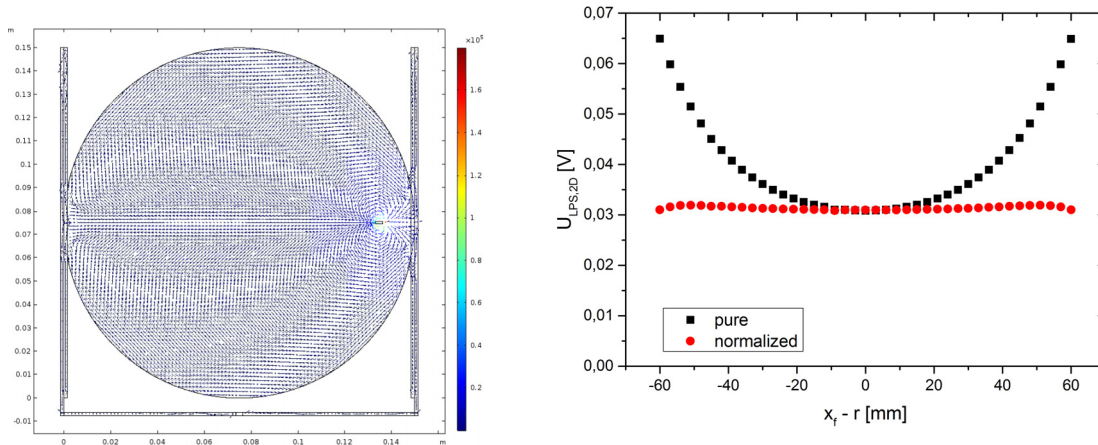


Fig. 3.12: Left panel: Sketch of the wafer-like sample set-up used in the two-dimensional model. Right panel: a line scan along the horizontal diameter was simulated (black). A LPS-voltage normalized by the local sample width is shown in red.

Analogously analysed is a trapezoid sample (hatched in grey) in figure (3.13). Here are also shown the results of  $U_{LPS,2D}$  pure (black) and normalized by the actual sample width (red). A non-linear increasing LPS-voltage width with decreasing sample width can be seen. This sample geometry leads to distorted LPS-measurements. The normalized results marked in red used the data point  $x_f = 180$  mm and normalized the remaining data point width the sample size. This results in a constant behaviour analogously to the rectangular case. Also the level is approximately the same as shown before.

To validate our model, we measured this effect. Therefore we used a length cut of an FZ Si ( $\rho = 80 \Omega\text{cm}$ ) using the 830 nm-laser. To avoid influences correlated to different sample length we used point-like contacts at the vertical centre of the edge. These LPS-measurements are shown in Fig. 3.14 left panel before and 3.14 right panel after cutting. Apart from edge effects



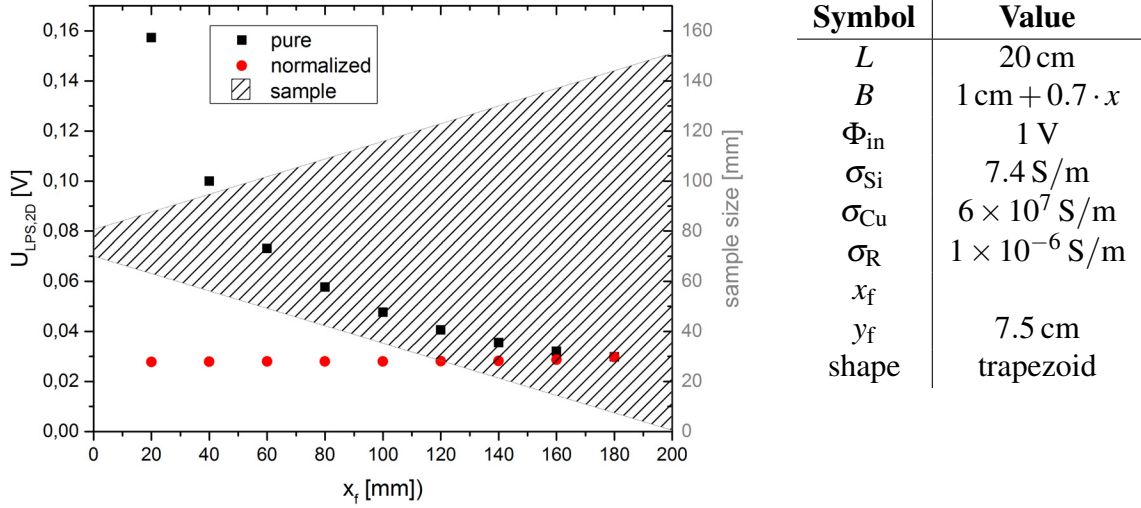


Fig. 3.13: Analysis of a trapezoidal sample (hatched in grey). The dependency of the two-dimensional LPS-voltage with respect to the observation (focal) point  $P(x_f, y_f)$ . The red dots represents a set of data, which is normalized by the local sample width.

in the left picture differences are hardly visible. This heavily relies on the gray scaling of the pictures. If we look at the standard deviation of the LPS-measurement along a horizontal central line, we get a better evaluation mark.

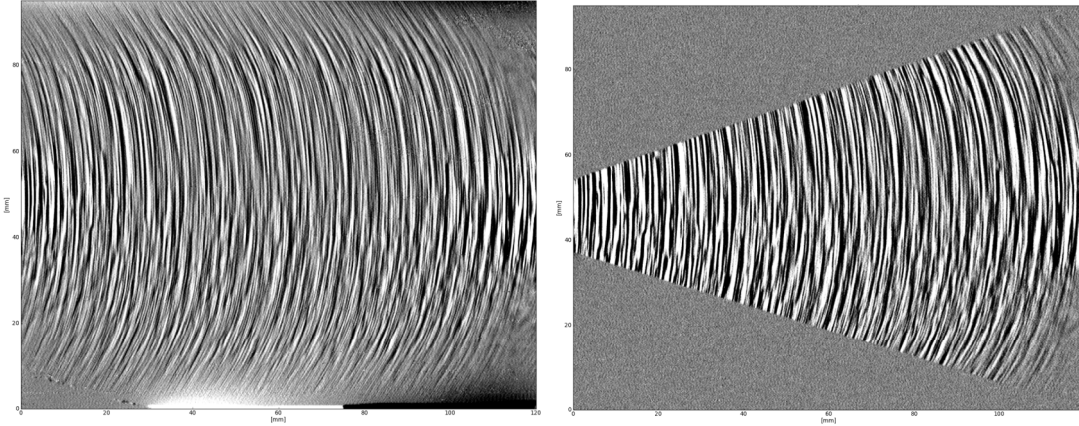


Fig. 3.14: Left panel: LPS-measurement of an  $80 \Omega\text{cm}$  sample with a rectangular shape  $100 \text{ mm} \times 120 \text{ mm}$ . Right panel: a repetition ( $(18 \text{ mm} - 100 \text{ mm}) \times 120 \text{ mm}$ ) of this measurement after cutting.

Analogously to the effective voltage of an accelerated current, we define:

$$U_{\text{eff}} = \text{std}(U_{\text{LPS}}) = \sqrt{\frac{1}{n} \sum_n (U_{\text{LPS}} - \overline{U_{\text{LPS}}})^2}. \quad (3.13)$$

To get still a local dependent value we evaluated the standard deviation for 80 consecutive measured LPS-voltages. This analysis is shown in Fig. 3.15 for a rectangular (black) and a trapezoidal (blue) sample geometry. In the region 30 mm - 100 mm the black curve stays constant in opposition to the decreasing behaviour of the blue curve. The red curve is scaled by

the actual sample width. In this region a good agreement between black and red curve can be seen. In the remaining regions, which are close to the sample edge the measurement signal is heavily increasing. This is what we have already shown and described in Fig. (3.11). The area of effect was some millimetres, here the range is about 20 mm - 30 mm on both edges. The behaviour at the right sample edge seems to be in good agreement. Also in this edge ranges the measurement results seem to depend on the y-coordinate. In the vertical centre of the sample, at the height of the contacts, the measurements seems to have a maximum, and is decreasing to vertical edges.

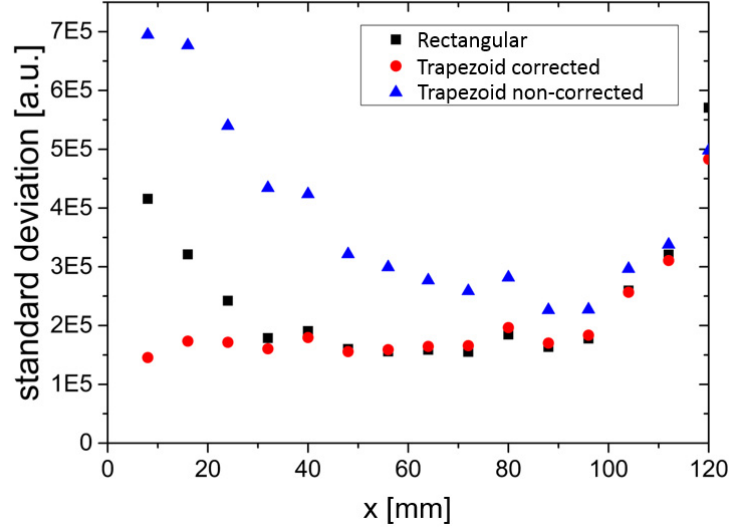


Fig. 3.15: Comparison measured LPS-voltage with respect to the sample geometry. The red curve contains a simulated correction factor described in figure (3.13).

### 3.2.4. Contacts

Results and considerations presented so far relate to contact applied to a full edge of the sample. For some sample geometries, dot-like contacts are of interest and their influence presented in the following. Therefore we adapted the described model as the following. In Fig. 3.16 left panel is sketched the current lines in the near of a point-like contact. In opposition to Fig. 3.7 the current lines are not closed by passing through the contact anymore. Just the short central contact, marked by an arrow, connects the sample to the inner resistivity.

For the further analysis we use the same set of parameters as used in Fig. 3.11. A central dot-like contact  $P_c(0\text{mm}, 75\text{mm})$  is located at the left edge. We first of all describe the horizontal behaviour at the same height as the contact, so  $y_f = 75\text{mm}$ . The results of  $U_{LPS,2D} = f(x_f)$  along this line are shown in Fig. 3.16 right panel. The region of effect, where  $U_{LPS,2D} \neq \text{const}$ , can be estimated with 0 mm - 40 mm. Compared to Fig. 3.11, the region of effect has heavily enlarged just by changing to a point-like contact. In comparison to the measurements shown in Fig. 3.15, where we measured this region to be approximately 0 mm - 30 mm, the simulation and measurements are in good agreement.

Finally we are looking at the measurement signal  $U_{LPS,2D} = f(y_f)$ . Therefore we are using a vertical line  $x_f = 25\text{mm}$ . The results of this investigation are shown in Fig. 3.17 left panel. Here a maximum is reached, at the centre of the sample, in which horizontal line the point-like

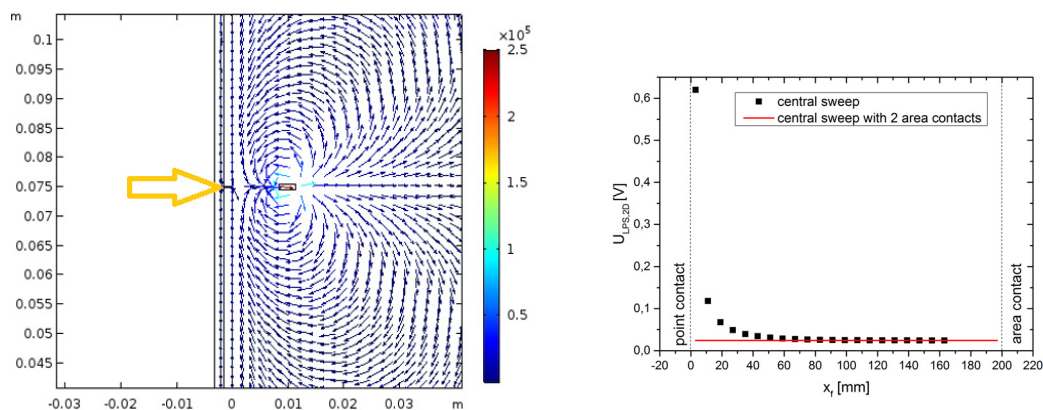


Fig. 3.16: Left panel: Sketch of a rectangular sample with a point-like contact. Right panel: horizontal line scan of the simulated LPS-voltage.

contact is located. This fits to the observation of the measurements in Fig. 3.11, where we have seen at the sample edges a decrease of  $U_{\text{LPS},2\text{D}}$  with increasing distance to the sample centre.

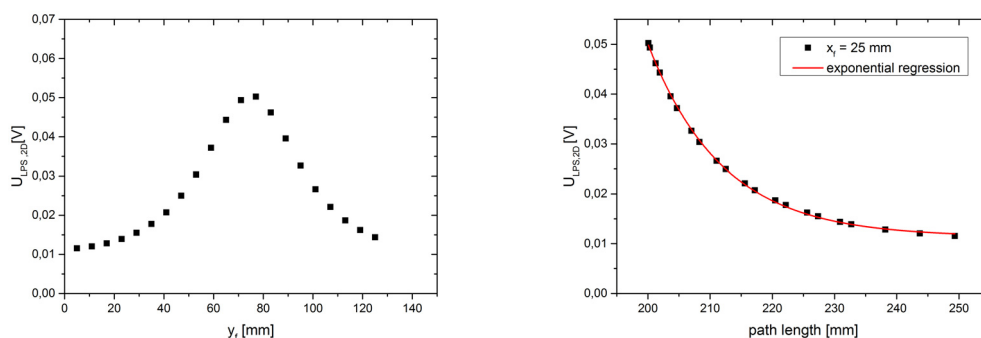


Fig. 3.17: Left panel: Vertical line scan of the simulated LPS-Voltage. Right panel: dependency of the two-dimensional simulated LPS-voltage depending on the path length, the shortest way connecting the focal points to both contacts.

We shortly introduce the path length as a value, which we define as the shortest path, connecting  $P_c$  via  $P_f$  to the area contact, which is located  $x_f = 200$  mm. Numerically this means:

$$\text{path length} = L - x_f + \sqrt{x_f^2 + (B/2 - y_f)^2} = 175 \text{ mm} + \sqrt{(25 \text{ mm})^2 + (75 \text{ mm} - y_f)^2} \quad (3.14)$$

Using this value, we get an exponential function connecting the  $U_{\text{LPS},2\text{D}}$  to the path length, which can be seen in Fig. 3.17 right panel. This means, that using a point-like contact adds also distortion to the measurement, which can easily be avoided.

### 3.3. Doping striations and model validation

We are now in a position, where we are able to describe the photovoltaic effect locally and we know, how this signal is transmuted to a voltmeter. So the next step is to connect both to verify the used models.

To validate our model, in this Section we compare the measured and simulated LPS data, obtained from sample S0 at different laser pump power. The n-type sample (sample S0,  $\rho = 20 \Omega\text{cm}$ ,  $N_D = 6.5 \times 10^{14} \text{cm}^{-3}$ ) was studied to demonstrate the effectiveness of the LPS approach for the characterization of crystal striation and to benchmark our numerical model. To this aim the charge carrier lifetime of S0 was measured using a commercial MDP-map system finding  $\tau_{S0} = 900 \mu\text{s}$ ; this value drops to  $240 \mu\text{s}$  when the surface is not passivated. Relying on this results we obtained a realistic estimation of material parameters governing the recombination velocity and the SRH rate in this sample.

In Fig. 3.18(a) we show the LPS signal, acquired from sample S0 with line scans along the  $x$ -direction, using four different laser pump powers. We find that at low laser power the main spatial wavelength component of the LPS signal of  $910 \mu\text{m}$  matches quite well with the spatial periodicity of dopant striation, expected for the adopted growth conditions; on the other hand, at larger pump power this spatial scale is not resolved [LR97], due to the lowering of the LPS resolution triggered by the increased fluency (see discussion in the next Section).

Moreover, to test the validity of our numerical model, we used the integrated experimental LPS signal shown in Fig. 3.18 left panel as an n-type doping profile to simulate the LPS voltage reported as red curve in Fig. 3.18 right panel, assuming uniform concentration along the  $y$ - and  $z$ - directions. As expected, the simulated LSP signal closely reproduces the spatial dependence of the input dopant gradient, since for an n-type material the photoinduced voltage is directly proportional (upper sign in Eq. (2.19)) to this quantity. Indeed, a spectral analysis of both the experimental and numerical signal reveals that the five main frequencies are correctly reproduced.

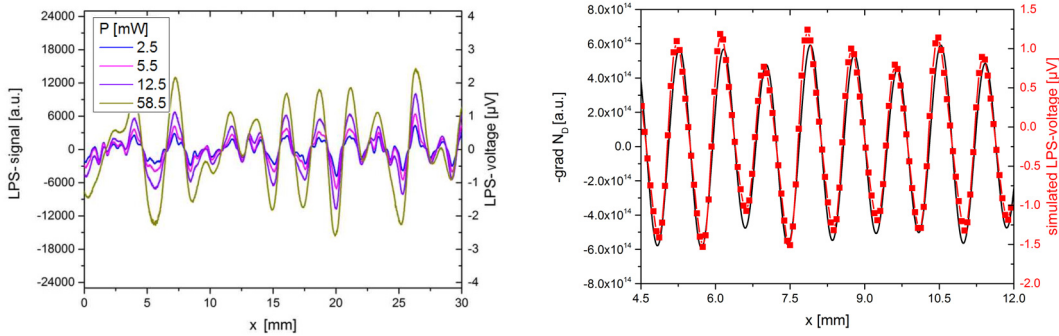


Fig. 3.18: Left panel:  $U_{LPS}$  line scan along the  $x$ -direction from sample S0 at different laser power, as reported in the legend. Right panel: simulated LPS voltage obtained from the dopant profile derived from the  $U_{LPS}$  signal shown in the left plot (red curve 5.5 mW). For comparison also the profile of the dopant gradient used in the simulation is reported (black curve).

We now analyze the dependence of the LPS voltage on the pump excitation density. For this purpose, in Fig. 3.19 we show for the n-type S0 sample at fixed excitation position the experimental (black squares) and simulated (red circles)  $U_{LPS}$  voltage as a function of the laser power close to the sample surface. Our numerical data are in very good agreement with measurements, and indicate a sublinear increasing behaviour. This trend can be interpreted considering that the photogenerated carriers tend to screen the driving force field associated to the dopant gradient. Therefore, upon increasing the laser power, the spatial displacement of the electron and hole excess carrier density, responsible for the photogenerated voltage, is controlled by a force whose intensity decreases due to the increased effectiveness of the screening effect, associated to larger excess carrier concentrations. This in turn results in a sublinear dependence of the LPS voltage from the laser power, despite the fact that our simulations indicate that the

excess carrier density is linearly proportional to the pump fluency. This would be in line with a dominant SRH-recombination.

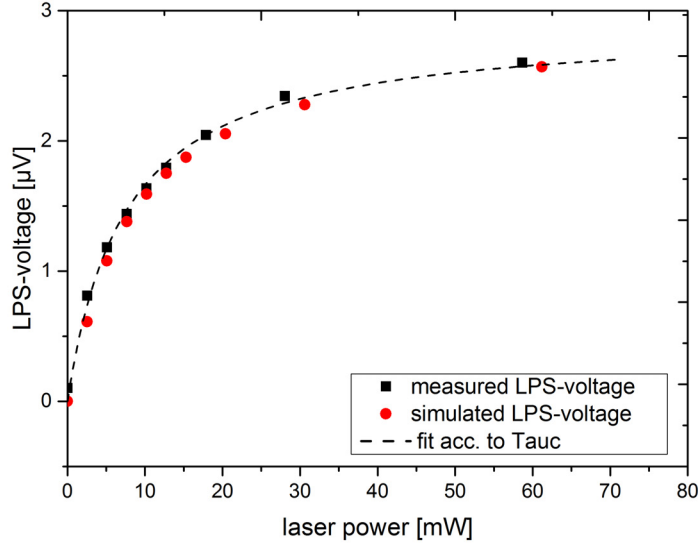


Fig. 3.19: Measured and simulated LPS voltages at fixed  $(x_f, y_f)$  as a function of laser pump power for the unimplanted n-type sample.

### 3.4. Conclusion

In this section we have looked at the signal transmission between a generated photovoltage inside of a Si sample and the measured voltage difference at the inner resistance of a voltmeter. For a rectangular sample with area contacts a linear transmission function could be analysed. The transmission coefficient  $c_1$  depends on sample geometry factors. So far a low transition coefficient limits the measurability of the sample.

For sample geometries such as a circle or a trapezoid the transition function becomes non-linear and this leads to distorted measurements. These have to be corrected for an analysis of the strength of the photovoltaic effect. Even by an integration to get the resistivity shape, this distortion has to be corrected.

In addition we investigated the influence of the contact (point-like or area). Here a point-like contact adds also a distortion to the measurement, which can be avoided by using area contacts.

In conclusion, the good agreement between numerical data and experimental observations described in this section validates our numerical model, and indicates that the integrated LPS signal is proportional to the local value of the dopant gradient. Indeed, the proportionality between the  $U_{LPS}$  and the dopant gradient, first predicted with simplifying assumptions by Tauc (see Fig. 3.19), has been confirmed here relying on a numerical model which takes into account in-plane and out-of-plane carrier diffusion, a mandatory prerequisite to describe realistic 3D sample geometries. Moreover, our model correctly addresses the spatial profile of the excess carrier distribution, which in our experimental conditions is much wider than the laser spot size, in contrast to the opposite working hypothesis assumed in the original analysis by Tauc. [Tau55]



# Chapter 4

## Local Resolution of the LPS Measurements

At this stage it is worth to notice that the spatial resolution of the LPS measurement is usually limited by the diffusive motion of the photogenerated carriers rather than by the spot size. Indeed in Si the diffusion length can be as large as few millimeters i.e. much more than the typical optical beam diameter. The introduction of a convolution function for the LPS signal is the most straightforward approach to phenomenologically model this smearing effect. In other words we assume that the LPS-voltage can be written as

$$U_{\text{LPS}}(x_f, y_f) \propto (\nabla_x N_{A,D} * \gamma)(x_f, y_f), \quad (4.1)$$

where  $N_{A,D}$  is the spatially dependent acceptor/donor concentration and  $\gamma$  represents an appropriate convolution profile centered in  $(x_f, y_f)$ , whose spatial extension controls the resolution of the LPS measurement. Notice also that in writing the above equation we have implicitly assumed that the photovoltage associated to the  $y$ -component of the dopant concentration gradient is not detected. As a consequence, integrating along the  $x$ -direction we obtain:

$$\int_0^x U_{\text{LPS}}(x_f, y_f) dx_f \propto (N_{A,D} * \gamma)(x, y). \quad (4.2)$$

The main scope of the present chapter is the quantitative estimation of the LPS spatial resolution, which can be assumed equal to the width of the convolution profile  $\gamma$ , as a function of the material parameters affecting the excess electron/hole distribution.

### 4.1. Sample preparation and SIMS characterization

In this Section we present samples, used for our analysis (see Table 4.1). A set of three boron implanted FZ wafers (S1-S3) have been fabricated and measured to estimate the LPS spatial resolution.

To explore the spatial resolution of the LPS method we prepared three p-type samples featuring a spatial variation of the resistivity, starting from homogeneous commercial 4" FZ Si wafers, with resistivity in the  $7 \Omega\text{cm} - 5000 \Omega\text{cm}$  range, associated to a acceptor concentrations  $N_{A,1}$  (see Table 4.1). To this aim on the top surface we have defined by B implantation a resistivity matrix using a lithographic mask to irradiate stripe-like regions only, which are oriented along the  $y$ -direction and with transverse dimension in the  $2.5 \mu\text{m} - 600 \mu\text{m}$  range. Spatial inter-stripe distances were chosen in the  $100 \mu\text{m} - 400 \mu\text{m}$  interval. The achieved B concentrations in the implanted regions  $N_{A,2}$  are listed in Table 4.1.

No.	$\rho_1$ [ $\Omega\text{cm}$ ]	$N_{A/D,1}$ [ $\text{cm}^{-3}$ ]	$N_{A,2}$ [ $\text{cm}^{-3}$ ]	$\rho_2$ [ $\Omega\text{cm}$ ]
S1	7	$1.9 \times 10^{15}$ B	$5.7 \times 10^{15}$ B	2.4
S2	200	$6.5 \times 10^{13}$ B	$3.8 \times 10^{15}$ B	3.5
S3	5000	$2.5 \times 10^{12}$ B	$3.8 \times 10^{15}$ B	3.5

Table 4.1: Sample characteristics: background ( $N_{A/D,1}$ ) and implanted ( $N_{A,2}$ ) dopant concentration, corresponding to resistivity  $\rho_1$  and  $\rho_2$ , respectively, obtained with a 2D B dose of  $1 \times 10^{11} \text{ cm}^{-2}$ .

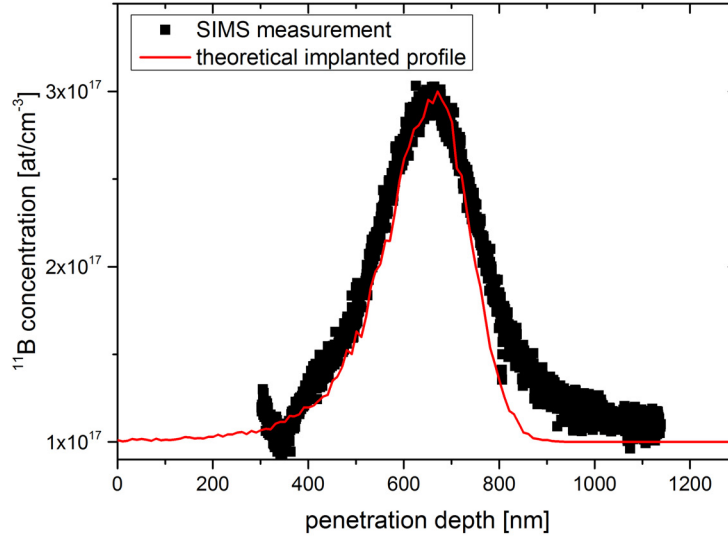


Fig. 4.1: SIMS measurement of the  $^{11}\text{B}$ -concentration in the implanted region after RTA for sample with  $N_{A,2} = 1 \times 10^{17} \text{ cm}^{-3}$ , compared with the theoretical estimation discussed in the text (red curve). Notice that the model properly describes the asymmetry of the measured profile.

SIMS data were also used to estimate the B concentration profile along the  $z$ -direction as shown in Fig. 4.1. For measurement reasons we had to use a comparison sample with  $N_{A,1} = 1 \times 10^{17} \text{ cm}^{-3}$  keeping the same  $N_{A,1}$ - $N_{A,2}$  ratio as sample S3. For comparison in Fig. 4.1 we also plot the expected distribution, where diffusion effects, associated to the annealing treatment were not taken into account. This result allow us to conclude that the RTA does not significantly contribute to the spatial extension of the concentration profile along the  $z$ -direction, which is typically in the order of 100 nm, in line with data reported for similar samples by Cho et al. [CNF<sup>+</sup>85].

Since the sharpness of the implanted/not-implanted interface at the stripe boundary can be responsible for larger diffusion effects of the B atoms during the RTA treatment, we performed dynamic SIMS measurements to evaluate the in-plane concentration profile, as shown in Fig. 4.2 for a sample with nominal stripe width of  $90 \mu\text{m}$ . In the inset of Fig. 4.2 also a line scan along the  $x$ -direction is reported. Those results confirm the presence of doped stripe regions, featuring a constant plateau, separated by the non-implanted regions by sharp interfaces, whose characteristic length is in the order of  $30 \mu\text{m}$ . This number is approximately equal to the in-plane SIMS spatial resolution, which is limited by the diameter of the probe beam (about  $24 \mu\text{m}$ ). This fact does not allow us to assess the impact of the RTA on the in-plane diffusion. Nevertheless, we notice that, as demonstrated in the following, the  $30 \mu\text{m}$  scale is one order of magnitude



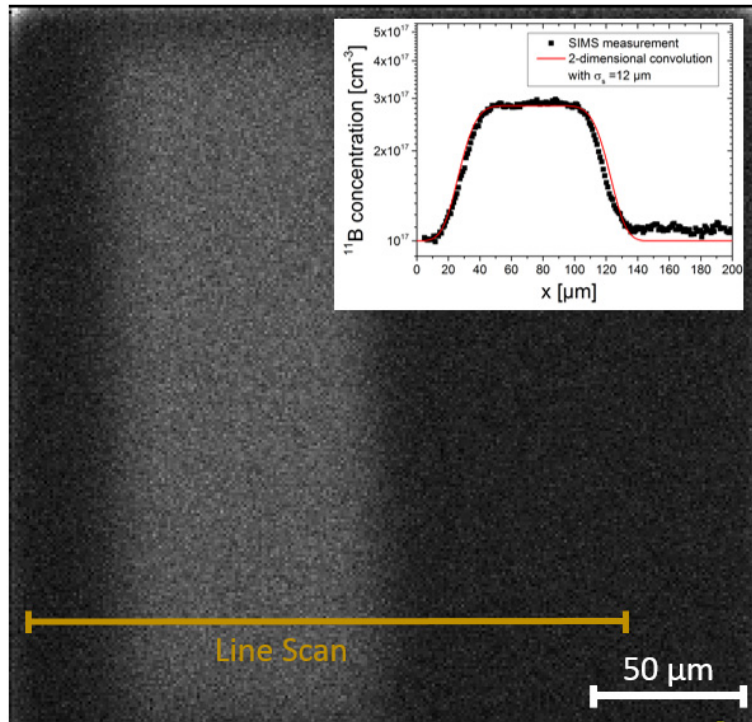


Fig. 4.2: SIMS map of the in-plane doping profile acquired after RTA with a penetration depth of 650 nm i.e. at the peak of the  $z$ -distribution of dopants, from a sample with nominal stripe width of 90  $\mu\text{m}$ . In the inset a line scan along the transverse  $x$ -direction is also shown together with a rectangular profile convolved with Gaussian functions with  $\sigma = 12 \mu\text{m}$  (red curve).

lower than the standard deviation of the LPS convolution function of Eq. (4.2). For this reason, in our simulation we have taken into account the proper spatial distribution of dopants in the vertical plane, but in-plane diffusion effects have been neglected.

An LPS grey scale map is reported in Fig. 4.3 for the example of sample S1 where the implanted matrix, superimposed to the typical doping striation pattern is clearly distinguishable.

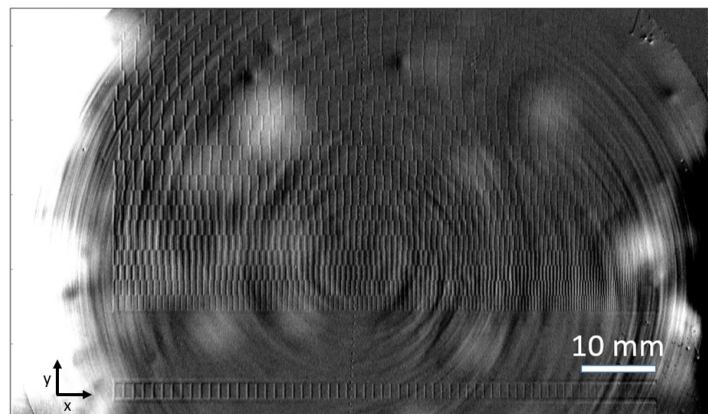


Fig. 4.3: LPS grey-scale map acquired from sample S1. Darker (brighter) grey corresponds to negative (positive)  $x$ -component of the gradient of the dopant concentration.

A convincing measurement of the LPS resolution requires steps in the doping profile along the  $x$ -direction of our samples, characterized by a spatial scale smaller with respect to the typical width of the convolution function  $\gamma$  reported in Eq. (4.2).

Symbol	Explanation	Value	
$\lambda$	wave length of the laser	685 nm	
$P$	maximum power of the laser	20 mW	
$A_C$	absorption coefficient in Si	$1/4.7 \mu\text{m}^{-1}$	[PS72]
$\mathcal{R}$	reflection coefficient for Si	0.34	
$\sigma$	standard deviation of the Gaussian laser spot	$1.25 \mu\text{m}$	
$C_{\text{Rad}}$	coefficient for radiative recombination	$1 \times 10^{-14} \text{cm}^3/\text{s}$	[GSM72]
$E_t$	trap level of B impurities	0.044 eV	[SK69]
$\tau_n$	SRH lifetime for electrons	400 ns	
$\tau_p$	SRH lifetime for holes	400 ns	
$\tau_{\text{S1,S2,S3}}$	measured life time for sample S1, S2 and S3	$0.3 \mu\text{s} - 1.8 \mu\text{s}$	
$C_{\text{Au}}^n$	Auger recombination coefficient for electrons	$2.8 \times 10^{-31} \text{cm}^6/\text{s}$	[DS77]
$C_{\text{Au}}^p$	Auger recombination coefficient for holes	$9.9 \times 10^{-32} \text{cm}^6/\text{s}$	[DS77]
$S_{\text{eff}}$	eff. surface recombination coefficient	$300000 \text{cm}/\text{s}$	
$F_1$	Coefficient for Fletcher mobility model	$1.04 \times 10^{21} 1/\text{cmVs}$	[DL81]
$F_2$	Coefficient for Fletcher mobility model	$7.45 \times 10^{12} \text{cm}^{-2}$	[DL81]

Table 4.2: Table of simulation parameters

## 4.2. Spatial resolution of the LPS measurements

After having validated our simulation platform, in the former chapter we combine experimental and numerical data obtained from the B implanted FZ-wafers (S1-S3) to investigate the LPS spatial resolution. To this aim no free tune-able parameters have been introduced in our modelling since input data used to describe the laser characteristic, the dopant profile, the SRH trap level and lifetime, and the surface recombination velocity, are taken from the literature or directly measured (see Table 4.2).

To give an intuitive picture of the spatial resolution achieved in our LPS experiments with B implanted Si samples, we show in Fig. 4.4 a scan along the  $x$ -direction of the  $U_{\text{LPS}}$  signal acquired from S2 before (black curve) and after (red curve) spatial integration.

The superimposed B profile (blue dashed curve), that at this spatial scale is practically a rectangular function, indicates that the LPS measurement properly assess the stripe positions and evidences its spatial resolution (notice that in agreement with Eq. (2.1) for the case of p-type materials, spatial regions featuring a positive dopant gradient are associated with positive values of the photogenerated voltage).

For a quantitative estimation of the LPS resolution, in line with Eq. (4.2), we have compared the peak line shape of the integrated LPS signal with doping profiles  $\bar{N}(x)$ , obtained by convolution along the  $x$ -direction of the rectangular function with Gaussian distributions, featuring different standard deviations. By a regression of these convolved doping profiles to the integrated LPS signal, we obtain from the best fitting profile, our estimation of the LPS resolution, defined in terms of the associated standard deviation  $\sigma_s$  (see Supplementary Material for details on the fitting procedure). As an example we show in Fig. 4.5 the LPS signal from S2 at  $P = 2.4 \text{mW}$  which can be quite faithfully reproduced by our best fitting profile obtained for  $\sigma_s = 200 \mu\text{m}$ .

We underline that the LPS resolution is related to the spatial extension of the photogenerated carrier distribution, which in S1-S3, using a spot size of about  $\sigma_L = 1.25 \mu\text{m}$  at the adopted pump fluency, is estimated to be of the order of  $10 \mu\text{m}$ . In other words, the LPS resolution

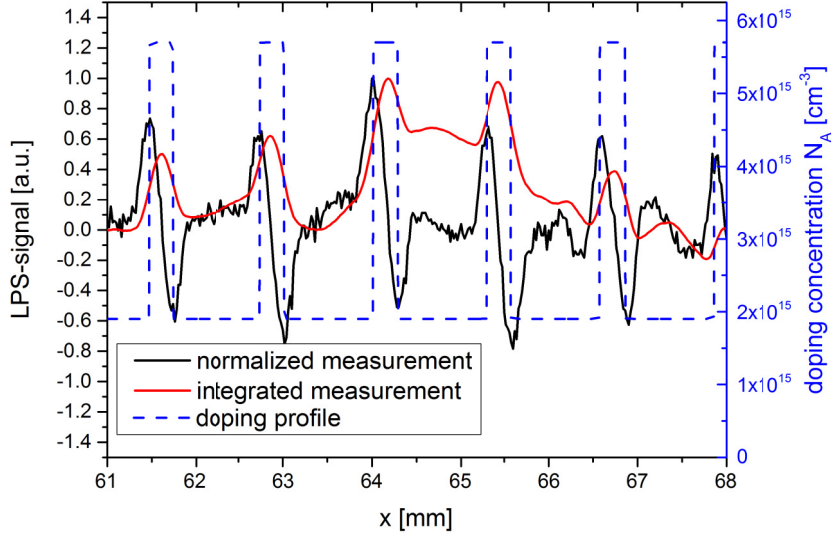


Fig. 4.4: LPS (black curve) and integrated (red curve) LPS signal from S2 measured at  $P = 20\text{mW}$ . The blue dashed curve refers to the right vertical axis and represents the doping profile. The large period modulation of the LPS signal and its inter-stripe secondary peaks are to be attributed to the contribution stemming from background doping striation.

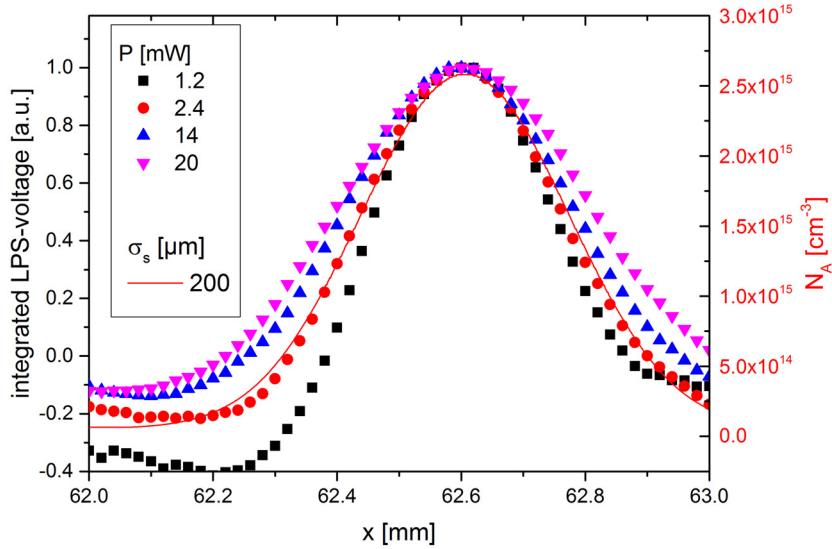


Fig. 4.5: Integrated LPS signal measured in S2 at different laser powers  $P$  (symbols). The solid red curve represents the dopant profile, convolved with a Gaussian function whose standard deviation  $\sigma_s$  is used as a fitting parameter to estimate the LPS spatial resolution at  $P = 2.4\text{mW}$ .

depends both on the material parameters governing the spatial extension of the carrier dynamics, and on the peculiar experimental conditions adopted to optically excite the sample. In general however, LPS spatial resolution is also influenced by the intensity of the driving force field, associated to the sample inhomogeneities which, controlling the spatial separation of the excess electron and holes distributions, governs the signal intensity associated to the bulk

photovoltaic effect. It follows that the LPS resolution may be found at a scale length different from the one describing the excess carrier diffusion length in an homogeneous portion of the sample (up to several mms in pure Si). These considerations motivate our operative procedure for the assessment of the LPS resolution in terms of the best fitting convolved doping profile. To this aim, we notice that the fact, that the reconstructed doping profile is well described by a Gaussian smoothing, is not in conflict with the non-Gaussian character of the photogenerated carrier distribution. Indeed in our simulations we observe for the excess electrons and hole concentration a strong deviation from the Gaussian shape, as one can expect considering that the material is not isotropic and that in our simulations we include non-linear recombination terms.[Gie14]

In line with the above considerations, our numerical simulations indicate that the in-plane spatial distribution of the electron/hole excess carriers may not only depend on the laser spot intensity but also on the spot position. As a matter of fact, when calculated for  $x_f$  located at the stripe boundary, the excess carrier distributions are characterized by a strong asymmetry. In Fig. 4.6 top left panel, we report the excess electron and hole distribution for sample S2 at different laser powers, estimated setting the laser spot at the left interface of the implanted stripe, i.e. in a region featuring a strong positive dopant gradient. In this case the standard deviation of the excess carrier distribution is typically one order magnitude larger than of the laser spot size, i.e. far from the LPS resolution that is about two orders of magnitude larger. Moreover, the LPS resolution is found to be a decreasing function of  $P$ , ranging between  $\sigma_s = 95 \mu\text{m} - 165 \mu\text{m}$ , while the standard deviation for the excess electron and hole distribution is only weakly affected by  $P$ .

In order to see the bulk photovoltaic effect at “work”, we plot in Fig. 4.6 top right panel the net  $\rho = p - n$  photoinduced charge density for  $P = 2.5 \times 10^{-3} \text{ mW} - 2.5 \text{ mW}$ , together with the static donor concentration profile  $N_A$ . The associated equilibrium conduction and valence band edge profiles are shown in Fig. 4.6 bottom left panel and evidence the screening character of the photoinduced electric field, shown in Fig. 4.6 bottom right panel. In line with Eq. (2.1) and with the sign of the photoinduced electric field shown in Fig. 4.6 bottom right panel, we obtain a positive value for the LPS voltage (see Fig. 4.4 at  $x = 64 \text{ mm}$ ).

Before comparing simulated and experimental data for the LPS resolution, we numerically investigate the impact of the doping profile along the out-of plane direction  $z$  on  $\sigma_s$ . To this aim we compare results obtained using  $z$ -dependent and  $z$ -independent dopant concentrations. Integrated LPS voltages reported in Fig. 4.7 left and central panel have been evaluated both accounting for the  $z$ -dependence in the B concentration as measured by SIMS experiments and considering only the dopant variation occurring along the  $x$ -direction, i.e. assuming an homogeneous dopant concentration along the  $z$ -axis throughout the whole wafer thickness central panel. In the latter case the dopant profile along the  $x$ -direction is set equal to the one measured by SIMS at the  $z$ -value where the dopant concentration peaks. To benchmark the measured LPS resolution with our theoretical prediction, we have applied the same procedure for the evaluation of the standard deviation of the convolved doping profile, which has been obtained fitting numerical LPS data. In Fig. 4.7 left and center panel we show the simulated integrated  $U_{\text{LPS}}$  signal and the rectangular doping profile along the  $x$ -direction for different laser powers. Also for numerical data the integrated signals are well described by a doping profile convolved with appropriate Gaussian functions (dashed curves in Fig. 4.7 left and central panel).

Indeed, this  $z$ -homogeneous configuration properly describes doping fluctuations associated to striations, since their spatial scale along the  $z$ -direction is usually much larger with respect to

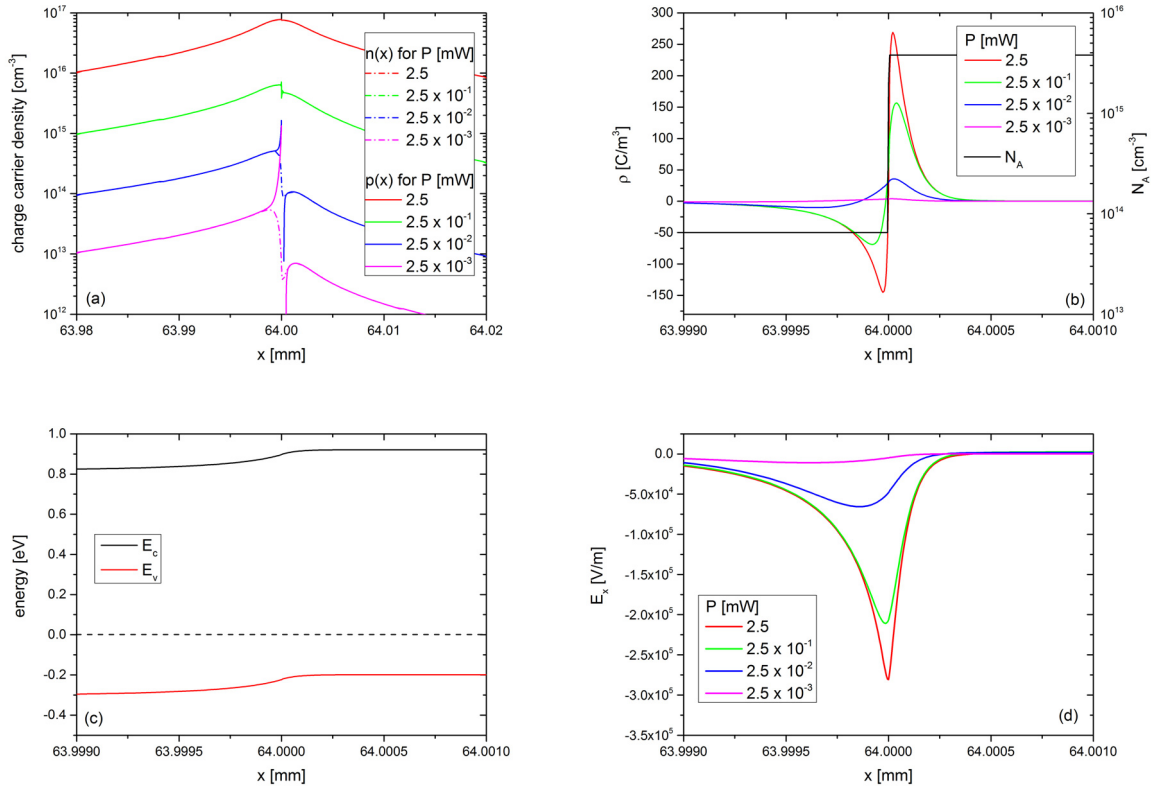


Fig. 4.6: Top left panel: numeric excess electron and hole carrier distribution, simulated at different pump powers for sample S2 with laser spot at the left interface of an implanted region ( $x = 64$  mm) i.e. in a region featuring a positive dopant gradient. The distributions are plotted as a function of  $x$  at the sample surface along a line passing through the laser spot center. Top right panel: the corresponding distribution for the net excess charge density  $\rho = p - n$  are shown for  $P = 2.5 \times 10^{-3}$  mW - 2.5 mW (left vertical axis) together with the static acceptor density  $N_A$  (black curve, right vertical axis). Bottom left panel: valence (red curve) and conduction (black curve) band edge at equilibrium. Bottom right panel: the photoinduced screening field, calculated as a function of  $x$  is shown.

both the laser penetration depth and the photocarrier diffusion along the out-of-plane axis. In the  $z$ -homogeneous case we obtain a  $U_{LPS}$  signal increased by a factor of about 110 for  $P = 20$  mW, which considers that the extension of the excess carrier distribution in the  $z$ -direction is larger than the laser penetration depth  $4.7 \mu\text{m}$  and so broader than the thickness of the doped region of about  $400$  nm. For this reason, when assuming a uniform dopant distribution along the  $z$ -direction, a larger portion of the sample contributes to the  $U_{LPS}$  signal.

Nevertheless, from the comparison of normalized  $U_{LPS}$  data reported in Fig. 4.7 left and central panel, we find that the shape of the  $U_{LPS}$  signal and then its in-plane resolution, is practically unchanged whether a  $z$ -dependent (Fig. 4.7 left panel) or a  $z$ -independent dopant profile (Fig. 4.7 central panel) is adopted.

This is apparent also from Fig. 4.7 right panel where  $\sigma_s$  is plotted as a function of the laser power. In the two cases: the spatial resolution in  $x$ -direction features very similar increasing behaviour. The slightly smaller value of  $\sigma_s$  obtained for the  $z$ -homogeneous configuration is to be attributed to the lower excitation density achieved in this material due to the increased non-radiative recombination rate associated to the larger amount of dopants.

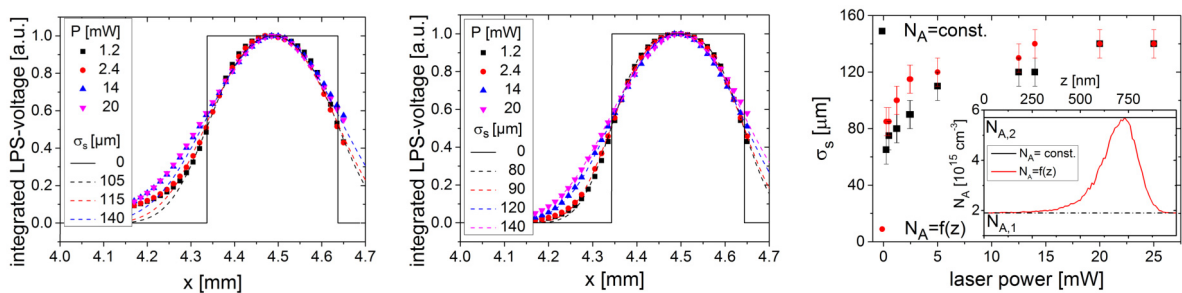


Fig. 4.7: Left and central panel: numerical simulation for sample S1 of line scans along the  $x$ -direction of the integrated LPS voltage, calculated at different laser powers. Plot (left panel) and (central panel) have been obtained considering and neglecting variations in the dopant concentration profile occurring along the  $z$ -direction, respectively (see text). For each pump power, the dashed line represents the best fitting convolution of the in-plane dopant distribution (black solid line) with a Gaussian function whose standard deviation  $\sigma_s$  is reported in the legend. Right panel: standard deviation for the best fitting Gaussian convolution profile as a function of the pump power, obtained with a  $z$ -dependent doping profile (red circles) and with an homogeneous doping profile along the  $z$ -direction (black square). The inset displays the  $z$ -dependence of the dopant concentration used in the simulations.

In conclusion, the LPS spatial resolution in the  $x$ -direction is not very sensitive to variations of the doping profile in the  $z$ -direction. Indeed, in our experimental condition, this last quantity controls only the magnitude of the LPS signal. It also follows that the precise shape of the doping profile along the  $z$ -direction does not represent a critical variable, which may limit the validity of a comparison between numerical and experimental LPS data.

For the investigated S1-S3 samples the measured and simulated LPS resolutions as a function of the laser pump power in the  $2.5 \times 10^{-2}$  mW - 25 mW range, are reported in Fig. 4.8. We find  $\sigma_s$  in the  $85 \mu\text{m}$  -  $350 \mu\text{m}$  interval with an overall satisfactory quantitative agreement between experimental and numerical values. Also the measured qualitative trends shown in Fig. 4.8 are correctly reproduced by the model.

As mentioned before, the  $\sigma_s \geq 85 \mu\text{m}$  spatial scale results to be much larger with respect to both the laser spot size ( $\sigma_L = 1.25 \mu\text{m}$ ) and the in-plane width of the excess carrier distribution ( $\approx 10 \mu\text{m}$ ). We notice also that the LPS resolution improves in samples featuring greater doping concentrations. Indeed  $\sigma_s$  in the S3 sample, which features a dopant concentration in the unimplanted region of  $N_{A,1} = 2.5 \times 10^{12} \text{cm}^{-3}$ , spans the  $190 \mu\text{m}$  -  $350 \mu\text{m}$  interval, while in the S1 sample, where the dopant concentration is  $N_{A,1} = 1.9 \times 10^{15} \text{cm}^{-3}$ ,  $\sigma_s$  remains below 150 micron.

This fact can be explained in terms of an increase of the driving force, caused by larger dopant gradients, rather than being attributed to lower electron and hole mobilities, or faster non-radiative recombination rates, which at larger doping densities may limit the spatial extension of the photogenerated carrier distribution. On the other hand, the moderate increase of  $\sigma_s$  with  $P$  is happening because larger pump powers are associated to greater spatial widths of the excess carriers.

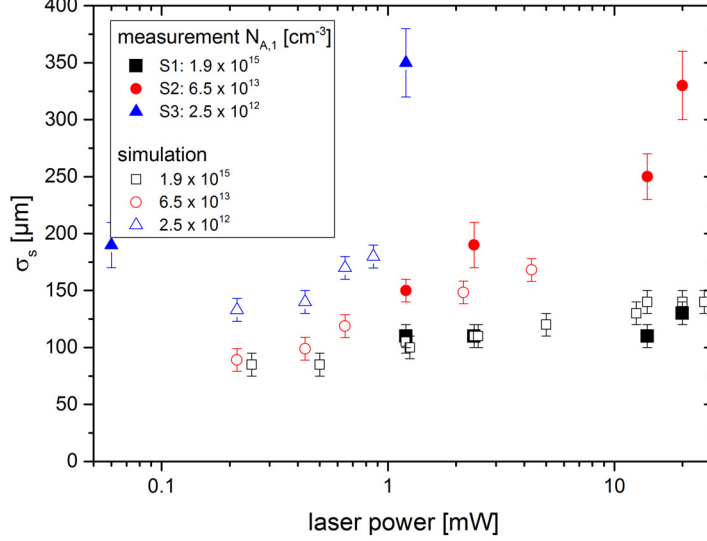


Fig. 4.8: Measured (full symbols) and simulated (empty symbols) LPS resolution  $\sigma_s$  as a function of pump power  $P$  for S1 (black squares), S2 (red circles), and S3 (blue triangle).

### 4.3. Conclusion

Our results are in agreement with data reported by Lüdge et al. [LR97], which, by means of LPS experiments with high pure FZ wafer, showed that the LPS resolution can be up to two orders of magnitude higher than the laser spot profile (i.e. in the same range as here obtained). Moreover, as empirically found also by Lüdge et al., we obtain that the spatial resolution can be improved by lowering the pump power. Of course one has to take in mind that the lowest pump power suitable for practical applications is limited by the signal to noise level.

As a final remark we briefly comment on the relatively large discrepancy between numerical and experimental data observed for S3 (blue symbols) in Fig. 4.8. This discrepancy can be attributed to the fact that, at the adopted pump power the carrier concentration generated in S3 (of the order of  $10^{15} \text{ cm}^{-3}$ ) is much larger than the background and implanted one. For this reason, the driving force associated to the dopant gradient in S3 can be regarded as extremely small and therefore unavoidable parameter uncertainties have in this case a larger impact on the estimation of  $\sigma_s$ . Similar considerations explain why for the S3 and S2 samples we could not simulate the LPS resolution in the high laser power region. In fact, due to the relative weakness of the driving field, associated to the lower dopant concentration featured by these samples, the CPU time required for convergency in the high excitation density regime becomes unaffordably long.





# Chapter 5

## Strain-field Measurement Simulation

In the last two decades, strain engineering in semiconductors has emerged as a very powerful approach in the control of mechanisms that are routinely applied to both electronics and photonics. As an example, the in-plane electron or hole mobility of Si is significantly increased when uniaxial or biaxial stress is applied, enhancing the performance of the modern transistors based on CMOS (Complementary Metal Oxide Semiconductor) technology [BBC<sup>+</sup>13]. In addition, breaking the centro-symmetry of the crystal lattice of Si may induce a second-order optical susceptibility, offering an open space for second-order non-linear processes (e.g. second harmonic generation) and improvement in terms of electro-optic modulation in the direction of high speed and low absorption loss. Strain engineering is also trying to change the paradigm of integrated light emitters that are now mainly based on III-V materials. In this direction, Ge has been selected as a promising material for integrating laser light source. This happens exploiting its nature of quasi-direct band gap material in combination with tensile strain that decrease the energy difference between the fundamental and direct gap.

Several established techniques exist to measure the strain/stress in a semiconductor sample, such as Raman and defect induced stress imaging by Scanning Infrared Stress Explorer (SIREX). Raman measurements have a high sample preparation effort and can difficultly provide information about strain gradients. SIREX technology has still a high vertical resolution of 3  $\mu\text{m}$ , but integrates the signal over the whole sample thickness. [HWK<sup>+</sup>18]. This is rather inefficient for most sample geometries, where a stressor-layer induces the stress mainly close to the sample surface.

As formerly stated, Tauc [Tau55] predicted that the bulk photovoltaic effect might be used to detect any effect that introduces spatial inhomogeneities in the band edges of semiconductors. In this chapter, we investigate the potentiality of **Lateral-Photovoltage-Scanning** method (LPS) for detection of the presence of strain gradients, exploiting the associated variation in the conduction  $E_c$  and valence band  $E_v$  edge. To this aim, we simulated the three-dimensional strain profile a Si nitride ( $\text{Si}_3\text{N}_4$ ) stressor causes, when it is deposit on-top of a Si sample. Afterwards, using the deformation potential theory, we calculate the band edge profile of the Si sample, which is the starting point for the LPS simulation.

From computational point of view with suitable assumptions for a stripe-like stressor layer, we achieved to directly couple the solid mechanics module and the semiconductor module in COMSOL Multiphysics [Com13] without any further data transmission and/or storage, which allows a great flexibility in sample and mesh designing.

## 5.1. Theoretical Model

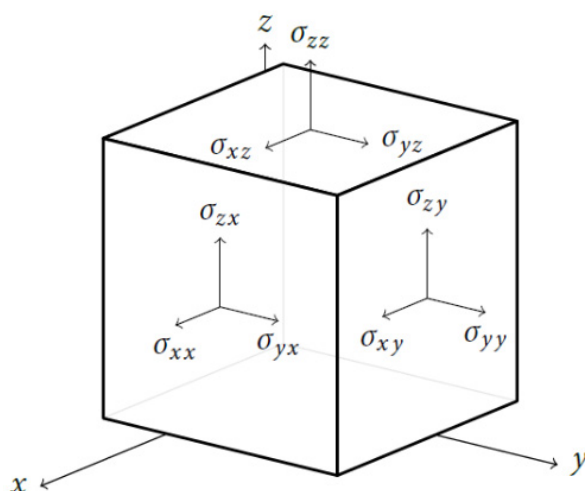


Fig. 5.1: Scheme of the strain tensor notation system chosen for the further investigations

### 5.1.1. Strain simulation model

Si is the most widely used material for electronics and microelectro-mechanical systems (MEMS) applications. For those reasons, several efforts have been done to investigate and to measure accurately its mechanical properties. Elastic features such as the elastic modulus, the shear modulus and the Young's modulus, depend on the crystalline structure. Consequently, the wafer orientation has a strong effect on the micro-fabrication and a wrong estimation of those characteristics can significantly influence the result of the device performance. In our investigation, we focus on Si-on-insulator (SOI) wafer (100) oriented, which means that the top surface of the wafer is perpendicular to the [100] Si crystal axis. To better describe the mechanical deformation in Si, let us start from stress-strain relations. Stress rise from density force applied per unit area on the crystal

$$\sigma = \begin{pmatrix} \sigma_{xx} & \sigma_{xy} & \sigma_{xz} \\ \sigma_{yx} & \sigma_{yy} & \sigma_{yz} \\ \sigma_{zx} & \sigma_{zy} & \sigma_{zz} \end{pmatrix}. \quad (5.1)$$

The strain is modeled as a two indexed tensor in the equation shown above. The first index defines the direction of the applied force, while the second refers to the normal to the plane where the force is applied (see Fig. 5.1). In the linear regime, we can assume the Hooke's law and the relationship between the stress ( $\sigma_{ij}$ ) and the strain ( $\epsilon_{kl}$ ) assumes the following form

$$\sigma_{ij} = C_{ijkl} \epsilon_{kl} \quad (5.2)$$

where  $C_{ijkl}$  is the stiffness matrix and where both the stress ( $\sigma_{ij}$ ) and the strain ( $\epsilon_{kl}$ ) have only six independent components as a direct consequence of the Hooke's law. In the case of Silicon, a more convenient description, that avoids tensorial transformation, is the one that makes use of the orthotropic model. A material is said to be orthotropic when it has least two orthogonal planes of symmetry and its elasticity can be described by a matrix that takes into account the

fundamental elasticity quantities in the axes of interest: the Young's modulus ( $Y$ ), the Poisson's ratio ( $\hat{I}_2^1$ ) and the shear modulus ( $G$ ). For this, the stress/strain relation reduces to:

$$\begin{pmatrix} \sigma_{xx} \\ \sigma_{yy} \\ \sigma_{zz} \\ \sigma_{yz} \\ \sigma_{zx} \\ \sigma_{xy} \end{pmatrix} = \begin{pmatrix} \frac{1-v_{yz}v_{zy}}{Y_x Y_z \Delta} & \frac{v_{yx}+v_{yz}v_{zy}}{Y_y Y_z \Delta} & \frac{v_{zx}+v_{yx}v_{zy}}{Y_z Y_x \Delta} & 0 & 0 & 0 \\ \frac{v_{xy}+v_{xz}v_{zy}}{Y_x Y_z \Delta} & \frac{1-v_{zx}v_{xz}}{Y_x Y_z \Delta} & \frac{v_{zy}+v_{zx}v_{xy}}{Y_z Y_x \Delta} & 0 & 0 & 0 \\ \frac{v_{xz}+v_{xy}v_{yz}}{Y_x Y_z \Delta} & \frac{v_{yz}+v_{xz}v_{yx}}{Y_x Y_z \Delta} & \frac{1-v_{xy}v_{yz}}{Y_x Y_z \Delta} & 0 & 0 & 0 \\ 0 & 0 & 0 & G_{yz} & 0 & 0 \\ 0 & 0 & 0 & 0 & G_{zx} & 0 \\ 0 & 0 & 0 & 0 & 0 & G_{xy} \end{pmatrix} \cdot \begin{pmatrix} \epsilon_{xx} \\ \epsilon_{yy} \\ \epsilon_{zz} \\ \epsilon_{yz} \\ \epsilon_{zx} \\ \epsilon_{xy} \end{pmatrix}. \quad (5.3)$$

Here

$$\Delta = \frac{1 - v_{xy}v_{yx} - v_{yz}v_{zy} - v_{zx}v_{xz} - 2v_{xy}v_{yz}v_{xz}}{Y_x Y_y Y_z} \quad (5.4)$$

is used. The elastic constant of Si in case of crystal coordinate axis at [100], [010], and [001] are:

$$Y_x = Y_y = Y_z = 130 \text{ GPa} \quad (5.5)$$

$$v_{yz} = v_{zx} = v_{xy} = 0.28 \quad (5.6)$$

$$G_{yz} = G_{zx} = G_{xy} = 79.6 \text{ GPa}. \quad (5.7)$$

We selected the letter "Y" for the Young's module instead of the more common "E" to avoid misinterpretations with the symbol for the electric field. The deformation of the Si stripes has been computed using COMSOL Multi-Physics tool. Assuming a compressive in-plane initial pressure of 4 GPa on the Si nitride cladding (defined as an amorphous material featuring an internal stress, which will then be transferred to the under-laying Si) the elastic strain has been computed on the Si stripes under the orthotropic approximation.[Hop07, MPB15]

The mechanical deformation calculations on the stripe show that the components  $\epsilon_{xy}$  and  $\epsilon_{yz}$  identically vanish and  $\epsilon_{yy}$  is presenting a negligible contribution with respect to  $\epsilon_{xx}$ ,  $\epsilon_{zz}$  and  $\epsilon_{xz}$  and the strain profile will be described in detail in the following sections.

### 5.1.2. Deformation potential theory

The description of the band alignment in the model is based on the deformation potential theory and the "model-solid approach". The predictions in terms of lattice mismatch and pseudomorphic strained layer interfaces. This predicts the band offsets at both lattice-matched and pseudomorphic strained-layer interfaces. In this section, we will show the behavior of valence and conduction bands under the effect of strain.

**Conduction Band** As a general remark, direct conduction bands (at  $\Gamma$ ) are non-degenerate and therefore only subject to hydrostatic strain shifts. In indirect semiconductors, however, the strain induced shift and splitting of fundamental conduction-band minima needs to be analyzed case by case. As an example, in Si the minima occur close to the X point (along the (001)-direction), in Germanium at the L point ((111)-direction). Because there are six equivalent (001)-directions, and eight (111) directions, the conduction-band valleys are degenerated in the cubic configuration, but can be split by the application of strain in appropriate directions.

The general formulation by van de Walle [Van86] is  $E_c^i = E_{c,0} + \Delta E_c^i$  where  $E_c^i$  is the  $i$ -th conduction band (according to the unit cell vector direction  $i$ ),  $E_{c,0}$  is the unstrained band minimum and  $\Delta E_c^i$  is the strain dependent correction of the  $i$ -th conduction band given by:

$$\Delta E_c^i = [\Xi_d \mathbf{1} + \Xi_u \{a_i a_i\}] : \boldsymbol{\varepsilon}. \quad (5.8)$$

Here  $\Xi_d$  and  $\Xi_u$  are deformation potentials, whose values for Si are reported in Table 5.1,  $\mathbf{1}$  and  $\boldsymbol{\varepsilon}$  are tensors (unit tensor and strain tensor ( $\boldsymbol{\varepsilon}_{i,j}$  with  $i,j \in x,y,z$ ), respectively), whereas  $a_i$  is the unit cell vector in the  $i$ -direction and  $\{\}$  denotes the dyadic product

$$\{a_i a_i\} = \begin{cases} \begin{pmatrix} 1 & 0 & 0 \\ 0 & 0 & 0 \\ 0 & 0 & 0 \end{pmatrix} & \text{in [100]-direction} \\ \begin{pmatrix} 0 & 0 & 0 \\ 0 & 1 & 0 \\ 0 & 0 & 0 \end{pmatrix} & \text{in [010]-direction} \\ \begin{pmatrix} 0 & 0 & 0 \\ 0 & 0 & 0 \\ 0 & 0 & 1 \end{pmatrix} & \text{in [001]-direction.} \end{cases} \quad (5.9)$$

The double inner product ( $:$ ) is the equivalent of a scalar product for vectors.<sup>1</sup> When the crystallographic [100] axis is aligned parallel to the  $x$ -direction, Eq. 5.8 can be written as:

$$\Delta E_c^{[100],[010],[001]} = \Xi_d \text{tr}(\boldsymbol{\varepsilon}) + \Xi_u \boldsymbol{\varepsilon}_{xx,yy,zz}. \quad (5.10)$$

As a consequence for the  $\Delta$  valley along the [100]-direction only the strain component  $\boldsymbol{\varepsilon}_{xx}$  contributes to the energy shift controlled by  $\Xi_u$  (analogously for [010]  $\boldsymbol{\varepsilon}_{yy}$  and for [001]  $\boldsymbol{\varepsilon}_{zz}$ ).

**Valence Band** For the strain dependent deformation, we select the approach introduced by Luttinger and Kohn and improved by Bir and Pikus. Here we solve for their Hamiltonian operator  $H$ . [KL54]·[Lut56]·[CC92]. The basis functions  $|j, m_l\rangle$  denote the Bloch-wave functions at the zone center [CC92] (where  $j$  is the total angular momentum quantum number and  $m_l$  is the magnetic quantum number). In the following, we will describe the electronic states including the coupling of heavy holes (HH  $|3/2, \pm 3/2\rangle$ ), light holes (LH,  $|3/2, \pm 1/2\rangle$ ) and the split-off (SO,  $|1/2, \pm 1/2\rangle$ ) bands. The effect of strain is to remove the degeneracy between HH and LH band; the variation of the valence band energy induced by strain will be defined by  $\Delta E_{v,LH}$ ,  $\Delta E_{v,HH}$  and  $\Delta E_{v,SO}$  for LH, HH and SO, respectively. The general formulation of the Bir-Pikus-Hamiltonian for a strained bulk semiconductor is:

$$H = - \begin{bmatrix} P+Q & -S & R & 0 & -\frac{1}{\sqrt{2}}S & \sqrt{2}R \\ -S^\dagger & P-Q & 0 & R & -\sqrt{2}Q & \sqrt{\frac{3}{2}}S \\ R^\dagger & 0 & P-Q & S & \sqrt{\frac{3}{2}}S^\dagger & \sqrt{2}Q \\ 0 & R^\dagger & S^\dagger & P+Q & -\sqrt{2}R^\dagger & -\frac{1}{\sqrt{2}}S^\dagger \\ -\frac{1}{\sqrt{2}}S^\dagger & -\sqrt{2}Q & \sqrt{\frac{3}{2}}S & -\frac{1}{\sqrt{2}}R & P+\Delta & 0 \\ \sqrt{2}R^\dagger & \sqrt{\frac{3}{2}}S^\dagger & \sqrt{2}Q & -\frac{1}{\sqrt{2}}S & 0 & P+\Delta \end{bmatrix}$$

<sup>1</sup>Given two  $3 \times 3$  matrix  $a$  and  $b$ , the double inner product is  $a : b = \sum_{i,j} a_{ij} b_{ij}$

where we used:

$$\begin{aligned}
P &= P_k + P_\varepsilon, & R &= R_k + R_\varepsilon, \\
Q &= Q_k + Q_\varepsilon, & S &= S_k + S_\varepsilon, \\
P_k &= \frac{\hbar^2}{2m_0} \gamma_1 (k_x^2 + k_y^2 + k_z^2), & P_\varepsilon &= -a_v (\varepsilon_{xx} + \varepsilon_{yy} + \varepsilon_{zz}), \\
Q_k &= \frac{\hbar^2}{2m_0} \gamma_2 (k_x^2 + k_y^2 - 2k_z^2), & Q_\varepsilon &= \frac{b}{2} (\varepsilon_{xx} - \varepsilon_{yy}) - id2\varepsilon_{xy}, \\
R_k &= \sqrt{3} \frac{\hbar^2}{2m_0} [-\gamma_2 (k_x^2 - k_y^2) + 2i\gamma_3 k_x k_z], & R_\varepsilon &= -\frac{\sqrt{3}}{2} (\varepsilon_{xx} + \varepsilon_{yy} - 2\varepsilon_{zz}), \\
S_k &= 2\sqrt{3} \frac{\hbar^2}{2m_0} \gamma_3 (k_x - ik_y) k_z, & S_\varepsilon &= -d (\varepsilon_{zx} - i\varepsilon_{yz}),
\end{aligned}$$

and the basis set:

$$\begin{aligned}
& \left| \frac{3}{2}, \frac{3}{2} \right\rangle \\
& \left| \frac{3}{2}, \frac{1}{2} \right\rangle \\
& \left| \frac{3}{2}, -\frac{1}{2} \right\rangle \\
& \left| \frac{3}{2}, -\frac{3}{2} \right\rangle \\
& \left| \frac{1}{2}, \frac{1}{2} \right\rangle \\
& \left| \frac{1}{2}, -\frac{1}{2} \right\rangle.
\end{aligned}$$

For clarification we denote the wave vector  $k$ , the Luttinger parameters  $\gamma_i$ , the Pir Bikus deformation potentials as  $a_v, b, d$  and  $\Delta$  as the spin-orbit split-off energy. All parameters ( $P, R, S, T$ ) can be split in a strain dependent (index  $\varepsilon$ ) and a wave vector dependent (index  $k$ ) part.

parameter	value	reference
$\Xi_d$	8.7 eV	[Van86]
$\Xi_u$	7.3 eV	[Van86]
$b$	-2.1 eV	[Van86]
$d$	-4.8 eV	[Van86]
$a_v$	2.46 eV	[Van86]
$\Delta$	0.044 eV	[SG89]
$\gamma_1$	4.285	[VN19]
$\gamma_2$	0.339	[VN19]
$\gamma_3$	0.446	[VN19]

Table 5.1: Parameter list for Si used for the strain calculation

The diagonalization of the Luttinger-Kohn Hamiltonian defines the band edge profiles as a function of strain and wave number. In the rest of this chapter, we are describing the band edge at  $k = 0 \text{ m}^{-1}$ . In order to have a complete overview of the effect of strain on valence bands, it is worthed to focus on the most frequent cases in the literature about the strain dependent band edges are reported for the case of the effect of biaxial strain in the xy-plane and uniaxial strain in the [001] direction. An achieved analytical expression for the conduction, valence and split off band can be found in Appendix A.

In the evaluation of the strain-dependent variation of the valence edge (supposing to fix the degenerate edge of HH and LH at  $\varepsilon = 0$ ), we can clearly see (Fig. 5.2) that in-plane biaxial strain

and [001] uniaxial strain have opposite behavior with respect to the strain nature (compressive or tensile).<sup>2</sup> For a tensile biaxial strain, the LH band edge is increasing and the HH band edge is decreasing, while for compressive biaxial it is vice versa. In case of tensile uniaxial strain, the LH-band edge is decreasing and HH-band edge is increasing, while for compressive biaxial strain the HH-band edge is decreasing and the LH-band edge is increasing.

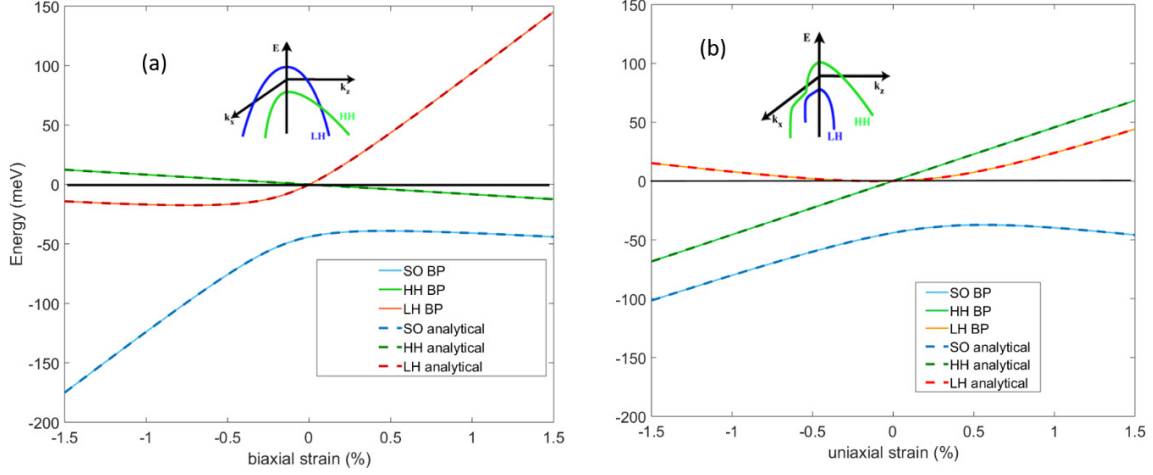


Fig. 5.2: Behaviour of the strain dependent band edge variation for HH, LH and SO as a function of strain in the hypothesis of in-plane biaxial strain (left panel) and [001] uniaxial strain (right panel).

Without loss of generality we set  $\epsilon_{xy}$  and  $\epsilon_{yz}$  to zero motivated by our stripe geometry and hence, we achieved an analytical expression for the eigenvalues. The results obtained with numerical diagonalization (solid lines) are in line with our analytically achieved results (dashed line).

Even milestone papers [CC92] still neglect the  $\epsilon_{xz}$ , but due to our sample geometry, we believe, that  $\epsilon_{xz}$  might have a significant and not negligible role. In the left panel of Fig. 5.3, we can notice that the band edge variation is symmetric with respect to the strain sign variation. Moreover, fixing the value of the uniaxial strain to  $\epsilon_{xx} = 1\%$  and ranging  $\epsilon_{xz} = 0\% - 1\%$ , a variation in the valence band edge can even reach a value of 140 meV, confirming our hypothesis that  $\epsilon_{xz}$  is not negligible, for simulations with  $|\epsilon_{xz}| \geq 0.1\%$ .

In the right panel of Fig.5.3 the resulting variation of the conduction and valence band edge depending on biaxial strain is shown. Here the conduction bands in different directions are calculated according to Eq. (5.11-5.13). Eq. 5.13 is in line with the Varshni rule, that the band gap varies according to the temperature [Var67]. The valence band edge for HH and LH is calculated by Eq. 5.14.

### 5.1.3. LPS simulation model

In order to evaluate the measurability of strain related effects, contrary to the previously chapters, we use a spatial homogeneous doping concentration ( $N_D = 1 \times 10^{16} \text{ cm}^{-3}$ ). The strain

<sup>2</sup>Special thanks to Dr. C. L. Manganeli for these calculations.

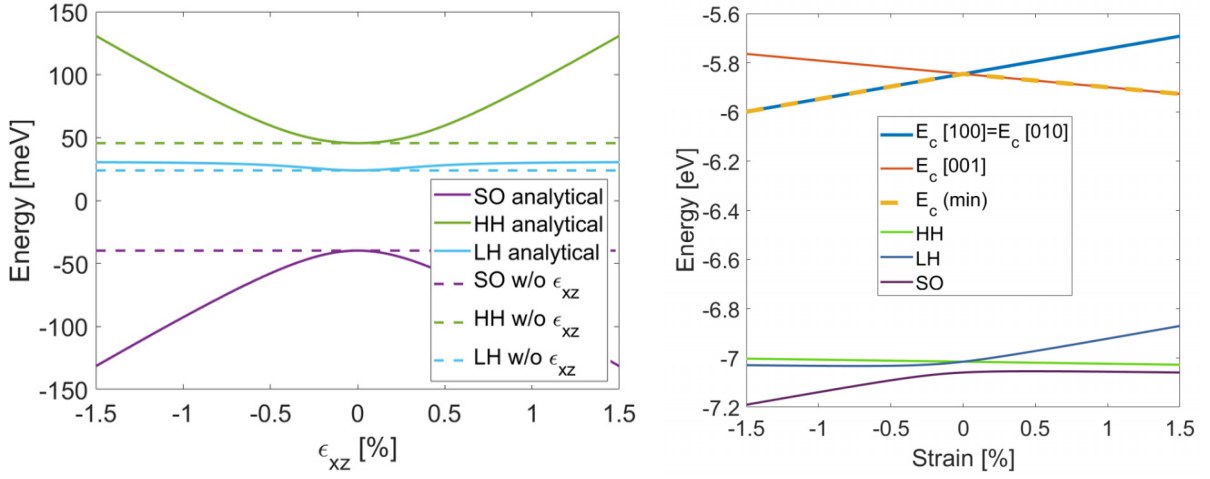


Fig. 5.3: Left panel: effect of non-diagonal component  $\epsilon_{xz}$  on valence band edge in presence of [001] tensile strain of 1 %. The dashed lines are the valence band edge for [001] tensile strain of 1 % without non-diagonal components, the full lines are the band profile with diagonal components. Right panel: resulting band edge variations depending on biaxial strain.

parameter	value	reference
$E_{gv}$	-7.03 eV	[Van86]
$\Delta$	0.044 eV	[SG89]
$E_{gap,ind}$	1.12 eV	[Van86]
$\alpha$	$-4.73 \times 10^{-4}$ e/K	ioffe
$\beta$	636 K	ioffe

$$E_c^i = E_{c,0} + \Delta E_c^i \quad (5.11)$$

$$E_{c,0} = E_{gv} + \frac{\Delta}{3} + E_g \quad (5.12)$$

$$E_g = E_{gap,ind} + \frac{\alpha T^2}{\beta + T} \quad (5.13)$$

$$E_v^{HH,LH} = E_{gv} + \frac{\Delta}{3} + \Delta E_v^{HH,LH} \quad (5.14)$$

field of a structure (will be introduced in the next section) is calculated by FEM using the solid mechanics module of COMSOL Multiphysics. The so achieved spatially resolved strain map is used to define the local value of the conduction and valence bands according to the deformation potential theory, as shown in the previous section. Those band maps are set as an input parameter for the COMSOL Multiphysics LPS simulation, ( $E_c(x)$  and  $E_g(x) = E_c(x) - E_v(x)$ ) The former calculated space dependent conduction and valence bands are introduced in a single band approach (needed in the actual version of the COMSOL Multiphysics semiconductor module) at room temperature, neglecting heating effects originated by the laser beam:

$$E_c = \min \left( E_c^{[100]}, E_c^{[010]}, E_c^{[001]} \right). \quad (5.15)$$

For the valence band the situation appears to be more clear, as the density of states in the HH-band is much higher than in the LH-band at room temperature. So we chose:

$$E_v = E_v^{HH} = E_{gv} + \frac{\Delta}{3} + \Delta E_v^{HH}. \quad (5.16)$$

For the LPS simulation we are using the Arora[AHR82] and Fletcher[Fle57] model describing the charge carrier mobility with respect to scattering by ionized impurities, acoustic phonons and the charge carriers themselves. We are *not* taking into account, the influence of strain on mobility. Considered recombination mechanisms are: Shockley-Read-Hall (SRH), Auger (Au), radiative recombination (Rad) and the effective surface recombination.

An adaptive mesh, which is centrosymmetric to the actual laser spot location, is used for all simulations. In  $z$ -direction we used a swept mesh with increasing size by increasing distance to the Si/Si<sub>3</sub>N<sub>4</sub>-interface, to achieve a periodic modulation of the strain field.

## 5.2. Results and Discussion

As a sample set-up we chose a Si sample covered with an array of Si<sub>3</sub>N<sub>4</sub> stripes (along  $y$ -direction), top panel Fig. 5.4. The pressure originated from the deposition process is applied on the Si<sub>3</sub>N<sub>4</sub> stripes and subsequently propagating in Si. A cross section ( $xz$ -plane) of a Si sample stressed by a single Si<sub>3</sub>N<sub>4</sub> stripes is shown in left bottom panel of Fig. 5.4. Motivated by the sample geometry,  $\epsilon_{xx}$  is assumed to be dominant, while  $\epsilon_{xy}$  and  $\epsilon_{yz}$  are vanishing. On the left the strain trace field is shown by a colormap (right axis) and the presence of compressive lobes at sides of the Si<sub>3</sub>N<sub>4</sub> stripes are clearly visible. On the right the behaviour of the dominant strain component ( $\epsilon_{xx}$ ) profile at different vertical distances from the Si-Si<sub>3</sub>N<sub>4</sub> interface is demonstrating a non negligible strain profile even 2  $\mu\text{m}$  below the stressor.

In Fig. 5.5 we show the non-negligible strain components at a depth level of 100nm as a function of the transverse direction  $x$ . In opposition to the  $\epsilon_{xx}$  and  $\epsilon_{zz}$  component, which are even functions, the  $\epsilon_{xz}$  component features an odd symmetry. The antisymmetric nature of the non-diagonal components derive from the hypothesis of absence of internal forces, which is directly determining from Hooke's law by the absence of angular acceleration and the symmetry of the strain tensor. Therefore not only the shear stress component  $\sigma_{xy}$  is flipping sign with respect to  $x$ , hence also the shear strain component  $\epsilon_{xy}$  [JHAP95] flips. The observation of  $\epsilon_{xx}$  and  $\epsilon_{zz}$  components shows, that the strain almost vanishes in-between two stripes, hence the array of stripes can be seen as multiple single stripes placed next to each other allowing no cross talk.

Due to this configuration we are allowed to describe the effects of the strain to the band edges on a single stripe (located at  $x = 1.37 \text{ mm} - 1.39 \text{ mm}$ ) giving a full representation for the whole array of stripes. In Fig. 5.6 we see the overall stripe like shape in the top most panel and the strain, conduction and valence bands in proximity to the stripe boundaries. As stated before,  $\epsilon_{yy}$ ,  $\epsilon_{yz}$  and  $\epsilon_{xy}$  components are vanishing due to the sample geometry. Following Eq. (5.15) the strain induced variation on the conduction bands is presenting a common off-set linked to the strain trace in all directions, however  $E_c^{[100]}$  is mainly reproducing the profile of  $\epsilon_{xx}$  (analogously  $E_c^{[001]}$  and  $\epsilon_{zz}$ ). Due to the absence of  $\epsilon_{yy}$ ,  $E_c^{[010]}$  shows significantly smaller variations. For the minimum conduction band marked as purple line, it can be seen, that every conduction band component according to [100], [010] and [001] direction is contributing, and hence none of them are negligible.

The valence band profiles are obtained according to the former introduced model of the Bir-Pikus-Hamiltonian and its diagonalization resulting in Eq. (5.16). It is worth noticing, that the non-diagonal strain components ( $\epsilon_{xz} = -\epsilon_{-xz}$ ) feature an odd nature, while the band-edges are symmetric for the sign variation. The peak for  $E_v^{LH}$  is located outside of the stressor covered region in opposition to the peak for  $E_v^{HH}$ , which is located inside.

Simulated LPS profiles will be compared to conduction and valence band variations caused by strain variations. For this, we remind the reader to the former definition of  $U_{LPS}$ :

$$U_{LPS} = \Phi_{x_{\text{end}}} - \Phi_{x=0}. \quad (5.17)$$



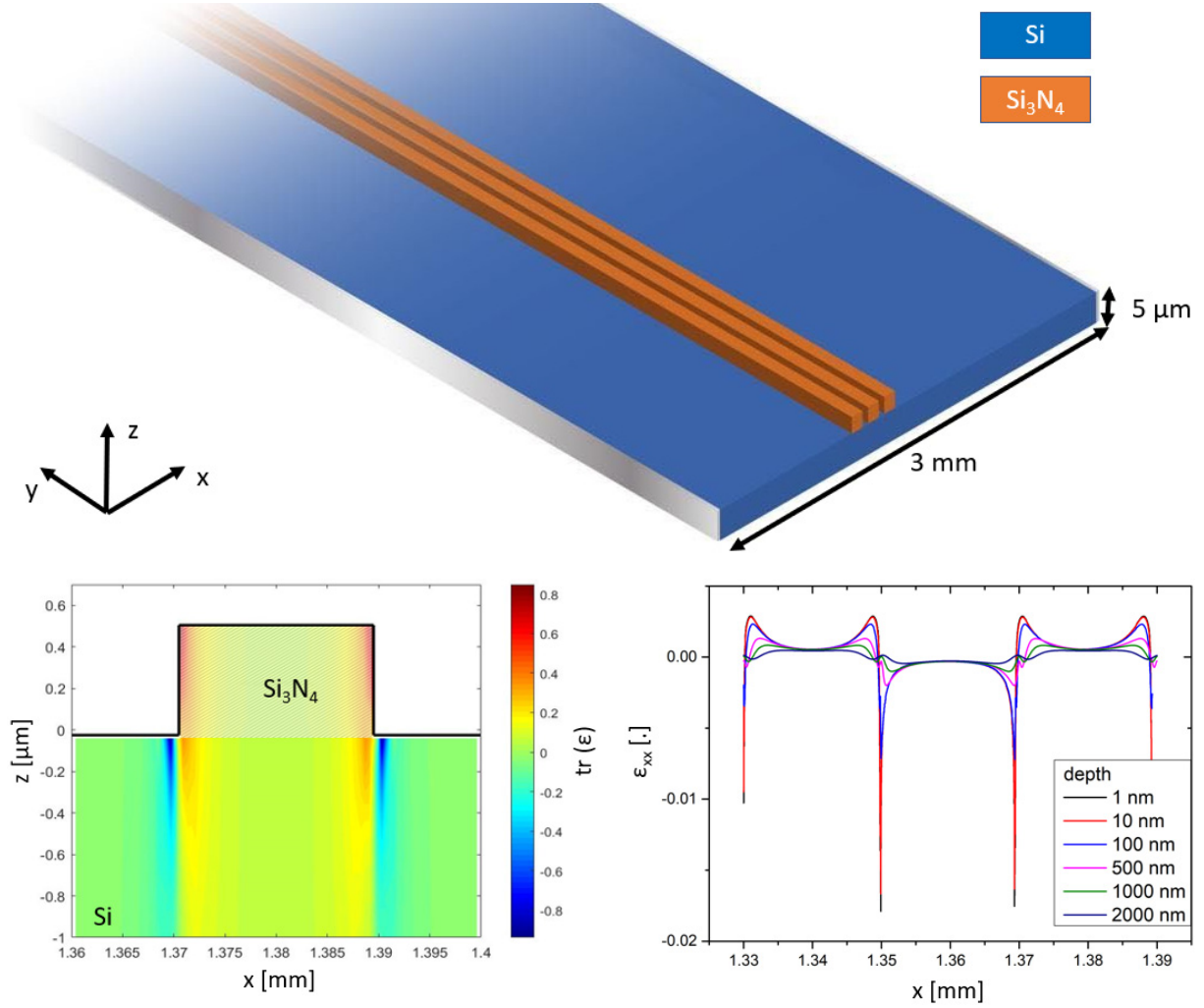


Fig. 5.4: Top panel: three dimensional sample geometry assuming an infinite length in the  $y$ -direction. Bottom left panel: strain trace field generated by a  $\text{Si}_3\text{N}_4$  stressor with 4 GPa initial in plane stress on top of a Si sample. Bottom right panel: strain profiles of the dominant  $\epsilon_{xx}$  component evaluated at different depth levels.

We used the 2D calculated strain dependent conduction and valence band values of Fig. 5.6 (bottom panels) as input for LPS simulations. It is worth to notice that the optical transmission of  $\text{Si}_3\text{N}_4$  is not only depending on the used laser wavelength, but also on the layer thickness itself. So the laser beam is assumed to be only absorbed by the under-laying Si sample. In our simulation we neglect effects associated to different interfaces (Si– $\text{Si}_3\text{N}_4$ , Si–air). This could also be avoided by using an homogeneous top on non-stressed  $\text{Si}_3\text{N}_4$ . Here only one overall interface Si– $\text{Si}_3\text{N}_4$  exists, which should not interfere with our simulation.

The presence of n-type doping ( $N_D = 1 \times 10^{16} \text{ cm}^{-3}$ ) adds a screening effect to the conduction band, but not the valence band. The screening effect is linked to the electrostatic potential  $e\Phi$ , which is flattening the conduction band profile  $E_{c,\text{eff}} = E_c + e\Phi = \text{const}$ . As the band gap is not effected by the screening, the effective valence band  $E_{v,\text{eff}} = E_v + e\Phi$  contains information of its former definition,  $E_v$ , and of the conduction band variation via  $e\Phi$ .

By an illumination, simulated by a Gaussian laser profile using a standard deviation of  $1.25 \mu\text{m}$  and an exponential decay in the  $z$ -direction ( $4.8 \mu\text{m}$  penetration depth), the generated

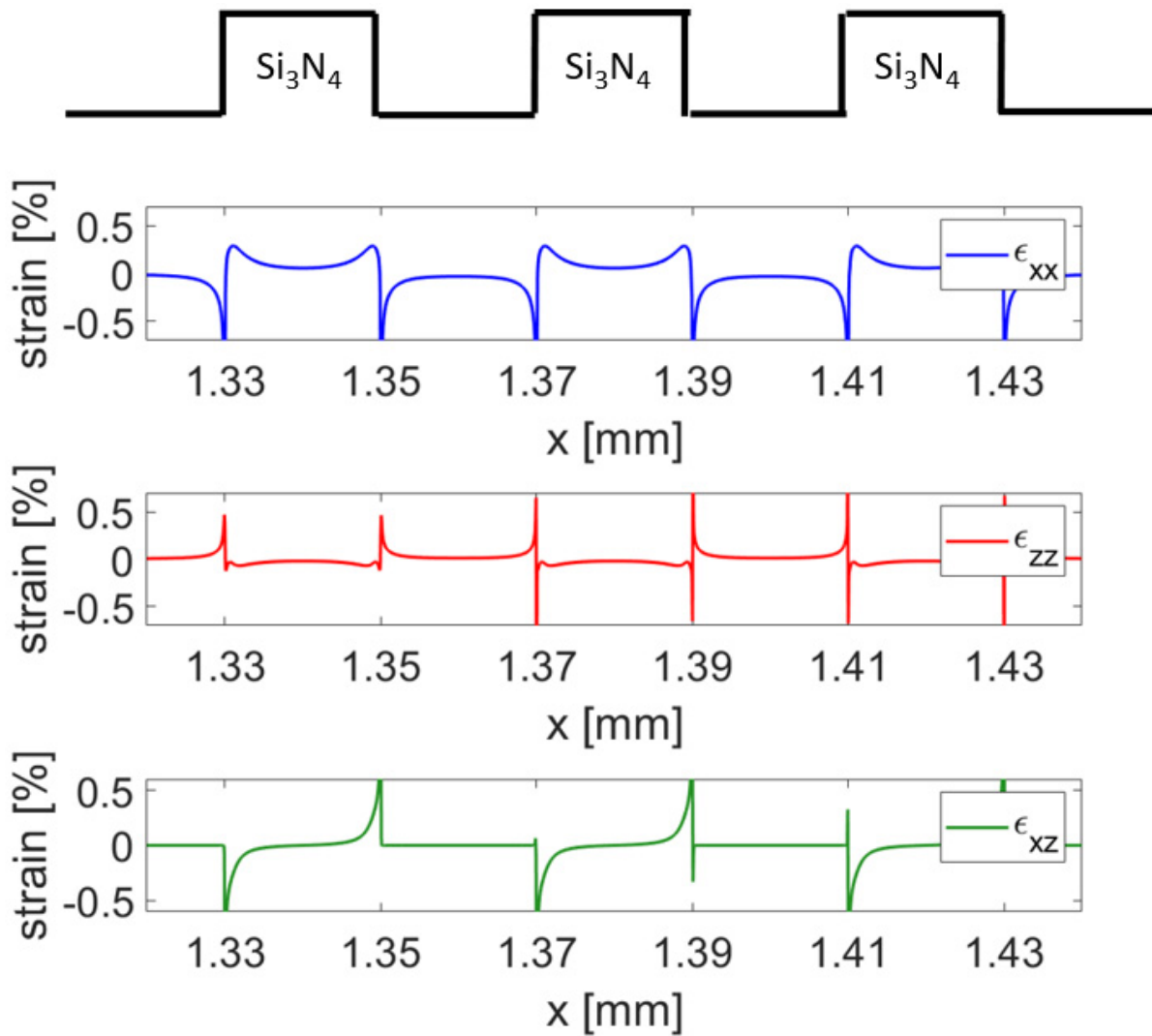


Fig. 5.5: Single strain components for the geometry taken 100 nm below the top surface.

electrons (holes) will drift accordingly to their effective conduction (valence) band. Hence, for the electrons, beside coulomb interactions due to the inhomogeneous hole distribution, only rotational symmetric diffusion occurs. On the other hand, the holes will additionally drift as the effective valence band is not constant. This drift motion of the holes is majorly determining for the LPS-voltage, by means of generating charge carrier dipole.

Fig. 5.7 left panel shows a profile of the effective valence band (right vertical axis) and a profile of the LPS-voltage as a function of the laser spot position. Analogously to the previously shown figures, the on top stressor is deposit in the range 1.37 mm - 1.39 mm. The profile of the effective valence band indicates two hole confining potentials located directly at the stressor stripe edges. The LPS-voltage shows the same periodicity as the causative effective valence band modulation. Before discussing the profile in detail, we can still see an logarithmic functionality of the LPS-voltage depending on the laser pump power (see Fig.5.7 right panel).

We now want to simplify and decouple the presented system for a more intelligible picture of the LPS- voltage profile (shown in Fig.5.7 left panel) by keeping comparable  $E_{v,eff}$  profiles. Therefore we made case studies in a quasi one dimensional model by thinning the sample

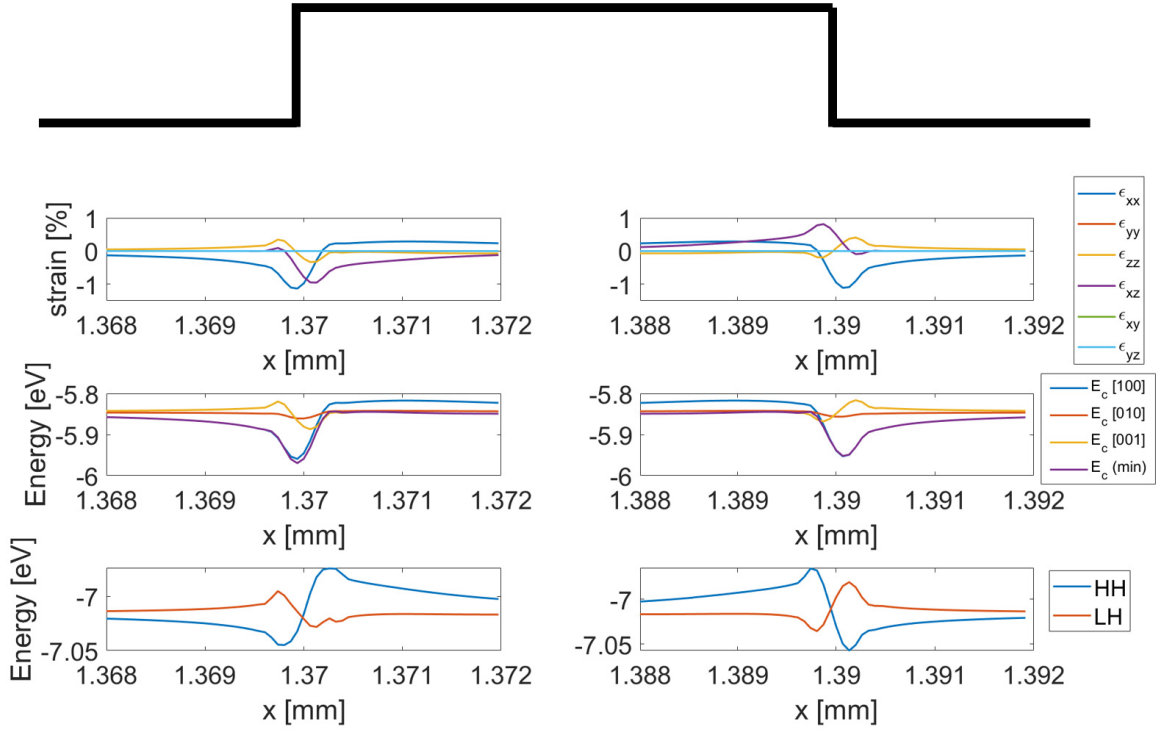


Fig. 5.6: Behavior of strain profile (top), conduction band (middle) and valence band (down) at both sides of the stripe.

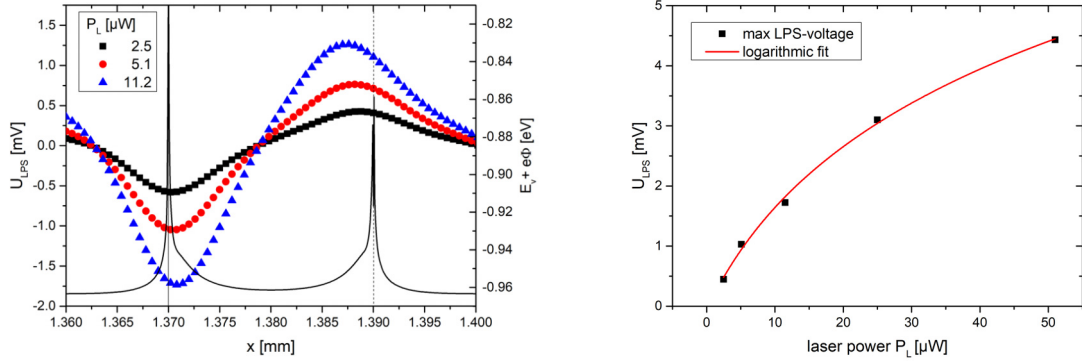


Fig. 5.7: Left panel: LPS-voltage profile (left axis) and the therefore simulated effective valence band edge profile extracted at  $z = 100$  nm. Right panel: LPS-voltage depending on the laser pump power at  $x = 1.3705$  mm

thickness (less than  $1 \mu\text{m}$ ). As in this case the sample thickness is much smaller than the penetration depth, we assume a constant generation rate in the  $z$ -direction. The out-coming LPS-voltage might differ in comparison to a full two dimensional approach, just by reducing the model dimension. To get better inside we intentionally chose a small laser pump power injection to increase the local resolution (chapter IV.)

For the first analyses we wanted to describe the effect of a single symmetrical hole con-

fining potential. Therefore we assumed a constant conduction band edge profile and a Gaussian shaped hole confining potential for the valence band edge. As a constant doping  $N_D = 1 \times 10^{16} \text{ cm}^{-3}$  is assumed, the shape of  $E_{v,\text{eff}}$  is preserved as  $E_c$  is spatially invariant. We simulate  $E_v$  as an artificial Gaussian function (see Fig.5.8 left panel) keeping its width comparable to the profile used in Fig. 5.7 left panel. If we directly illuminate at the center of the hole confining potential that electric potential generated by the laser pump power does not influence the Gaussian behaviour significantly and the effective valence band extracted at equilibrium and excited conditions overlap.

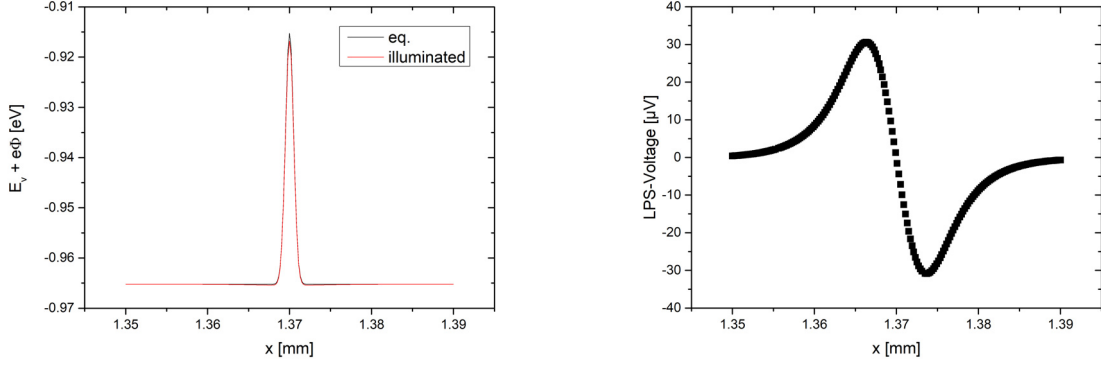


Fig. 5.8: Left panel: effective valence band edge profile for a (non)-illuminated sample marked in red (black). Right panel: calculated LPS-voltage with respect to the laser spot position.

In the right panel of Fig.5.8, we see the corresponding LPS-voltage with respect to the laser spot position. The LPS-voltage decreases, as expected to completely vanish far away from the hole confining potential. Responsible for this is the diffusion length (approx  $5 \mu\text{m}$ ) of the excess charge carriers. If excess charge carrier can not reach the location of the hole confining potential by drift and/or diffusion, they will not generate a dipole and so a potential difference at the sample edges. As a confirmation of this status, the symmetry of the hole confining potential is determining no LPS-voltage by illuminating at the center of the trap. Due to the symmetry of the trap, charge carriers will be pushed (in case of electrons) away or pull (in case of holes) towards the center of the trap symmetrically and hence, can not result in an effective dipole, which is in line with our results.

To better understand the LPS-voltage we investigate two cases with different excess charge carrier distribution, where the laser spot position were at 1.365 mm and 1.375 mm. For the next six figures an illumination at 1.365 mm (1.375 mm) is always indicated as a black (red) solid line.

By looking at the charge carrier distributions for electrons (holes) in Fig. 5.9 left (right) panel, it is clear, that low injection conditions are fulfilled, as  $\Delta n = \Delta p$  are two orders of magnitude smaller than the doping of  $N_D = 1 \times 10^{16} \text{ cm}^{-3}$ . Every line has two peaks, one located at the laser spot positions and one located at the hole confining potential. By reminding of the fact, that the conduction band profile is assumed constant and the valence band profile is assumed as an artificial Gaussian shaped function, it is clear, that the band gap in this region is smaller in comparison to the surrounding area. As the intrinsic charge carrier distribution  $n_i$  depends on the band gap  $E_g$ :

$$n_i \propto \exp(-E_g), \quad (5.18)$$

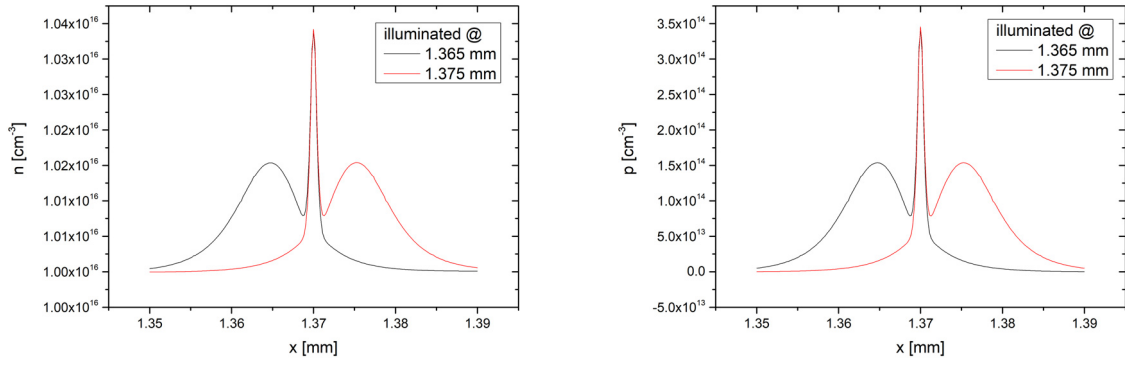


Fig. 5.9: Charge carrier densities for electrons (holes) are shown in the left (right) panel.

a lowering in the band gap results in a larger intrinsic charge carrier distribution. Hence, a larger equilibrium value for the charge carriers ( $n, p$ ) can be observed in the hole confining potential region. Also the Coulomb attraction of electrons and holes in this hole confining potential region causes a peak in the electron distribution. The central peak in Fig. 5.9 is nearly independent on illumination. This can be seen in the results as, even for two different located laser spot positions, the charge carrier density in this region is perfectly overlapping. If the effect is majorly depending on the excess charge carrier density and so on the laser spot position, we would see a change at least in the flank region of the peak.

Fig. 5.10 left panel shows the net charge carrier concentration  $\rho = q(p - N_A - n + N_D)$ . At first glance this figure appears like a normal beam spot profile, as electrons can diffuse further than holes, which creates a central positive region flanked by two negative areas. However, this is not the correct interpretation, as the center of this peak is independent on laser spot position. As previously stated we can directly see the effect of the hole confining potential located at  $x = 1.37$  mm affecting the total amount of inherent charge carriers. The hole confining potential attracts holes, therefore we see a strong positive concentration in the center and a negative depletion zone in its surrounding area.

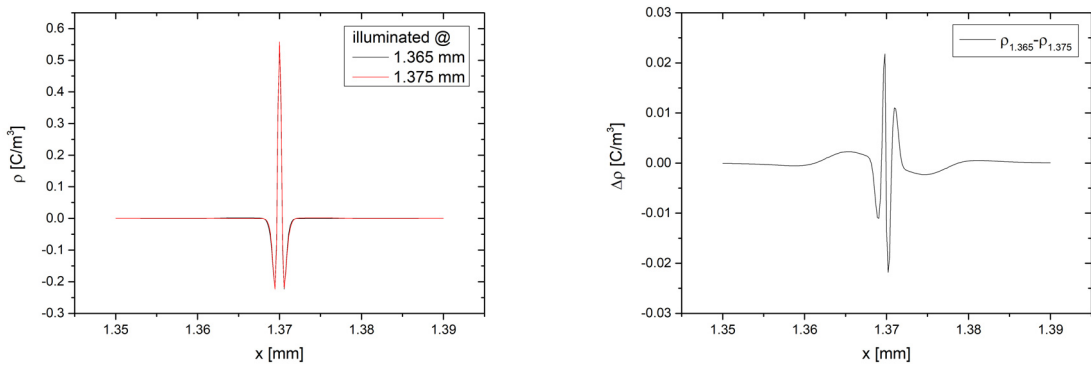


Fig. 5.10: Left panel: net charge carrier concentration profiles. Right panel: shows the difference between the shown net charge carrier distributions.

The right panel of Fig. 5.10 shows the difference between the net charge carrier densities

obtained with illuminations at different laser spot positions (black and red line of the left panel). Here we see two broad peaks located at the two described laser spot positions. In case of electrons and holes with the same mobility, these two peaks would be vanishing. Moreover we can clearly see the presence of the central peaks in proximity of the hole confining potential. On a quantitative way, by comparing  $\Delta\rho$  and  $\rho$  values, we can conclude, that the variation of  $\Delta\rho$  is at least one order of magnitude smaller then the variation of  $\rho$ . Therefore we can state that the profile of the charge carrier density is not majorly affected by the two different laser spot positions in proximity of the hole confining potential.

In chapter IV, we discussed the local resolution of the LPS method by a Gaussian convolution function. Therefore it might be intuitive, that a sequence of alternative heavily charged regions might have a smaller effect then a broadened region with a small but defined charge. Applying this concept on the  $\Delta\rho$  profile, the variation in proximity to the hole confining potential may play a subordinate role in comparison to the peaks located at the illumination spots.

The full picture is captured with a detailed analysis of the behaviour of the electric field, as in Fig. 5.11 left panel the x-component is described. To have a better picture, we can separate it in three parts, region (I) in grey: 1.35 mm - 1.365 mm and 1.375 mm - 1.39 mm, region (II) in yellow: 1.3675 mm - 1.3725 mm and region (III) in white: the remaining part between the hole confining potential (region (II)) and the laser spot positions. In region (I) the differences between the red and black line are hardly visible. Still on the left (right) side the black (red) line has a non-zero electric field components as a consequence of the proximity to the laser spot. In the hole confining potential region (II), the red and black curve are again matching perfectly. This confirms that there is no effective LPS-voltage if the electric field component is not effected by the excess charge carriers generated by illumination. In region (III) the differences between the shown graphs are the largest. The generated excess carriers, explicitly the holes, will move towards the hole confining potential generating an electric field. Due to the different directions the holes are moving, the peaks values in this area have a different sign, generating dipoles differently oriented. This variation of orientation is mainly responsible of voltage changes, bringing us to the conclusion that region (III) is the most relevant for the observation of the LPS-voltage.

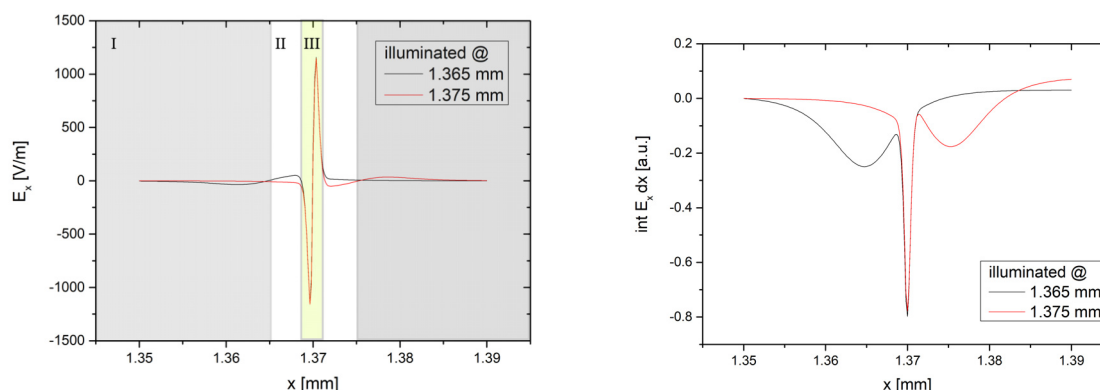


Fig. 5.11: Left panel: lateral electric field. Right panel: its integration.

On the right panel in Fig. 5.11 we integrated the electric field component shown in the left panel.

Due to the quasi one dimensional approach, the potential is only connected to the electric field component along this direction:  $\Phi = \int -E dx$ . The LPS-voltage is assumed to be the difference between the potential evaluated at the two sample edges, hence:

$$U_{\text{LPS}} = \Phi_{x_{\text{end}}} - \Phi_{x=0} = \int_0^{\text{end}} -(E_{\text{ill}} - E_{\text{non-ill}}) dx. \quad (5.19)$$

The right panel of Fig. 5.11 is showing only a selection of the total integral of Eq. (5.19). For graphical reasons we set  $\Phi_{x=1.35\text{mm}} = 0\text{V}$  resulting in a positive shift of the black line and in a non-negative value of  $\Phi_{x=1.39\text{mm}}$ . As a further consequence of this approximation is that black and red line match perfectly in the region of the hole confining potential, indicating, that this region does not have an significant impact to the LPS-voltage.

After discussing a single isolated hole confining potential in detail, we want to discuss two asymmetric hole confining potentials separated by  $20\ \mu\text{m}$ , which is the same distance as the pit length in Fig. 5.7, also shown for better comparison in the right panel of Fig. 5.12. In order to have the mentioned strong asymmetry as the simulated profile of Fig. 5.7, we chose two half Gaussian profiles for the valence band edge (shown in right axis the left panel of Fig. 5.12 with black and red lines). On the left axis we show the LPS-voltage with respect to the laser spot position. The maxima of the LPS-voltage resulting from the two different semi-Gaussian valence band profiles are only slightly shifted. Using one semi-Gaussian profile or the other may be translated in a small shift of the hole confining potential position. However, despite this small shift both LPS profiles fulfill the requirement of the periodicity shown in the full simulation (right panel).

Moreover, we have to state that the semi-Gaussian shape is influencing the LPS-voltage intensity. Indeed, if the laser spot position is located closer to the Gaussian flank, the LPS-voltage is higher than in the case of a laser spot located closer to the cut flank. Although the intuitive erroneous explanation for this is that the gradient of the Gaussian flank is smaller than the gradient of the cut flank, the higher intensity in proximity of the Gaussian flanks is presenting a wider trap width attracting more holes and so increasing the intensity of the LPS-voltage.<sup>3</sup>

Before concluding this section, we want to stress again the differences in the simulation set-ups generating these results shown in 5.12 left and right panel. The results on the left side were achieved using a quasi one dimensional set-up, resulting in no laser penetration in the  $z$ -direction. Moreover, the effective valence band edge profile is independent on the  $z$ -direction. Results on the right side were achieved by two dimensional calculation of a strain profile generated from a top  $\text{Si}_3\text{N}_4$  stressor, affecting the conduction and valence band. Due to the doping, the effective conduction band edge gets completely flat and the information on the strain induced variation is basically stored in the effective valence band edge profile. The difference in the laser power used for these calculations had a distinct purpose. On the left side we intentionally decreased the laser power significantly to increase the local resolution. In contrast, on the right side, we made sure, that the resulting LPS-voltage is larger then  $100\ \mu\text{V}$ . This value most likely guarantees the measurability by keeping track of realistic laser pump power values.

---

<sup>3</sup>This case is analogously to a brachistochrone motion of balls, where not the trajectory with the largest gradient let the balls, get to the end of the trajectory first.

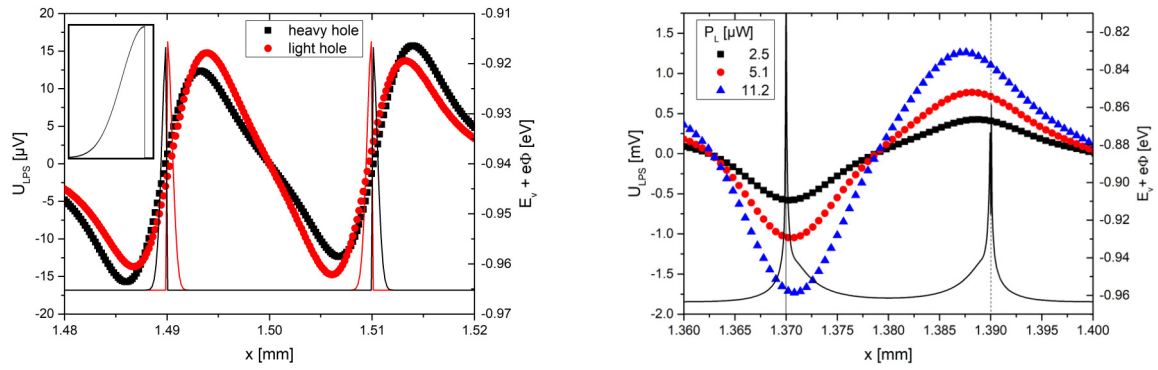


Fig. 5.12: Left panel: calculated LPS-voltage with respect to the laser spot position in quasi one dimensional sample geometry. As an inlay a semi-Gaussian profile is shown. Right panel: calculated LPS-voltage with respect to the laser spot position in two dimensional sample geometry.

Despite all these mentioned differences, the signals feature several equal properties. The peaks inside of a stripe are basically located at the same spots, close to the hole confining potential. Also the sign of the signal is varying in the same way, giving a clear sign, that the interpretation using the effective valence band edge distribution (responsible of the LPS-results) is reasonable. The peaks outside of the stripes do not feature a similar dependency. However, it has to be kept in mind, that the simulation set-up related to the graph on the right side includes a stripe array. As a consequence, considering the relatively large diffusion length  $5\ \mu\text{m}$  in comparison to the pit distance  $20\ \mu\text{m}$ , a "cross talk" between the stripes is unavoidable. We stress again, that the sample geometry was chosen to have realistic and obtainable strain conditions and is not designed for an optimal LPS-result.

### 5.3. Conclusion

We implemented a simulation tool in COMSOL Multiphysics connecting the solid-mechanics and semiconductor module. The coupling was realized by implementing the effects of strain to the conduction and valence band in line with the deformation potential theory, by using an analytic approach for the eigenvalues of the Luttinger-Kohn-Hamiltonian. Here we do *not* neglect the non-diagonal strain component  $\epsilon_{xy}$ , which we showed to have a significant impact on the calculated eigenvalues. Despite having solved the Bir-Pikus Hamiltonian for three different eigenvalue pairs, heavy hole, light hole and the split of band, COMSOL Multiphysics is only able to calculate in a single band approach. Therefore still the most reasonable band has to be selected.

By using a realistic set-up for a Si sampled stressed by a top  $\text{Si}_3\text{N}_4$  stressor, we were able to calculate the correlated conduction and valence band profiles testing Tauc's prediction, that the bulk photovoltaic effect might be used detecting any quantity affecting the conduction and valence band on a level of strain. We could clearly see a varying LPS-voltage with respect to the effective valence band variation. This proves Tauc's theory and gives the opportunity to measure the strain related conduction and valence band profiles using the LPS-technology.

Additionally we build a simplified quasi one dimensional simulation model probing for several



features in detected LPS-voltage. Here we showed that the peaks in the LPS-voltage can be interpreted by the existence of hole confining potentials. In general this means that the detectable LPS-voltage in a doped semiconductor is heavily depending on the effective band profile of the minority charge carriers, which might contain information from the conduction *and* valence band edge profile. Due to this inside, a new sample geometry might be designed increasing the LPS-voltage and thus offering a higher likelihood to measure this effect directly.

We showed, that stripe width of 20  $\mu\text{m}$  might be sufficient probing for peaks underlying the stripe geometry. Also an inter-stripe width of 20  $\mu\text{m}$  was not sufficient to avoid "cross talk". For real measurements it is highly recommended to increase this value.

The perspectives of this activity are clearly located in the framework of a complete analysis of strain and strain gradient effect in semiconductors. On the one hand, the LPS approach can probe strain non-uniformity, on the other hand, the approach shown in this chapter can be extended to other semiconductor micro-structures. As an example, suspended Germanium structures can be analyzed and further designed to improve their potential as integrated light emitters on Si photonics platforms.



## Summary and Outlook

We implemented COMSOL Multiphysics program model simulating LPS measurement using FVM. Due to a model separation into a signal transmission and a signal generation part ①, it was possible to directly compare simulation and measurement results. Interestingly a distortion of the LPS signal could be measured and simulated by investigating the signal transmission. Here rectangular sample usually, occurring by cutting the main part of an ingot along the growth direction, are preferred for an LPS measurement, as no distortion is observed ②. In opposition circular (usually wafers) or trapezoidal (cone of an ingot) generate distorted measurement, with respect to the actual sample with. Due to this physical dependency, undistorted LPS maps can be achieved by post-measurement rescaling. This allows, just by knowing the sample size to use the absolute value of the LPS voltage as well-defined quantity. Formerly just the shape of the striation could be used for a quality investigation of the samples. By investigating the signal generation, we observed ③:

- that the LPS voltage is proportional to the doping gradient,
- that the LPS-voltage saturates with respect to the laser pump power and
- a logarithmic dependency of the LPS voltage for small laser pump powers.

All those observations were theoretically discussed by Tauc using a simplified model and not self-consistent assumptions. Still our investigations show their validity even in a full 3D sample geometry using, with standard semiconductor assumptions. Nevertheless, those investigation are a validation for our model, which now is ready to use the advantages of the three-dimensional sample geometry for further analysis, which where not able in the model introduced by Tauc.

Using this set-up, we were able to analyzed the local resolution of this method. Formerly as a benchmark for the local resolution was used the laser spot diameter, which neglects the sample inherent charge carrier motion by drift and diffusion. Still frequency analyses of the measured signal were made by Ludge et al. [LR97], showing for a specific Si sample, that wavelength smaller 100  $\mu\text{m}$  are heavily suppressed. Hence, they assumed the local resolution to be in this order of magnitude. Unfortunately, they could not completely distinguish whether these low wavelength are occurring in a FZ Si crystal, or whether the method itself suppresses those.

By using our introduced full three-dimensional FVM simulation, we can directly define the structure investigating for. Additionally, we used ion deposition to directly define a patterned structure in commercially FZ Si wafers. The stripe structure got verified by using SIMS technology and so we reduced the uncertainty of the stripe structure to the local detection limit of the used SIMS method. Now we could use Tauc's first prediction to compare integrated LPS scans with the doping profile.

Here we could see that the integrated LPS signal does not follow the rectangular shaped doping profile and is smeared out ④. For further investigations we defined a Gaussian convolution function and applied it on the doping profiles varying the standard deviation of the Gaussian convolution function. For every integrated LPS profile we achieved a very good agreement, with the convolved doping profiles. As integration (LPS profiles) and convolution are commutative, it suggested that the LPS profiles themselves are convolved by a Gaussian function and not just its integration. By further analyses of the standard

deviation of the so achieved Gaussian convolution function, we were able to directly compare measurements and simulations. Here we could detect a more ambivalent result, as for high doped ( $1.9 \times 10^{15} \text{ cm}^{-3}$ ) a nearly perfect agreement could be shown. A slowly increasing behavior of the standard deviation, representing a decrease in the local resolution with respect to the laser pump power. This is in agreement with Ludge et al. , where they suggested to always measure with the lowest possible laser pump power (5) to increase the local resolution. For the lower doped samples larger deviation between measurement and simulation was detectable, up to a factor of two. Still the same tendency between local resolution and laser pump power could be seen. The difference between measurements and simulation might be caused by several reasons. In the simulation we kept the SRH-recombination lifetime constant for all three samples. Measurements of the lifetime show, that the mean value is equal for all three samples, but the local variation on the wafers is varying much stronger in the low doped wafers. Here our simulation might have underestimated the charge carrier lifetime, which causes a better local resolution. Also, the dose of implanted boron ions kept the same for all three samples, which causes different step height in the doping concentration, as the background level is different. Therefore, it can be assumed that the samples having the largest step height, so the highest non-steady profile causing the largest difficulties in semiconductor computation. Hence, former small variations in the wafers with high doping profile jumps might cause higher deviations between simulation and measurements.

It must be said that, these large unsteady jumps in the doping concentration do not occur in naturally grown FZ or Cz Si even assuming a central facet. As we now know, that a Gaussian function might be causative describing the local resolution, it might be worth trying to deconvolve the measured LPS profiles to reconstruct the inherent doping profile. Then, the LPS measurement set-up might be used as a resistivity measurement tool avoiding the large tip-to-tip distance ( $\approx 0.6 \text{ mm}$ ), which results in a poor local resolution. This add on to the set-up inherent modifications of an LPS-measurement (fast, cheap and non-destructive). A first and easy test could be done by using the common OriginPro 9.1 software, which is able to deconvolve signals with respect to a known Gaussian convolution function. Here the problem occurs, that the standard deviation of the Gaussian convolution function is sample dependent and has to be detected in advance. The shown results might not be used for common FZ or Cz- Si samples, because the charge carrier life time dropped due to the ion implantation significantly. To avoid this detection of the Gaussian convolution function, a self-learning artificial intelligence AI might be trained by simulated data achieved by COMSOL Multiphysics. Hence, after training, the AI could deconvolve the measured data.

The possible usage of LPS as a resistivity measurement tool is still limited. Up to now, LPS is only measurable on Si, Ge and  $\text{Si}_x\text{Ge}_{1-x}$ , and so limited to indirect semiconductor materials. In case of direct semiconductors, the recombination time and so the total amount for free charge carriers is heavily reduced. As we have seen is the LPS voltage assumed to be proportional to the logarithm of the laser pump power, hence the total amount of free charge carriers. This suggests that only materials featuring a large charge carrier lifetime might be candidates for further investigation increasing the pool of material LPS can be used. As the COMSOL Multiphysics code can be easily adapted to different sample material, it guides further investigations. For the analysis of Tauc's thesis, that the bulk photovoltaic effect, causative for the LPS voltage, might be used detecting any physical quantity, which is depending on the band structure profile, we combined FEM strain simulations by the deformation potential theory to connect local strain variations to conduction and valence band variation. We could theoretically proof that the LPS voltage is suitable to detect band profile variations, caused by

an unisotropic strain profile. Eventhough we took care of the measurability by using a realistic geometry and reasonable parameters, a final measurement verifying our results, is still missing. Due to the fact, that we combined the solid mechanics and semiconductor model directly in one program, this code gained more degrees of freedom. For example, different sample geometries and stressor material can be included in the strain simulation using the solid mechanics model. For substrate materials we are at the moment limited to Si, as the deformation potentials are only implemented for Si. But in the deformation potential theory Ge, GaAs, InP are also well described and can be implemented as substrate materials. Up to now, we would be able to simulate complex geometries using any on top stressor on different substrate materials gaining its non-uniform band profiles. Due to the semiconductor model those achieved band profiles can directly be used simulating measurements, e.g. as shown for the LPS-voltage. Also suitable measurements to be simulated are the resistivity profile or the temperature dependent hall effect. Hence, we build a multi flexible simulation program for analyzing physical quantities in stressed semiconductors.

Stressed Ge semiconductors became focus of the semiconductor community as a population inversion could be measured [BKO<sup>+</sup>17, LSP<sup>+</sup>07] in 2007. Therefore Ge on Si lasers have been performed [CACP<sup>+</sup>12], which are assumed to fill the gap of an effective laser source on Si [ZYM15, Sor06], making fully functional photonic-integrated circuits (PICs) possible [BKO<sup>+</sup>17]. Several miniaturizations such as light detection and ranging (LIDAR) for autonomous vehicles [STY<sup>+</sup>13], bio-chemical sensors [Sor10] and chip-level optical communication [Mil10] are driven by PICs development. Theoretical simulations predict for altering band structures by strain a significant reduction in lasing threshold through tensile strain [VMG<sup>+</sup>13, PTG<sup>+</sup>15] and therefore improving PICs in line with the more then Moore approach. At the moment several innovative platforms inducing large strain are in discussion [CKY<sup>+</sup>13, BKO<sup>+</sup>17] showing the demand for also innovative strain measurement and simulation tools. Therefore the shown possibility for LPS to measure strain-related conduction/valence band effects might contribute to this development. Additionally the flexible COMSOL Multiphysics simulation program, which calculates strain-related conduction and valence band profiles and directly connect those to classical semiconductor measurements/simulation, opens new possibilities for investigations.



## Acknowledgement

I would like to thank the Leibniz Institute for Crystal Growth, the group Classical Semiconductors and their members for the constructive and friendly working environment.

Special thanks also go to the actual head of the Leibniz Institute for Crystal Growth Prof. Dr. T. Schröder and his predecessor Prof. Dr. G. Tränkle and C. Wenger, leader of the Adaptive Materials for Sensing and Computing group at ihp for their vote of confidence in my work.

Dr. M. Virgilio, who was not just supervising me, he critical advised and created ideas. Therefore I am thankful.

I am thanking Dr. A. Lüdge for supervising me in the first couple of years.

Particularly I am honouring my departure head Dr. F. M. Kießling and Dr. N. V. Abrosimov. They always supported me and my ideas investigating on interesting samples.

I would like to thank for the excellent cooperation with sample preparation and characterization K. Berger, I. Buchovska, M. Czupalla, Dr. T. Ervik, J. Fischer, Dr. C. Guguschev, B. Hallmann-Seifert, M. Imming-Friedland, Dr. K. Irmscher, Dr. U. Juda, U. Kupfer, Dr. A. Kwasniewski, V. Lange, L. Lehmann, Dr. R. Menzel, Dr. W. Miller, K. Reinhold, M. Renner, Dr. H. Riemann, B. Spotowitz, T. Turschner, S. Weiß and M. Ziem.

I feel enormous gratitude to Dr. C. Dadzis and Dr. K. Böttcher for their expertise in creating the simulation model.

Especially I am emphasizing the collaboration to the ihp- Innovations for High Performance Microelectronics and the WIAS-Weierstrass Institute for Applied Analysis and Stochastics. Representatively named therefore are: Prof. Dr. G. Capellini (ihp), Dr. C. L. Manganelli (ihp), Dr. P. Farrell (WIAS), Dr. N. Rotundo (WIAS) and Dr. T. Koprucki (WIAS).

I found good resonance for inspiring conversations for different topics. For this social contact I thank Dr. C. Frank-Rotsch, Dr. N. Dropka, Dr. T. Boeck and B. Ruthenberg.

A cup of coffee and additionally a constructive conversation can heal sorrows and enable a PhD thesis. Therefore I thank all participants including the coffee.

Finally I want to gratitude my family, my colleges and my girlfriend warmly. They enabled writing my PhD and additionally suffused it with life.

## Scientific Visibility

### Publications

S. Kayser, K. Böttcher and A. Lüdge: Computational Simulations of the Lateral-Photovoltage-Scanning-Method, *IOP Conference Series: Materials Science and Engineering*, 355 (1), (2018)

C. Ehlers, S. Kayser, D. Uebel, R. Bansen, T. Markurt, T. Teubner, K. Hinrichs, O. Ernst and T. Boeck, :In situ removal of a native oxide layer from an amorphous silicon surface with a UV laser for subsequent layer growth *CrystEngCom*, 44, (2018)

W. Miller, N. Abrosimov, J. Fischer, A. Gybin, U. Juda, S. Kayser and J. Janicsko-Csathy: Quasi-Transient Calculation of Czochralski Growth of Ge Crystals Using the Software Elmer, *Crystals*, **10** (2020)

N. Abrosimov, M. Czupalla, N. Dropka, J. Fischer, A. Gybin, K. Irscher, J. Janicsko-Csathy, U. Juda, S. Kayser, W. Miller, M. Pietsch, F. Kießling: Technology development of high purity germanium crystals for radiation detectors, *Journal of Crystal Growth*, **532**, (2020)

### Preprints

O. Ernst, D. Uebel, S. Kayser, F. Lange, T. Teubner and T. Boeck, :Revealing all states of dewetting of a thin gold layer on a silicon surface by nanosecond laser conditioning, *Applied Surface Science Advanced*, (2020)

D. Uebel, S. Kayser, T. Markurt O. Ernst and T. Boeck: Fast Raman mapping and in situ TEM observation of metal induced crystallization of amorphous silico,n *CrystEngCom*, (2020)

### Talks

Occasion	Title	Date
WIAS Seminar	Modelling of Lateral-Photovoltage-Scanning Method	16 November 2016
MMP 2017	Computational Simulations of the Lateral-Photovoltage-Scanning - Method	20-22 September 2017
DGKK AK 2017	Investigation of the local resolution of the LPS method with respect to the doping concentration using Finite-Volume-Simulation	11-12 October 2017
GACCG 2018	Measurement of the local resolution of the Lateral-Photovoltage scanning and scanning photoluminescence method	14-16 February 2018

### Posters

Occasion	Title	Date
ICDS 2015	Novel study of lateral photovoltage scanning (LPS) and scanning photoluminescence (SPL) method	27-31 July 2015
GCCCCG 2016	Calculation of the heating treatment during Lateral-Photovoltage scanning and scanning photoluminescence measurements	16-18 March 2016
GSCCG 2017	First complete computational simulation of an LPS (Lateral - Photovoltage - Scanning) measurement setup	7-10 March 2017



## Bibliography

- [AA91] T. J. Anderson and I. Ansara. The Ga-In (Gallium-Indium) System. *Journal of Phase Equilibria*, 12(1):64–72, 1991.
- [ACC<sup>+</sup>06] M. D. Abbott, J. E. Cotter, F. W. Chen, T. Trupke, R. A. Bardos, and K. C. Fisher. Application of photoluminescence characterization to the development and manufacturing of high-efficiency silicon solar cells. *Journal of Applied Physics*, 100(11), 2006.
- [ADLK01] P. R. Amestoy, I. S. Duff, J. Y. L'Excellent, and Jacko Koster. A Fully Asynchronous Multifrontal Solver Using Distributed Dynamic Scheduling. *SIAM Journal on Matrix Analysis and Applications*, 23(1):15–41, 2001.
- [AGLP06] Patrick R. Amestoy, Abdou Guermouche, Jean-Yves L'Excellent, and Stéphane Pralet. Hybrid scheduling for the parallel solution of linear systems. *Parallel Computing*, 32(2):136–156, 2006.
- [AHR82] Narain D. Arora, John R. Hauser, and David J. Roulston. Electron and Hole Mobilities in Silicon as a Function of Concentration and Temperature. *IEEE Transactions on Electron Devices*, 29(2):292–295, 1982.
- [ALR<sup>+</sup>05] N.V. Abrosimov, A. Lüdge, H. Riemann, V.N. Kurlov, D. Borissova, V. Klemm, H. Halloin, P. von Ballmoos, P. Bastie, B. Hamelin, and R.K. Smither. Growth and properties of mosaic single crystals for X-ray lens application. *Journal of Crystal Growth*, 275(1-2):495–500, feb 2005.
- [ALRS02] N.V. Abrosimov, Anke Lüdge, Helge Riemann, and W Schröder. Lateral photovoltage scanning ( LPS ) method for the visualization of the solid-liquid interface of Si<sub>(1-x)</sub> - Ge<sub>(x)</sub> single crystals. 239:356–360, 2002.
- [BBC<sup>+</sup>13] E. Bonera, M. Bollani, D. Chrastina, F. Pezzoli, A. Picco, O. G. Schmidt, and D. Terziotti. Substrate strain manipulation by nanostructure perimeter forces. *Journal of Applied Physics*, 113(16), 2013.
- [BDS<sup>+</sup>91] V. N. Bhoraskar, S. D. Dhole, Surjit Singh, S. M. Jahagirdar, and K. S. Srinivas. Radiation damage and minority carrier lifetime in crystalline silicon. *Nuclear Inst. and Methods in Physics Research, B*, 62(1):99–102, 1991.
- [BGW18] Michele Baldini, Zbigniew Galazka, and Günter Wagner. Recent progress in the growth of  $\beta$ -Ga<sub>2</sub>O<sub>3</sub> for power electronics applications. *Materials Science in Semiconductor Processing*, 78(October 2017):132–146, 2018.
- [BKO<sup>+</sup>17] Shuyu Bao, Daeik Kim, Chibuzo Onwukaeme, Shashank Gupta, Krishna Saraswat, Kwang Hong Lee, Yeji Kim, Dabin Min, Yongduck Jung, Haodong Qiu, Hong Wang, Eugene A. Fitzgerald, Chuan Seng Tan, and Donguk Nam. Low-threshold optically pumped lasing in highly strained germanium nanowires. *Nature Communications*, 8(1):1–7, 2017.
- [BM16] Christopher Baber and Richard McMaster. The C challenges of I nteroperability. *Grasping the Moment*, pages 167–179, 2016.

- [BPRA10] P. Becker, H. J. Pohl, H. Riemann, and N. Abrosimov. Enrichment of silicon for a better kilogram. *Physica Status Solidi (A) Applications and Materials Science*, 207(1):49–66, 2010.
- [CACP<sup>+</sup>12] Rodolfo E. Camacho-Aguilera, Yan Cai, Neil Patel, Jonathan T. Bessette, Marco Romagnoli, Lionel C. Kimerling, and Jurgen Michel. An electrically pumped germanium laser. *Optics Express*, 20(10):11316, 2012.
- [CC92] Calvin Yi-ping Chao and Shun Lien Chuang. Spin-orbit-coupling effects on the valence-band structure of strained semiconductor quantum wells. *PHYSICAL REVIEW B*, 46(7):4110–4122, 1992.
- [CDB<sup>+</sup>10] G. Capellini, M. De Seta, Y. Busby, M. Pea, F. Evangelisti, G. Nicotra, C. Spinella, M. Nardone, and C. Ferrari. Strain relaxation in high Ge content SiGe layers deposited on Si. *Journal of Applied Physics*, 107(6), 2010.
- [CKY<sup>+</sup>13] G. Capellini, G. Kozlowski, Y. Yamamoto, M. Lisker, C. Wenger, G. Niu, P. Zaumseil, B. Tillack, A. Ghrib, M. De Kersauson, M. El Kurdi, P. Boucaud, and T. Schroeder. Strain analysis in SiN/Ge microstructures obtained via Si-complementary metal oxide semiconductor compatible approach. *Journal of Applied Physics*, 113(1), 2013.
- [CNF<sup>+</sup>85] K. Cho, M. Numan, T. G. Finstad, W. K. Chu, J. Liu, and J. J. Wortman. Transient enhanced diffusion during rapid thermal annealing of boron implanted silicon. *Applied Physics Letters*, 47(12):1321–1323, 1985.
- [CO98] M Costa and A Oliva. Numerical Simulation of a Latent Heat Thermal Energy Storage System With. *Interface*, 39(3):319–330, 1998.
- [Com13] Comsol. COMSOL Multiphysics 4.4 Heat Transfer Module User’s Guide. 2013.
- [CWDW08] Ryan C. Chiechi, Emily A. Weiss, Michael D. Dickey, and George M. Whitesides. Eutectic gallium-indium (EGaIn): A moldable liquid metal for electrical characterization of self-assembled monolayers. *Angewandte Chemie - International Edition*, 47(1):142–144, 2008.
- [CYD<sup>+</sup>09] Bryan Cord, Joel Yang, Huigao Duan, David C. Joy, Joseph Klingfus, and Karl K. Berggren. Limiting factors in sub- 10 nm scanning-electron-beam lithography. *Journal of Vacuum Science and Technology B: Microelectronics and Nanometer Structures*, 27(6):2616–2621, 2009.
- [Czo18] J. Czochralski. Ein neues Verfahren zur Messung der Kristallisationsgeschwindigkeit der Metalle. *Z. phys. Chemie.*, 92:219–221, 1918.
- [Das59] William C. Dash. Growth of Silicon Crystals Free from Dislocations. *Journal of Applied Physics*, 30(4):459–474, 1959.
- [DBSR17] K. Dadzis, P. Bönisch, L. Sylla, and T. Richter. Validation, verification, and benchmarking of crystal growth simulations. *Journal of Crystal Growth*, 474(December 2016):171–177, 2017.
- [DFR13] Natasha Dropka and Christiane Frank-Rotsch. Accelerated VGF-crystal growth of GaAs under traveling magnetic fields. *Journal of Crystal Growth*, 367:1–7, 2013.

- [DHM<sup>+</sup>06] Gordon Davies, Shusaku Hayama, Leonid Murin, Reinhard Krause-Rehberg, Vladimir Bondarenko, Asmita Sengupta, Cinzia Davia, and Anna Karpenko. Radiation damage in silicon exposed to high-energy protons. *Physical Review B - Condensed Matter and Materials Physics*, 73(16):1–10, 2006.
- [Dic66] D. H. Dickey. A Spreading Resistance Technique for Resistivity Measurements on Silicon. *Journal of the Electrochemical Society*, 113(3):255–259, 1966.
- [DL81] J. M. Dorkel and Ph. Leturcq. Carrier mobilities in silicon semi-empirically related to temperature, doping and injection level. *Solid State Electronics*, 24(9):821–825, 1981.
- [DMZ<sup>+</sup>17] Kaspars Dadzis, Robert Menzel, Mario Ziem, Till Turschner, Helge Riemann, and Nikolay Abrosimov. High-frequency Heat Induction Modeling for a Novel Silicon Crystal Growth Method. pages 1–6, 2017.
- [DNH<sup>+</sup>14] Sune Duun, Anne Nielsen, Christian Hindrichsen, Theis Sveigaard, Ole Andersen, Jarosław Jabłoński, and Leif Jensen. 200 mm <100> PREFERRED FLOAT ZONE ( PFZ ) SILICON WAFERS. 2014.
- [DS77] J Dziewior and W Schmid. Auger coefficients for highly doped and highly excited silicon. *Applied Physics Letters*, 31:346–348, 1977.
- [Fle57] N. H. Fletcher. The High Current Limit for Semiconductor Junction Devices. *Proceedings of the IRE*, pages 862–872, 1957.
- [Fre04] W Frensley. Scharfetter-Gummel Discretization Scheme for Drift-Diffusion Equations, 2004. *Preprint*, (3):1–3, 2004.
- [Gie14] Johannes Giesecke. *Quantitative Recombination and Transport Properties in Silicon from Dynamic Luminescence*. 2014.
- [GSM72] W. Gerlach, H. Schlangenotto, and H. Maeder. On the radiative recombination rate in silicon. *Physica Status Solidi (a)*, 13(1):277–283, 1972.
- [HJ18] Masataka Higashiwaki and Gregg H. Jessen. Guest Editorial: The dawn of gallium oxide microelectronics. *Applied Physics Letters*, 112(6), 2018.
- [Hop07] M Hopcroft. What is the Young ’ s Modulus of Silicon ? What is the Crystal Orientation in a Silicon Wafer ? *Physical Acoustics*, 19(2):229–238, 2007.
- [HWK<sup>+</sup>18] Martin Herms, Matthias Wagner, Stefan Kayser, Frank M. Kießling, Anna Poklad, Ming Zhao, and Ulrich Kretzer. Defect-induced Stress Imaging in Single and Multi-crystalline Semiconductor Materials. *Materials Today: Proceedings*, 5(6):14748–14756, 2018.
- [ITR15] ITRS. International Technology Roadmap for Semiconductors 2.0: Executive Report. *International technology roadmap for semiconductors*, page 79, 2015.
- [JHAP95] S. C. Jain, A. H. Harker, A. Atkinson, and K. Pinardi. Edge-induced stress and strain in stripe films and substrates: A two-dimensional finite element calculation. *Journal of Applied Physics*, 78(3):1630–1637, 1995.

- [KEWH89] Koichi Kakimoto, Minoru Eguchi, Hisao Watanabe, and Taketoshi Hibiya. Natural and forced convection of molten silicon during Czochralski single crystal growth. *Journal of Crystal Growth*, 94(2):412–420, 1989.
- [KL54] W Kohn and J.M. Luttinger. Motion of Electrons and Holes in Perturbed Periodic Fields. *Physical Review*, 97(4):869–883, 1954.
- [KLB18] S. Kayser, A. Lüdge, and K. Böttcher. Computational Simulations of the Lateral-Photovoltage-Scanning-Method. *IOP Conference Series: Materials Science and Engineering*, 355(1), 2018.
- [KNL<sup>+</sup>91] Koichi Kakimoto, Pierre Nicodème, Michael Lecomte, François Dupret, and Marcel J. Crochet. Numerical simulation of molten silicon flow; comparison with experiment. *Journal of Crystal Growth*, 114(4):715–725, 1991.
- [LK11] Zheng Lu and Steven Kimbel. Growth of 450 mm diameter semiconductor grade silicon crystals. *Journal of Crystal Growth*, 318(1):193–195, 2011.
- [Lor19] Nicolai Lorenz. *Lumped Parameter Model for Silicon Crystal Growth from Granulate Crucible*. PhD thesis, Technische Universität Berlin, 2019.
- [LR97] Anke Lüdge and Helge Riemann. Doping Inhomogeneities in Silicon Crystals Detected by the Lateral Photovoltage Scanning (LPS) Method. *Inst. Phys. Conf. Ser.*, 160:145–148, 1997.
- [LSP<sup>+</sup>07] Jifeng Liu, Xiaochen Sun, Dong Pan, Xiaoxin Wang, Lionel C. Kimerling, Thomas L. Koch, and Jurgen Michel. Tensile-strained, n-type Ge as a gain medium for monolithic laser integration on Si. *Optics Express*, 15(18):11272, 2007.
- [Lut56] J M Luttinger. Quantum Theory of Cyclotron Resonance in Semiconductors: General Theory. *Physical Review*, 529(1954), 1956.
- [Mad07] Imdat Maden. *Numerische Simulation der physikalischen Eigenschaften eines planaren 3D Germanium Pixeldetektors*. PhD thesis, Darmstadt, 2007.
- [MD66] R. G. Mazur and D. H. Dickey. A Spreading Resistance Technique for Resistivity Measurements on Silicon. *Journal of The Electrochemical Society*, 113(3):255–259, 1966.
- [Mil10] David A.B. Miller. Device requirements for optical interconnects to CMOS silicon chips. *Optics InfoBase Conference Papers*, 97(7), 2010.
- [Moo65] G E Moore. Craming more components onto integrated circuits. *Electronics*, 38(8):114–117, 1965.
- [MPB15] Costanza Lucia Manganelli, Paolo Pintus, and Claudio Bonati. Modeling of strain-induced Pockels effect in Silicon. 23(22):25324–25332, 2015.
- [New00] R. C. Newman. Oxygen diffusion and precipitation in Czochralski silicon. *Journal of Physics Condensed Matter*, 12(25), 2000.

- [OM60] J. Oroshnik and A. Many. Quantitative photovoltaic evaluation of the resistivity homogeneity of germanium single crystals. *Solid State Electronics*, 1(1):46–53, 1960.
- [OMTO92] Tetsuo Oikawa, Nobufumi Mori, Noriko Takano, and Masahiro Ohnishi. Development of an image recording system using the imaging plate in a TEM. *Fuji Film research & development*, 443(37):74–80, 1992.
- [Oss19] Ossila. FOUR-POINT PROBE USER MANUAL 3.0c. page 11, 2019.
- [PDLV<sup>+</sup>99] M. C. Porté-Durrieu, C. Labrugère, F. Villars, F. Lefebvre, S. Dutoya, A. Guette, L. Bordenave, and C. Baquey. Development of RGD peptides grafted onto silica surfaces: XPS characterization and human endothelial cell interactions. *Journal of Biomedical Materials Research*, 46(3):368–375, 1999.
- [Pfa52] W. G. Pfann. Principles Zone-Melting. pages 747–753, 1952.
- [PS72] D. Pierce and W. Spicer. Electronic Structure of Amorphous Si from Photoemission and Optical Studies. *Physical Review B*, 5(8):3017–3029, 1972.
- [PTG<sup>+</sup>15] D. Peschka, M. Thomas, A. Glitzky, R. Nurnberg, K. Gartner, M. Virgilio, S. Guha, T. Schroeder, G. Capellini, and T. Koprucki. Modeling of edge-emitting lasers based on tensile strained germanium microstrips. *IEEE Photonics Journal*, 7(3):2013, 2015.
- [RC19] Rs-Components. Data Sheet - Raspberry Pi Model B. *Raspberry Pi (Trading) Ltd.*, 2019.
- [Rei17] Felix Reichmann. *Size-Dependent Investigation of Selectively Grown  $\beta$ -Sn Nanostructures with Respect to Plasmonic Activity*. PhD thesis, Brandenburgischen Technischen Universität Cottbus-Senftenberg, 2017.
- [RNM<sup>+</sup>17] Fiacre E. Rougieux, Hieu T. Nguyen, D. H. Macdonald, Bernhard Mitchell, and Robert Falster. Growth of Oxygen Precipitates and Dislocations in Czochralski Silicon. *IEEE Journal of Photovoltaics*, 7(3):735–740, 2017.
- [SB02] Sriram Sundararajan and Bharat Bhushan. Development of AFM-based techniques to measure mechanical properties of nanoscale structures. *Sensors and Actuators, A: Physical*, 101(3):338–351, 2002.
- [SDML10] V. A. Shah, A. Dobbie, M. Myronov, and D. R. Leadley. Reverse graded SiGe/Ge/Si buffers for high-composition virtual substrates. *Journal of Applied Physics*, 107(6), 2010.
- [SG69] D. L. Scharfetter and H. K. Gummel. Large-Signal Analysis of a Silicon Read Diode Oscillator. *IEEE Transactions on Electron Devices*, ED-16:64–77, 1969.
- [SG89] N. B. Singh and M. E. Glicksman. Determination of the mean solid-liquid interface energy of pivalic acid. *Journal of Crystal Growth*, 98(4):573–580, 1989.
- [Shi86] Fumio Shimura. Carbon enhancement effect on oxygen precipitation in Czochralski silicon. *Journal of Applied Physics*, 59(9):3251–3254, 1986.

- [SK69] M. Sze, Simon and K. Ng Kwok. *Physics of Semiconductor Devices*. John Wiley & Sons, 3 edition, 1969.
- [SLR96] H.-J. Schulze, A. Lüdge, and H. Riemann. High-Resolution Measurement of Resistivity Variations in Power Devices by the Photoscanning Method. *J. Electrochem. Soc.*, 143:4105–4108, 1996.
- [Sor06] Richard Soref. The past, present, and future of silicon photonics. *IEEE Journal on Selected Topics in Quantum Electronics*, 12(6):1678–1687, 2006.
- [Sor10] Richard Soref. Mid-infrared photonics in silicon and germanium. *Nature Photonics*, 4(8):495–497, 2010.
- [SPZ07] Andrew J. Steckl, Jeong Ho Park, and John M. Zavada. Prospects for rare earth doped GaN lasers on Si, 2007.
- [STY<sup>+</sup>13] Jie Sun, Erman Timurdogan, Ami Yaacobi, Ehsan Shah Hosseini, and Michael R. Watts. Large-scale nanophotonic phased array. *Nature*, 493(7431):195–199, 2013.
- [Syl62] W. D. Sylwestrowicz. Mechanical properties of single crystals of silicon. *Philosophical Magazine*, 7(83):1825–1845, 1962.
- [Tai00] King L Tai. System-In-Package ( SIP ): Challenges and Opportunities. *Proceedings 2000. Design Automation Conference. (IEEE Cat. No.00CH37106)*, pages 191–196, 2000.
- [Tau55] J. Tauc. The Theory of a Bulk Photo-Voltaic Phenomenon in Semi-Conductors. *Institute of technical Physics, Czechosl.*, 5:178–191, 1955.
- [The62] H C Theurer. METHOD OF PROCESSENG SEMCONDUCTIVE MATERIALS, 1962.
- [Tib19] Shara Tibken. CES 2019: Moore’s Law is dead, says Nvidia’s CEO. <https://www.cnet.com/news/moores-law-is-dead-nvidias-ceo-jensen-huang-says-at-ces-2019/>, 2019.
- [Toc10] G Tocci. Performance estimation and Variability from Random Dopant Fluctuations in Multi-Gate Field Effect Transistors: a Simulation Study. 2010.
- [TUT92] H Takeno, S. Ushio, and T. Takenaka. Evaluation of Microdefects in as-grown Silicon Crystals. *Mat. Res. Soc. Symp. Proc.*, 262:51–56, 1992.
- [Val54] L.B. Valdes. Resistivity Measurements on Germanium for Transistor. *Proceeding of the I.R.E.*, 42(2):420–427, 1954.
- [Van50] W. Van Roosbroeck. Theory of the Flow of Electrons and Holes in Germanium and Other Semiconductors. *Bell System Technical Journal*, 29(4):560–607, 1950.
- [Van53] W. Van Roosbroeck. The Transport of Added Currents Carriers in a Homogeneous Semiconductor. *Physical Review*, 91(2), 1953.
- [Van86] Chris G. Van de Walle. Theoretical calculations of semiconductor heterojunction discontinuities. *Journal of Vacuum Science & Technology B: Microelectronics and Nanometer Structures*, 4(4):1055, 1986.

- [Van89] Chris G. Van de Walle. Band lineups and deformation potentials in the model-solid theory. *PHYSICAL REVIEW B*, 39(3):1871–1883, 1989.
- [Var67] Y. P. Varshni. Temperature dependence of the energy gap in semiconductors. *Physica*, 34(1):149–154, 1967.
- [VFM07] D. Vizman, J. Friedrich, and G. Mueller. 3D time-dependent numerical study of the influence of the melt flow on the interface shape in a silicon ingot casting process. *Journal of Crystal Growth*, 303(1 SPEC. ISS.):231–235, 2007.
- [VMG<sup>+</sup>13] M. Virgilio, C. L. Manganelli, G. Grosso, G. Pizzi, and G. Capellini. Radiative recombination and optical gain spectra in biaxially strained n-type germanium. *Physical Review B - Condensed Matter and Materials Physics*, 87(23):1–11, 2013.
- [VN19] Benjamin Venitucci and Yann Michel Niquet. Simple model for electrical hole spin manipulation in semiconductor quantum dots: Impact of dot material and orientation. *Physical Review B*, 99(11), 2019.
- [WLC<sup>+</sup>17] Shien Yang Wu, C. Y. Lin, M. C. Chiang, J. J. Liaw, J. Y. Cheng, S. H. Yang, C. H. Tsai, P. N. Chen, T. Miyashita, C. H. Chang, V. S. Chang, K. H. Pan, J. H. Chen, Y. S. Mor, K. T. Lai, C. S. Liang, H. F. Chen, S. Y. Chang, C. J. Lin, C. H. Hsieh, R. F. Tsui, C. H. Yao, C. C. Chen, R. Chen, C. H. Lee, H. J. Lin, C. W. Chang, K. W. Chen, M. H. Tsai, K. S. Chen, Y. Ku, and S. M. Jang. A 7nm CMOS platform technology featuring 4 th generation FinFET transistors with a 0.027um 2 high density 6-T SRAM cell for mobile SoC applications. *Technical Digest - International Electron Devices Meeting, IEDM*, pages 2.6.1–2.6.4, 2017.
- [Zul94] W. Zulehner. The growth of highly pure silicon crystals. *Metrologia*, 31(3):255–261, 1994.
- [Zul01] Werner Zulehner. Influence of structure development on atomic layer deposition of TiO<sub>2</sub> thin films. *Applied Surface Science*, 181(3-4):339–348, 2001.
- [ZYM15] Zhiping Zhou, Bing Yin, and Jurgen Michel. On-chip light sources for silicon photonics. *Light: Science and Applications*, 4(11):1–13, 2015.





# Appendices

# Appendix A

## Notes to the main text

### Derivation of Equation (2.14)

In Section 1.2 when discussing the Tauc theory of the bulk photovoltaic effect, we stated that if excess carriers are present only in the  $\overline{bc}$  interval, contributions to the photovoltage from the closed circuit integrals in the right hand side of Eq. (2.7), can be recast to restrict the integration domain inside the  $\overline{bc}$  range only. To demonstrate this statement, we write  $U$  in our close 1D ring geometry as

$$U = \oint E dx = \int_a^b E dx + \underbrace{\int_b^c dx}_{\text{excited}} + \int_c^{a'} E dx \quad (\text{A.1})$$

where we have evidenced the contribution from the excited region. From the above equation, adding and subtracting a contribution from a non-excited  $\overline{bc}$  region, follows

$$\begin{aligned} U &= \int_a^b E dx + \underbrace{\int_b^c E dx}_{\text{excited}} + \int_c^{a'} E dx + \int_b^c E dx - \int_b^c E dx \\ &= \oint E dx + \underbrace{\int_b^c E dx}_{\text{excited}} - \int_b^c E dx \end{aligned} \quad (\text{A.2})$$

Therefore since the first term in the right hand side vanishes, the photoexcited voltage can be calculated considering only the  $\overline{bc}$  interval, provided that the contribution in this range to the potential associated to equilibrium condition is also considered.

We now focus on an  $n$ -type system ( $n_{\text{eq}} \gg p_{\text{eq}}$ ), and introduce the approximate expression for the spatially varying equilibrium conductivity  $\sigma_{\text{eq}} = \sigma_0 + \zeta x$ , which is supposed to hold in the  $\overline{bc}$  interval. Exploiting Eq. (A.2), and relying on Eq.(2.14) we obtain

$$U = -\frac{k_B T}{q} \left( \underbrace{\int_b^c \frac{\zeta}{\sigma_0 + \zeta x + \Delta\sigma} dx}_{f_1} - \underbrace{\int_b^c \frac{\zeta}{\sigma_0 + \zeta x} dx}_{f_2} - \frac{\mu_p - \mu_n}{\mu_p + \mu_n} \oint \frac{\nabla_x \Delta\sigma}{\sigma_{\text{eq}} + \Delta\sigma} dx \right) \quad (\text{A.3})$$

where we have named  $f_1$  the  $\overline{bc}$  contribution where the linearized expression for the conductivity

holds, and  $\oint_2$  the term involving a closed circuit integral. We first address the evaluation of  $\int_1$ :

$$\begin{aligned}\int_1 &= \int_b^c \frac{\zeta}{\sigma_0 + \zeta x + \Delta\sigma} dx - \int_b^c \frac{\zeta}{\sigma_0 + \zeta x} dx \\ &= \ln[\sigma_0 + \zeta x + \Delta\sigma]_b^c - \ln[\sigma_0 + \zeta x]_b^c \\ &= \ln\left[1 + \frac{\Delta\sigma}{\sigma_0 + \zeta c}\right] - \ln\left[1 + \frac{\Delta\sigma}{\sigma_0 + \zeta b}\right]\end{aligned}\quad (\text{A.4})$$

The integrand in  $\oint_2$  vanishes everywhere except for  $x = b$  and  $x = c$  where it diverges. Therefore, to calculate it is useful to adopt a limiting procedure, substituting the rectangular shape of  $\delta\sigma$  as a function of  $x$  with a symmetric trapezoidal profile, with the slope in  $x = b$  and  $x = c$  controlled by a  $\delta 0$  parameter:

$$\oint_2 = \lim_{\delta \rightarrow 0} \underbrace{\int_{b-\delta}^{b+\delta} \frac{\nabla_x \left(\frac{\Delta\sigma}{2\delta}x - \frac{\Delta\sigma}{2\delta}(b-\delta)\right)}{\sigma_0 + \zeta x + \frac{\Delta\sigma}{2\delta}x - \frac{\Delta\sigma}{2\delta}(b-\delta)} dx}_{\int_b} + \lim_{\delta \rightarrow 0} \underbrace{\int_{c-\delta}^{c+\delta} \frac{\nabla_x \left(-\frac{\Delta\sigma}{2\delta}x + \frac{\Delta\sigma}{2\delta}(c+\delta)\right)}{\sigma_0 + \zeta x - \frac{\Delta\sigma}{2\delta}x + \frac{\Delta\sigma}{2\delta}(c+\delta)} dx}_{\int_c}\quad (\text{A.5})$$

For  $\int_b$  it holds

$$\begin{aligned}\int_b &= \frac{\frac{\Delta\sigma}{2\delta}}{\frac{\Delta\sigma}{2\delta} + \zeta} \int_{b-\delta}^{b+\delta} \frac{\left(\frac{\Delta\sigma}{2\delta} + \zeta\right)}{\sigma_0 + \left(\frac{\Delta\sigma}{2\delta} + \zeta\right)x - \frac{\Delta\sigma}{2\delta}(b-\delta)} dx \\ &= \frac{1}{1 + \frac{2\zeta\delta}{\Delta\sigma}} \ln \left[ \sigma_0 + \left(\frac{\Delta\sigma}{2\delta} + \zeta\right)x - \frac{\Delta\sigma}{2\delta}(b-\delta) \right]_{b-\delta}^{b+\delta} = \frac{1}{1 + \frac{2\zeta\delta}{\Delta\sigma}} \ln \left[ \frac{\sigma_0 + \zeta(b+\delta) + \Delta\sigma}{\sigma_0 + \zeta(b+\delta)} \right]\end{aligned}\quad (\text{A.6})$$

Letting  $\delta \rightarrow 0$  we end up with

$$\lim_{\delta \rightarrow 0} \int_b \frac{1}{1 + \frac{2\zeta\delta}{\Delta\sigma}} \ln \left[ \frac{\sigma_0 + \zeta(b+\delta) + \Delta\sigma}{\sigma_0 + \zeta(b+\delta)} \right] = \ln \left[ 1 + \frac{\Delta\sigma}{\sigma_0 + \zeta b} \right]\quad (\text{A.7})$$

Analogously the  $\int_c$  gives

$$\lim_{\delta \rightarrow 0} \int_c = -\ln \left[ 1 + \frac{\Delta\sigma}{\sigma_0 + \zeta c} \right]\quad (\text{A.8})$$

In conclusion we have

$$U = -\frac{k_B T}{q} \frac{2}{\frac{\mu_n}{\mu_p} + 1} \ln \left[ \frac{1 + \frac{\Delta\sigma}{\sigma_0 + \zeta c}}{1 + \frac{\Delta\sigma}{\sigma_0 + \zeta b}} \right] = -\frac{k_B T}{q} \frac{2}{\frac{\mu_n}{\mu_p} + 1} \ln \left[ \frac{1 + \frac{\Delta\sigma}{\sigma(c)}}{1 + \frac{\Delta\sigma}{\sigma(b)}} \right]\quad (\text{A.9})$$

$$= -\frac{k_B T}{q} \frac{2}{\frac{\mu_n}{\mu_p} + 1} \left( \ln \left[ \frac{\sigma(c)}{\sigma(b)} \right] - \ln \left[ \frac{\sigma(c) + \Delta\sigma}{\sigma(b) + \Delta\sigma} \right] \right).\quad (\text{A.10})$$

which is the same as Eq. (2.25) reported in Chapter 2.

## Analytic expressions for LH,HH and SO band

HH and LH band:

$$Part1 = Part1(HH) = Part1(LH) = Part1(SO) = P_{\epsilon} + SO/3 \quad (A.11)$$

$$\begin{aligned} Part2(HH) = Part2(LH) = & (((3P_{\epsilon}Q_{\epsilon}^2)/2 + (3P_{\epsilon}R_{\epsilon}^2)/2 - (P_{\epsilon}^2SO)/2 + (3P_{\epsilon}S_{\epsilon}^2)/2 - 3Q_{\epsilon}R_{\epsilon}^2 \\ & + (Q_{\epsilon}^2SO)/2 + (3Q_{\epsilon}S_{\epsilon}^2)/2 + (R_{\epsilon}^2SO)/2 + (SOS_{\epsilon}^2)/2 - ((3P_{\epsilon} + SO)(3Q_{\epsilon}^2 - 2SOP_{\epsilon} \\ & - 3P_{\epsilon}^2 + 3R_{\epsilon}^2 + 3S_{\epsilon}^2))/6 - P_{\epsilon}^3/2 + Q_{\epsilon}^3 - (3P_{\epsilon} + SO)^3/27 + (3 * 3^{1/2}R_{\epsilon}S_{\epsilon}^2)/2)^2 \\ & - (Q_{\epsilon}^2 - P_{\epsilon}^2 - (2P_{\epsilon}SO)/3 + R_{\epsilon}^2 + S_{\epsilon}^2 + (3P_{\epsilon} + SO)^2/9)^3) \end{aligned} \quad (A.12)$$

$$\begin{aligned} Part5(HH) = Part5(LH) = & ((P_{\epsilon}^2SO)/2 - (3P_{\epsilon}R_{\epsilon}^2)/2 - (3P_{\epsilon}Q_{\epsilon}^2)/2 - (3P_{\epsilon}S_{\epsilon}^2)/2 + \\ & 3Q_{\epsilon}R_{\epsilon}^2 - (Q_{\epsilon}^2SO)/2 - (3Q_{\epsilon}S_{\epsilon}^2)/2 - (R_{\epsilon}^2SO)/2 - (SOS_{\epsilon}^2)/2 + \\ & ((3P_{\epsilon} + SO)(3Q_{\epsilon}^2 - 2SOP_{\epsilon} - 3P_{\epsilon}^2 + 3R_{\epsilon}^2 + 3S_{\epsilon}^2))/6 \\ & + P_{\epsilon}^3/2 - Q_{\epsilon}^3 + (3P_{\epsilon} + SO)^3/27 - (3 * 3^{1/2}R_{\epsilon}S_{\epsilon}^2)/2) \end{aligned} \quad (A.13)$$

$$A = A(HH) = A(LH) = A(SO) = (Q_{\epsilon}^2 - P_{\epsilon}^2 - (2P_{\epsilon}SO)/3 + R_{\epsilon}^2 + S_{\epsilon}^2 + (3P_{\epsilon} + SO)^2/9) \quad (A.14)$$

$$Part3(HH) = Part3(LH) = ((Part2(HH))^{1/2} + Part5(HH))^{1/3} \quad (A.15)$$

$$Part4(HH) = Part4(LH) = A/(2Part3(HH)) \quad (A.16)$$

$$E(HH) = Part1 - 0.5(Re(Part3(HH))) - R_{\epsilon}(Part4(HH)) + \sqrt{(3)Im(0.5Part3(HH) - Part4(HH))} \quad (A.17)$$

$$E(LH) = Part1 - 0.5(Re(Part3(HH))) - R_{\epsilon}(Part4(HH)) - \sqrt{(3)Im(0.5Part3(HH) - Part4(HH))}. \quad (A.18)$$

SO band:

$$Part1 = Part1(HH) = Part1(LH) = Part1(SO) = P_{\epsilon} + SO/3 \quad (A.19)$$

$$A = A(HH) = A(LH) = A(SO) = (Q_{\epsilon}^2 - P_{\epsilon}^2 - (2P_{\epsilon}SO)/3 + R_{\epsilon}^2 + S_{\epsilon}^2 + (3P_{\epsilon} + SO)^2/9) \quad (A.20)$$

$$\begin{aligned}
Part2(SO) = & (((3P_\epsilon Q_\epsilon^2)/2 + (3P_\epsilon R_\epsilon^2)/2 - (P_\epsilon^2 SO)/2 + (3P_\epsilon S_\epsilon^2)/2 - 3Q_\epsilon R_\epsilon^2 + (Q_\epsilon^2 SO)/2 \\
& + (3Q_\epsilon S_\epsilon^2)/2 + (R_\epsilon^2 SO)/2 + (SO S_\epsilon^2)/2 - ((3P_\epsilon + SO)(3P_\epsilon^2 \\
& - 2SOP_\epsilon + 3Q_\epsilon^2 + 3R_\epsilon^2 + 3S_\epsilon^2))/6 - \\
& P_\epsilon^3/2 + Q_\epsilon^3 - (3P_\epsilon + SO)^3/27 + (3 * 3^{1/2} R_\epsilon S_\epsilon^2)/2)^2 - \\
& (Q_\epsilon^2 - P_\epsilon^2 - (2P_\epsilon SO)/3 + R_\epsilon^2 + S_\epsilon^2 + (3P_\epsilon + SO)^2/9)^3)
\end{aligned} \tag{A.21}$$

$$\begin{aligned}
Part5(SO) = Part5(LH) = & ((P_\epsilon^2 SO)/2 - (3P_\epsilon R_\epsilon^2)/2 - (3P_\epsilon Q_\epsilon^2)/2 - (3P_\epsilon S_\epsilon^2)/2 + \\
& 3Q_\epsilon R_\epsilon^2 - (Q_\epsilon^2 SO)/2 - (3Q_\epsilon S_\epsilon^2)/2 - (R_\epsilon^2 SO)/2 - (SO S_\epsilon^2)/2 + \\
& ((3P_\epsilon + SO)(3P_\epsilon^2 - 2SOP_\epsilon + 3Q_\epsilon^2 + 3R_\epsilon^2 + 3S_\epsilon^2))/6 \\
& + P_\epsilon^3/2 - Q_\epsilon^3 + (3P_\epsilon + SO)^3/27 - (3 * 3^{1/2} R_\epsilon S_\epsilon^2)/2)
\end{aligned} \tag{A.22}$$

$$Part3(SO) = ((Part2(SO))^{1/2} + Part5(SO))^{1/3} \tag{A.23}$$

$$Part4(SO) = A/(Part3(SO)) \tag{A.24}$$

$$E(SO) = Re(Part1 + Part3(SO) + Part4(SO)). \tag{A.25}$$

# Appendix B

## Code

Presented is a simulation code used for the calculation of the local resolution of an LPS-measurement. Steady state solved for are the electric potential  $\Phi$  and the charge carrier densities  $n, p$ . The focal point is at a defined spot  $P_f(x_f, y_f)$ . Here usually a parametric sweep of the focal point can simulate a line scan. For the laser power and the dopant concentration an auxiliary sweep is used. The benefit is, that a solution containing a parameter set will be used as a configuration for the next parameter set. Just for illustration two laser powers and three main donor levels were chosen. After the simulation, the code was saved as a MATLAB file, which is shown below.

```
1 function out = model
2 %
3 % thesis.m
4 %
5 % Model exported on Sep 16 2019, 10:43 by COMSOL 5.4.0.246.
6
7 import com.comsol.model.*
8 import com.comsol.model.util.*
9
10 model = ModelUtil.create('Model');
11
12 model.modelPath('D:\Stefan\Desktop');
13
14 model.label('thesis.mph');
15
16 model.comments(['20160829 15uhr33 kboe FV Wafer 2p430mm sin ab 15\n\ngestoppt bei 0.6 sec, weil
17 randeffekt bis 0.8sec nicht wichtig']);
18
19 model.param.set('L', '9.000[mm]', '''Wafer length''');
20 model.param.set('B', '0.50[mm]', '''Wafer width''');
21 model.param.set('Lz', '0.05[mm]', '''Wafer thickness''');
22 model.param.set('x0', '0.0[mm]', '''path center x-coord''');
23 model.param.set('y0', '0[mm]', '''path center y-coord''');
24 model.param.set('d0', '5[um]');
25 model.param.set('z_off', '0[mm]');
26 model.param.set('Z_R', 'pi*d0^2/4/lambda00');
27 model.param.set('sigx', '1/4*d0*(1+(z_off/Z_R)^2)^(1/2)', '''pulse x standard dev''');
28 model.param.set('sigy', '1/4*d0*(1+(z_off/Z_R)^2)^(1/2)', '''pulse y standard dev''');
29 model.param.set('Bor0a', 'Bor0*1[cm^-3]', '''basic Bor-Doping''');
30 model.param.set('Bor0b', '0.05*Bor0a', '''Bor-Doping Gradient''');
31 model.param.set('DeltaBor', '0*0.3*Bor0a', '''Bor fluctuation''');
32 model.param.set('ni', '1e10[1/cm^3]', '''intrinsic''');
33 model.param.set('BorWaveLength', '500[um]');
34 model.param.set('x000002', '1');
35 model.param.set('x000003', '1');
36 model.param.set('WaveNo', '(L)/BorWaveLength');
37 model.param.set('sinusFaktor', 'WaveNo/L', '''for Bor-Doping-sinus''');
38 model.param.set('velo', '3[mm/s]');
39 model.param.set('time_end', '(L-sigy)/velo');
40 model.param.set('pulse', '0.0025[s]');
```

```

40 model.param.set('time_step', 'pulse/10', '''timestep''');
41 model.param.set('x000000', '1');
42 model.param.set('x000001', '1');
43 model.param.set('prefactor', '0');
44 model.param.set('P0', 'praefakt*1/1000*0.025[W]', '''total laser power, pulsed''');
45 model.param.set('Rc', '0.34', '''reflection''');
46 model.param.set('Ac', '1/4.7[um]', '''absorption coeff''');
47 model.param.set('lambda00', '685[nm]', '''wavelength of laser''');
48 model.param.set('f0', 'c_const/lambda00');
49 model.param.set('omega0', '2*pi*1[rad]*f0');
50 model.param.set('E_ph', 'f0*h_const', '''photon energy''');
51 model.param.set('cp', '1');
52 model.param.set('Pdens', 'P0', '''areal density of power''');
53 model.param.set('Phi', 'Pdens/E_ph', '''photon flux''');
54 model.param.set('a', '(pi*sigx*sigy)/4');
55 model.param.set('Phi2', 'Phi', '''Rate at focus area''');
56 model.param.set('praefakt', '500', '''sweep parameter''');
57 model.param.set('time_end2', 'time_end*1[1/s]', '''endzeit ohne einheit''');
58 model.param.set('y_end2', '(0.015[mm]+velo*time_end)*1[1/mm]', '''endort ohne einheit''');
59 model.param.set('gauss_dia', [ '280[ native2unicode(hex2dec({'00' 'b5'}), 'unicode') 'm]'], [ '
  'St' native2unicode(hex2dec({'00' 'f6'}), 'unicode') 'rstelle''']);
60 model.param.set('x2', '0[mm]', [ '''Ort St' native2unicode(hex2dec({'00' 'f6'}), 'unicode') '
  rstelle''']);
61 model.param.set('y2', '4.5 [nm]', [ '''Ort St' native2unicode(hex2dec({'00' 'f6'}), 'unicode') '
  rstelle''']);
62 model.param.set('Size_max', 'L/WaveNo/150*1.9*2');
63 model.param.set('Size_min', 'L/WaveNo/170*1.9*2');
64 model.param.set('k_B', '1.3806*10^-23[J/K]');
65 model.param.set('q', '1.602*10^-19[A*s]');
66 model.param.set('RT', '293.15[K]');
67 model.param.set('geschw', 'velo');
68 model.param.set('tschritt', '1.5[s]');
69 model.param.set('y02', 'velo*tschritt');
70 model.param.set('x02', '0[m]');
71 model.param.set('Se', '3*100000[cm/s]');
72 model.param.set('Sh', '3*100000[cm/s]');
73 model.param.set('tau_SRH', '900[us]');
74 model.param.set('Geom', '0.016');
75 model.param.set('pen', '2[um]');
76 model.param.set('z1', '6.6E-7[m]');
77 model.param.set('z2', '6.3E-7[m]');
78 model.param.set('z3', '5E-7[m]');
79 model.param.set('s11', '7E-8 [m]');
80 model.param.set('s12', '1.4E-7[m]');
81 model.param.set('s13', '1.9E-7[m]');
82 model.param.set('Bor0', '6.5E13');
83 model.param.set('SRH2', '400');
84 model.param.label('Parameters 1');
85
86 model.component.create('mod1', false);
87
88 model.component('mod1').geom.create('geom1', 3);
89
90 model.component('mod1').label('Model 1');
91
92 model.component('mod1').defineLocalCoord(false);
93
94 model.func.create('an1', 'Analytic');
95 model.func.create('an2', 'Analytic');
96 model.component('mod1').func.create('int1', 'Interpolation');
97 model.component('mod1').func.create('int2', 'Interpolation');
98 model.func.create('pw1', 'Piecewise');
99 model.func.create('an4', 'Analytic');
100 model.func.create('an5', 'Analytic');
101 model.func.create('an6', 'Analytic');
102 model.func.create('an7', 'Analytic');
103 model.component('mod1').func.create('int3', 'Interpolation');
104 model.func.create('an8', 'Analytic');
105 model.func.create('an9', 'Analytic');
106 model.func.create('an10', 'Analytic');
107 model.component('mod1').func.create('an12', 'Analytic');
108 model.component('mod1').func.create('step1', 'Step');
109 model.func.create('wv1', 'Wave');
110 model.func.create('wv2', 'Wave');

```

```

111 model.func.create('rect1', 'Rectangle');
112 model.component('mod1').func.create('an13', 'Analytic');
113 model.func.create('an14', 'Analytic');
114 model.func('an1').label('Doping-sinus-profile');
115 model.func('an1').set('expr', 'sin(sinusFaktor*2*pi*(y[m]-0.000015[m]))');
116 model.func('an1').set('args', {'y'});
117 model.func('an1').set('argunit', 'm');
118 model.func('an1').set('fununit', '1');
119 model.func('an1').set('plotargs', {'y' '0.0006' '0.001425'});
120 model.func('an2').label('Analytic 2');
121 model.func('an2').set('funcname', 'focus');
122 model.func('an2').set('expr', 'exp(-((a-a0)^2/(2*sigma^2))-((b-b0)^2/(2*sigma^2)))');
123 model.func('an2').set('args', {'a' 'a0' 'sigma' 'b' 'b0' 'sigma'});
124 model.func('an2').set('argunit', 'm,m,m,m,m');
125 model.func('an2').set('fununit', '1');
126 model.func('an2').set('plotargs', {'a' '0' 'B'; ...
127 'a0' '0' '0'; ...
128 'sigma' '2.5[um]' '2.5[um]'; ...
129 'b' '-L/2' 'L/2'; ...
130 'b0' '0' '0'; ...
131 'sigma' '2.5[um]' '2.5[um]'});
132 model.component('mod1').func('int1').label('x-Koord-Zeitlauf');
133 model.component('mod1').func('int1').set('table', {'0.000000' '0.000000'; ...
134 '1.600000' '0.000000'});
135 model.component('mod1').func('int1').set('argunit', 's');
136 model.component('mod1').func('int1').set('fununit', 'mm');
137 model.component('mod1').func('int2').label('y-Koord-Zeitlauf');
138 model.component('mod1').func('int2').set('table', {'0' '0.015'; 'time_end2' 'y_end2'});
139 model.component('mod1').func('int2').set('argunit', 's');
140 model.component('mod1').func('int2').set('fununit', 'mm');
141 model.func('pw1').label('Piecewise 1');
142 model.func('pw1').set('smooth', 'contd2');
143 model.func('pw1').set('smoothends', true);
144 model.func('pw1').set('pieces', {'0' '0.8' '1'});
145 model.func('pw1').set('argunit', 's,s');
146 model.func('pw1').set('fununit', '1');
147 model.func('an4').label('Doping-sinus-profile 1');
148 model.func('an4').set('expr', 'sin(sinusFaktor/2*2*pi*(y[m]-0.000015[m]))');
149 model.func('an4').set('args', {'y'});
150 model.func('an4').set('argunit', 'm');
151 model.func('an4').set('fununit', '1');
152 model.func('an4').set('plotargs', {'y' '0.0006' '0.001425'});
153 model.func('an5').label('Doping-sinus-profile 1.1');
154 model.func('an5').set('expr', 'sin(sinusFaktor/1.5*2*pi*(y[m]-0.000015[m]))');
155 model.func('an5').set('args', {'y'});
156 model.func('an5').set('argunit', 'm');
157 model.func('an5').set('fununit', '1');
158 model.func('an5').set('plotargs', {'y' '0.0006' '0.001425'});
159 model.func('an6').label('Doping-sinus-profile 1.1.1');
160 model.func('an6').set('expr', 'sin(sinusFaktor/3*2*pi*(y[m]-0.000015[m]))');
161 model.func('an6').set('args', {'y'});
162 model.func('an6').set('argunit', 'm');
163 model.func('an6').set('fununit', '1');
164 model.func('an6').set('plotargs', {'y' '0.0006' '0.001425'});
165 model.func('an7').label('Doping-sinus-profile 1.1.1.1');
166 model.func('an7').set('expr', 'sin(sinusFaktor/1.7*2*pi*(y[m]-0.000015[m]))');
167 model.func('an7').set('args', {'y'});
168 model.func('an7').set('argunit', 'm');
169 model.func('an7').set('fununit', '1');
170 model.func('an7').set('plotargs', {'y' '0.0006' '0.001425'});
171 model.component('mod1').func('int3').label('y-Koord-Zeitlauf 1');
172 model.component('mod1').func('int3').set('table', {'0.000000' '0.015000'; ...
173 '1.600000' '4.815000'});
174 model.component('mod1').func('int3').set('argunit', 's');
175 model.component('mod1').func('int3').set('fununit', 'mm');
176 model.func('an8').label('Analytic 3');
177 model.func('an8').set('funcname', 'dotierstoff');
178 model.func('an8').set('expr', '1/2/pi/sigma/sigma*exp(-((a-a0)^2/(2*sigma^2))-((b-b0)^2/(2*sigma
179 model.func('an8').set('args', {'a' 'a0' 'sigma' 'b' 'b0' 'sigma'});
180 model.func('an8').set('argunit', 'm,m,m,m,m');
181 model.func('an8').set('fununit', '1');
182 model.func('an8').set('plotargs', {'a' '-L' 'L'; ...
183 'a0' 'x0' 'x0'; ...

```



```

184 'sigma' 'sigx' 'sigx'; ...
185 'b' '-L' 'L'; ...
186 'b0' 'y0' 'y0'; ...
187 'sigb' 'sigy' 'sigy'});
188 model.func('an9').label('mue');
189 model.func('an9').set('funcname', 'an10');
190 model.func('an9').set('expr', '(88+1323/(1+0.8*10^(-17) *N))');
191 model.func('an9').set('args', {'N'});
192 model.func('an9').set('argunit', 'cm^(-3)');
193 model.func('an9').set('fununit', 'cm^2/V/s');
194 model.func('an9').set('plotargs', {'N' '10^12 [cm^-3]' '10^16 [cm^-3]});
195 model.func('an10').label('muh');
196 model.func('an10').set('funcname', 'an11');
197 model.func('an10').set('expr', '(55+429/(1+0.4*10^(-17) *N))');
198 model.func('an10').set('args', {'N'});
199 model.func('an10').set('argunit', 'cm^(-3)');
200 model.func('an10').set('fununit', 'cm^2/V/s');
201 model.func('an10').set('plotargs', {'N' '10^18' '10^26'});
202 model.component('mod1').func('an12').set('funcname', 'an13');
203 model.component('mod1').func('an12').set('expr', 'step1(x)');
204 model.component('mod1').func('an12').set('argunit', 'm');
205 model.component('mod1').func('an12').set('fununit', '1/m');
206 model.component('mod1').func('an12').set('plotargs', {'x' '-1e-6' '1e-6'});
207 model.component('mod1').func('step1').set('from', 1);
208 model.component('mod1').func('step1').set('to', 0);
209 model.component('mod1').func('step1').set('smooth', 0.01);
210 model.func('wv1').set('type', 'square');
211 model.func('wv1').set('smooth', 0.2);
212 model.func('wv1').set('freq', '2*pi');
213 model.func('wv1').set('phase', 'pi/2');
214 model.func('wv2').set('freq', '2*pi*1000');
215 model.component('mod1').func('an13').label('Analytic 14');
216 model.component('mod1').func('an13').set('funcname', 'an14');
217 model.component('mod1').func('an13').set('expr', '(exp(-(x-x1)/s1)^2+exp(-(x-x2)/s2)^2)
/1.2+exp(-(x-x3)/s3)^2)/2./2.05');
218 model.component('mod1').func('an13').set('args', {'x' 'x1' 'x2' 'x3' 's1' 's2' 's3'});
219 model.component('mod1').func('an13').set('argunit', 'm,m,m,m,m,m,m');
220 model.component('mod1').func('an13').set('plotargs', {'x' '0' '1E-5'; ...
221 'x1' 'z1' 'z1'; ...
222 'x2' 'z2' 'z2'; ...
223 'x3' 'z3' 'z3'; ...
224 's1' 's11' 's11'; ...
225 's2' 's12' 's12'; ...
226 's3' 's13' 's13'});
227 model.func('an14').label('for Mesh');
228 model.func('an14').set('funcname', 'an19');
229 model.func('an14').set('expr', 'sqrt(1/2/pi)/d0*exp(-((y-y02)^2/(2*d0^2)))');
230 model.func('an14').set('args', {'y'});
231 model.func('an14').set('argunit', 'm');
232 model.func('an14').set('plotargs', {'y' '0' '3E-3'});
233
234 model.component('mod1').mesh.create('mesh3');
235
236 model.component('mod1').geom('geom1').label('Geometry 1');
237 model.component('mod1').geom('geom1').geomRep('comsol');
238 model.component('mod1').geom('geom1').repairTolType('relative');
239 model.component('mod1').geom('geom1').create('blk1', 'Block');
240 model.component('mod1').geom('geom1').feature('blk1').label('Block 1');
241 model.component('mod1').geom('geom1').feature('blk1').set('pos', {'B/2' 'L/2' '-Lz/2'});
242 model.component('mod1').geom('geom1').feature('blk1').set('base', 'center');
243 model.component('mod1').geom('geom1').feature('blk1').set('size', {'B' 'L' 'Lz'});
244 model.component('mod1').geom('geom1').feature('blk1').set('layername', {'Layer 1'});
245 model.component('mod1').geom('geom1').feature('blk1').set('layer', []);
246 model.component('mod1').geom('geom1').create('poll', 'Polygon');
247 model.component('mod1').geom('geom1').feature('poll').set('source', 'table');
248 model.component('mod1').geom('geom1').feature('poll').set('table', {'0' '0' '0'; '0' 'L' '0'})
;
249 model.component('mod1').geom('geom1').create('pol2', 'Polygon');
250 model.component('mod1').geom('geom1').feature('pol2').active(false);
251 model.component('mod1').geom('geom1').feature('pol2').set('source', 'table');
252 model.component('mod1').geom('geom1').feature('pol2').set('table', {'-B/2' '0.65*L' '0'; 'B/2'
'0.65*L' '0'});
253 model.component('mod1').geom('geom1').create('pt1', 'Point');
254 model.component('mod1').geom('geom1').feature('pt1').label('Point 1');

```

```

255 model.component('mod1').geom('geom1').feature('pt1').set('p', {'0' 'y02' '0'});
256 model.component('mod1').geom('geom1').feature('fin').label('Form Union');
257 model.component('mod1').geom('geom1').feature('fin').set('repairtoltype', 'relative');
258 model.component('mod1').geom('geom1').run;
259 model.component('mod1').geom('geom1').run('fin');
260
261 model.variable.create('var2');
262 model.variable('var2').set('BorGef', 'Bor0a-Bor0b/2+y*Bor0b/L', 'basic Bor + y*gradient');
263 model.variable('var2').set('BorSin', '0*DeltaBor*(fluct)', 'Bor fluctuation');
264 model.variable('var2').set('BorTotal', 'BorGef + BorSin', 'Bor total');
265 model.variable('var2').set('ElAnf', 'ni*ni/BorTotal', 'initial electron (not used)');
266 model.variable('var2').set('x01', '0[mm]');
267 model.variable('var2').set('y01', '0.325[mm]');
268 model.variable('var2').set('PhiFokus', 'Phi*focus(x,x01,sigx,y,y01,sigy)', 'for post-
processing');
269 model.variable('var2').set('fluct', 'sin(sinusFaktor*2*pi*(y-L/2))', 'fluctuation');
270 model.variable('var2').set('fluct2', '0*sin(sinusFaktor/1.7*2*pi*(y-0.000015[m]))+sin(
sinusFaktor/2.2*2*pi*(y-0.000015[m]))+sin(sinusFaktor/3.1*2*pi*(y-0.000015[m]))+sin(
sinusFaktor/1.4*2*pi*(y-0.000015[m]))', 'fluctuation2');
271 model.variable('var2').set('mue0', 'an10(Bor0a)');
272 model.variable('var2').set('muh0', 'an11(Bor0a)');
273 model.variable('var2').set('sig1', 'mue0*Bor0a*q');
274 model.variable('var2').set('sig2', 'muh0*ni^2/Bor0a*q');
275 model.variable('var2').set('rho0', '1/(sig1+sig2)');
276 model.variable('var2').set('Geh', 'Ac*Phi_focus*exp(-Ac*abs(z))');
277 model.variable('var2').set('Phi_focus', 'Phi/2/pi/sigx/sigy*focus(x,x02,sigx,y,y02,sigy)');
278 model.component('mod1').variable.create('var3');
279 model.component('mod1').variable('var3').set('x02', '0.0');
280 model.component('mod1').variable('var3').set('y02', '0.00[mm] + velo*tschritt');
281 model.component('mod1').variable('var3').set('switch', 'pwl(t)');
282 model.component('mod1').variable('var3').set('Q_in', 'P0*(1-Rc)*Ac*(1/(pi*sigx*sigy))*focus(x,
x01,sigx,y,y01,sigy)*exp(-Ac*abs(z))', 'for heat source');
283 model.component('mod1').variable('var3').set('Phi_focus', 'Phi/2/pi/sigx/sigy*focus(x,x02,sigx
,y,y02,sigy)');
284 model.component('mod1').variable('var3').set('Phi_focus_graph', 'Phi/2/pi/sigx/sigy*focus(x,
x02,sigx,y,y02,sigy)');
285 model.component('mod1').variable('var3').set('Geh', 'Ac*Phi_focus*exp(-Ac*abs(z))');
286 model.component('mod1').variable('var3').set('max_gauss', 'dotierstoff(x2,x2,gauss_dia,y2,y2,
gauss_dia)');
287 model.component('mod1').variable('var3').set('switsch', '-1*z-IE-7[m]');
288 model.component('mod1').variable('var3').set('switsch2', 'an13(switsch)');
289
290 model.view.create('view2', 3);
291 model.view.create('view3', 3);
292 model.view.create('view4', 3);
293 model.view.create('view5', 2);
294 model.view.create('view6', 3);
295
296 model.component('mod1').material.create('mat1', 'Common');
297 model.component('mod1').material('mat1').propertyGroup.create('AroraMobilityModel', 'Arora
mobility model');
298 model.component('mod1').material('mat1').propertyGroup.create('PowerLawMobilityModel', 'Power
law mobility model');
299 model.component('mod1').material('mat1').propertyGroup.create('Auger', 'Auger recombination');
300 model.component('mod1').material('mat1').propertyGroup.create('Direct', 'Direct recombination'
);
301 model.component('mod1').material('mat1').propertyGroup.create('SRH', 'Shockley-Read-Hall
recombination');
302 model.component('mod1').material('mat1').propertyGroup.create('FletcherMobilityModel', '
Fletcher mobility model');
303 model.component('mod1').material('mat1').propertyGroup.create('CaugheyThomasMobilityModel', '
Caughey-Thomas mobility model');
304 model.component('mod1').material('mat1').propertyGroup.create('SemicondMaterial', '
Semiconductor material');
305 model.component('mod1').material('mat1').propertyGroup.create('LombardiSurfaceMobilityModel',
'Lombardi surface mobility model');
306 model.component('mod1').material('mat1').propertyGroup.create('ImpactIonization', 'Impact
ionization');
307 model.component('mod1').material('mat1').propertyGroup.create('SlotboomModel', 'Slotboom model
');
308 model.component('mod1').material('mat1').propertyGroup.create('JainRoulstonModel', 'Jain-
Roulston model');
309 model.component('mod1').material('mat1').propertyGroup.create('RefractiveIndex', 'Refractive
index');

```

```

310
311 model.component('mod1').cpl.create('intop1', 'Integration');
312 model.component('mod1').cpl.create('aveop1', 'Average');
313 model.component('mod1').cpl.create('aveop2', 'Average');
314 model.component('mod1').cpl('intop1').selection.geom('geom1', 2);
315 model.component('mod1').cpl('intop1').selection.set([5]);
316 model.component('mod1').cpl('aveop1').selection.geom('geom1', 2);
317 model.component('mod1').cpl('aveop1').selection.set([2]);
318 model.component('mod1').cpl('aveop2').selection.geom('geom1', 2);
319 model.component('mod1').cpl('aveop2').selection.set([5]);
320
321 model.component('mod1').physics.create('semi2', 'Semiconductor', 'geom1');
322 model.component('mod1').physics('semi2').identifier('semi2');
323 model.component('mod1').physics('semi2').field('electricpotential').field('V2');
324 model.component('mod1').physics('semi2').field('numberdensity_n').field('Ne2');
325 model.component('mod1').physics('semi2').field('numberdensity_p').field('Ph2');
326 model.component('mod1').physics('semi2').feature('smml').create('mmar1', 'AroraMobilityModel',
3);
327 model.component('mod1').physics('semi2').feature('smml').create('mmfl1', '
FletcherMobilityModel', 3);
328 model.component('mod1').physics('semi2').create('adml', 'AnalyticDopingModel', 3);
329 model.component('mod1').physics('semi2').feature('adml').selection.all;
330 model.component('mod1').physics('semi2').create('disc1', 'Discretization', -1);
331 model.component('mod1').physics('semi2').create('aur1', 'AURRecombination', 3);
332 model.component('mod1').physics('semi2').feature('aur1').selection.set([1]);
333 model.component('mod1').physics('semi2').create('udg1', 'UDGeneration', 3);
334 model.component('mod1').physics('semi2').feature('udg1').selection.all;
335 model.component('mod1').physics('semi2').create('tar1', 'TrapAssistedRecombination', 3);
336 model.component('mod1').physics('semi2').feature('tar1').selection.all;
337 model.component('mod1').physics('semi2').create('mcl', 'MetalContact', 2);
338 model.component('mod1').physics('semi2').physics('semi2').feature('mcl').selection.set([2]);
339 model.component('mod1').physics('semi2').create('mc2', 'MetalContact', 2);
340 model.component('mod1').physics('semi2').feature('mc2').selection.set([5]);
341 model.component('mod1').physics('semi2').create('udr1', 'UDRecombination', 3);
342 model.component('mod1').physics('semi2').feature('udr1').selection.all;
343 model.component('mod1').physics('semi2').create('dir1', 'DIRRecombination', 3);
344 model.component('mod1').physics('semi2').feature('dir1').selection.all;
345
346 model.component('mod1').mesh('mesh3').create('ftri1', 'FreeTri');
347 model.component('mod1').mesh('mesh3').create('swel', 'Sweep');
348 model.component('mod1').mesh('mesh3').feature('ftri1').selection.set([4]);
349 model.component('mod1').mesh('mesh3').feature('swel').create('dis1', 'Distribution');
350
351 model.capeopen.label('Thermodynamik-Paket');
352
353 model.variable('var2').label('Variables 2');
354 model.component('mod1').variable('var3').label('Variables 3');
355
356 model.component('mod1').view('view1').label('View 1');
357 model.component('mod1').view('view1').set('scenelight', false);
358 model.component('mod1').view('view1').light('lgt1').label('Directional Light 1');
359 model.component('mod1').view('view1').light('lgt2').label('Directional Light 2');
360 model.component('mod1').view('view1').light('lgt3').label('Directional Light 3');
361 model.view('view2').label('View 3D 2');
362 model.view('view2').set('locked', true);
363 model.view('view2').axis.label('Axis');
364 model.view('view2').light('lgt1').label('Directional Light 1');
365 model.view('view2').light('lgt2').label('Directional Light 2');
366 model.view('view2').light('lgt3').label('Directional Light 3');
367 model.view('view3').label('View 3D 3');
368 model.view('view3').axis.label('Axis');
369 model.view('view3').light('lgt1').label('Directional Light 1');
370 model.view('view3').light('lgt2').label('Directional Light 2');
371 model.view('view3').light('lgt3').label('Directional Light 3');
372 model.view('view4').label('View 3D 4');
373 model.view('view4').axis.label('Axis');
374 model.view('view4').light('lgt1').label('Directional Light 1');
375 model.view('view4').light('lgt2').label('Directional Light 2');
376 model.view('view4').light('lgt3').label('Directional Light 3');
377 model.view('view5').label('View 2D 5');
378 model.view('view5').axis.label('Axis');
379 model.view('view5').axis.set('xmin', -7.823700434528291E-5);
380 model.view('view5').axis.set('xmax', 2.0453293109312654E-4);
381 model.view('view5').axis.set('ymin', -1.5517087012995034E-4);

```

```

382 model.view('view5').axis.set('ymax', 1.271647197427228E-4);
383 model.view('view6').label('View 3D 6');
384 model.view('view6').axis.label('Axis');
385 model.view('view6').light('lgt1').label('Directional Light 1');
386 model.view('view6').light('lgt2').label('Directional Light 2');
387 model.view('view6').light('lgt3').label('Directional Light 3');
388
389 model.component('mod1').material('mat1').label('Si - Silicon');
390 model.component('mod1').material('mat1').propertyGroup('def').label('Basic');
391 model.component('mod1').material('mat1').propertyGroup('def').set('relpermittivity', {'11.7' '0' '0' '0' '11.7' '0' '0' '0' '11.7'});
392 model.component('mod1').material('mat1').propertyGroup('def').set('thermalconductivity', {'131[W/(m*K)]' '0' '0' '0' '131[W/(m*K)]' '0' '0' '0' '131[W/(m*K)]'});
393 model.component('mod1').material('mat1').propertyGroup('def').set('density', '2329[kg/m^3]');
394 model.component('mod1').material('mat1').propertyGroup('def').set('heatcapacity', '700[J/(kg*K)]');
395 model.component('mod1').material('mat1').propertyGroup('AroraMobilityModel').label('Arora mobility model');
396 model.component('mod1').material('mat1').propertyGroup('AroraMobilityModel').set('mun0_ref_arora', '');
397 model.component('mod1').material('mat1').propertyGroup('AroraMobilityModel').set('mup0_ref_arora', '');
398 model.component('mod1').material('mat1').propertyGroup('AroraMobilityModel').set('mun_min_ref_arora', '');
399 model.component('mod1').material('mat1').propertyGroup('AroraMobilityModel').set('mup_min_ref_arora', '');
400 model.component('mod1').material('mat1').propertyGroup('AroraMobilityModel').set('Nn0_ref_arora', '');
401 model.component('mod1').material('mat1').propertyGroup('AroraMobilityModel').set('Np0_ref_arora', '');
402 model.component('mod1').material('mat1').propertyGroup('AroraMobilityModel').set('alpha0_arora', '');
403 model.component('mod1').material('mat1').propertyGroup('AroraMobilityModel').set('beta1_arora', '');
404 model.component('mod1').material('mat1').propertyGroup('AroraMobilityModel').set('beta2_arora', '');
405 model.component('mod1').material('mat1').propertyGroup('AroraMobilityModel').set('beta3_arora', '');
406 model.component('mod1').material('mat1').propertyGroup('AroraMobilityModel').set('beta4_arora', '');
407 model.component('mod1').material('mat1').propertyGroup('AroraMobilityModel').set('Tref_arora', '');
408 model.component('mod1').material('mat1').propertyGroup('AroraMobilityModel').set('mun0_ref_arora', '1252[cm^2/(V*s)]');
409 model.component('mod1').material('mat1').propertyGroup('AroraMobilityModel').set('mup0_ref_arora', '407[cm^2/(V*s)]');
410 model.component('mod1').material('mat1').propertyGroup('AroraMobilityModel').set('mun_min_ref_arora', '88[cm^2/(V*s)]');
411 model.component('mod1').material('mat1').propertyGroup('AroraMobilityModel').set('mup_min_ref_arora', '54.3[cm^2/(V*s)]');
412 model.component('mod1').material('mat1').propertyGroup('AroraMobilityModel').set('Nn0_ref_arora', '1.26e17[1/cm^3]');
413 model.component('mod1').material('mat1').propertyGroup('AroraMobilityModel').set('Np0_ref_arora', '2.35e17[1/cm^3]');
414 model.component('mod1').material('mat1').propertyGroup('AroraMobilityModel').set('alpha0_arora', '0.88');
415 model.component('mod1').material('mat1').propertyGroup('AroraMobilityModel').set('beta1_arora', '-0.57');
416 model.component('mod1').material('mat1').propertyGroup('AroraMobilityModel').set('beta2_arora', '-2.33');
417 model.component('mod1').material('mat1').propertyGroup('AroraMobilityModel').set('beta3_arora', '-2.33');
418 model.component('mod1').material('mat1').propertyGroup('AroraMobilityModel').set('beta4_arora', '-0.146');
419 model.component('mod1').material('mat1').propertyGroup('AroraMobilityModel').set('Tref_arora', '300[K]');
420 model.component('mod1').material('mat1').propertyGroup('PowerLawMobilityModel').label('Power law mobility model');
421 model.component('mod1').material('mat1').propertyGroup('PowerLawMobilityModel').set('mun0_pl', '');
422 model.component('mod1').material('mat1').propertyGroup('PowerLawMobilityModel').set('mup0_pl', '');
423 model.component('mod1').material('mat1').propertyGroup('PowerLawMobilityModel').set('alphan_pl', '');

```

```

424 model.component('mod1').material('mat1').propertyGroup('PowerLawMobilityModel').set('alphap_pl', '');
425 model.component('mod1').material('mat1').propertyGroup('PowerLawMobilityModel').set('Tref_pl', '');
426 model.component('mod1').material('mat1').propertyGroup('PowerLawMobilityModel').set('mun0_pl', '1448[cm^2/(V*s)]');
427 model.component('mod1').material('mat1').propertyGroup('PowerLawMobilityModel').set('mup0_pl', '473[cm^2/(V*s)]');
428 model.component('mod1').material('mat1').propertyGroup('PowerLawMobilityModel').set('alphap_pl', '2.33');
429 model.component('mod1').material('mat1').propertyGroup('PowerLawMobilityModel').set('alphap_pl', '2.23');
430 model.component('mod1').material('mat1').propertyGroup('PowerLawMobilityModel').set('Tref_pl', '300[K]');
431 model.component('mod1').material('mat1').propertyGroup('Auger').label('Auger recombination');
432 model.component('mod1').material('mat1').propertyGroup('Auger').set('Cn', '');
433 model.component('mod1').material('mat1').propertyGroup('Auger').set('Cp', '');
434 model.component('mod1').material('mat1').propertyGroup('Auger').set('Cn', '2.8e-31[cm^6/s]');
435 model.component('mod1').material('mat1').propertyGroup('Auger').set('Cp', '9.9e-32[cm^6/s]');
436 model.component('mod1').material('mat1').propertyGroup('Direct').label('Direct recombination');
437 model.component('mod1').material('mat1').propertyGroup('Direct').set('C', '1e-20[cm^3/s]');
438 model.component('mod1').material('mat1').propertyGroup('SRH').label('Shockley-Read-Hall recombination');
439 model.component('mod1').material('mat1').propertyGroup('SRH').set('taun', '');
440 model.component('mod1').material('mat1').propertyGroup('SRH').set('taup', '');
441 model.component('mod1').material('mat1').propertyGroup('SRH').set('taun', '10[us]');
442 model.component('mod1').material('mat1').propertyGroup('SRH').set('taup', '10[us]');
443 model.component('mod1').material('mat1').propertyGroup('FletcherMobilityModel').label('Fletcher mobility model');
444 model.component('mod1').material('mat1').propertyGroup('FletcherMobilityModel').set('F1_fl', '');
445 model.component('mod1').material('mat1').propertyGroup('FletcherMobilityModel').set('F2_fl', '');
446 model.component('mod1').material('mat1').propertyGroup('FletcherMobilityModel').set('Tref_fl', '');
447 model.component('mod1').material('mat1').propertyGroup('FletcherMobilityModel').set('F1_fl', '1.04e21[1/(cm^1*V*s)]');
448 model.component('mod1').material('mat1').propertyGroup('FletcherMobilityModel').set('F2_fl', '7.45e13[1/cm^2]');
449 model.component('mod1').material('mat1').propertyGroup('FletcherMobilityModel').set('Tref_fl', '300[K]');
450 model.component('mod1').material('mat1').propertyGroup('CaugheyThomasMobilityModel').label('Caughey-Thomas mobility model');
451 model.component('mod1').material('mat1').propertyGroup('CaugheyThomasMobilityModel').set('alphan0_ct', '');
452 model.component('mod1').material('mat1').propertyGroup('CaugheyThomasMobilityModel').set('alphap0_ct', '');
453 model.component('mod1').material('mat1').propertyGroup('CaugheyThomasMobilityModel').set('vn0_ct', '');
454 model.component('mod1').material('mat1').propertyGroup('CaugheyThomasMobilityModel').set('vp0_ct', '');
455 model.component('mod1').material('mat1').propertyGroup('CaugheyThomasMobilityModel').set('betan1_ct', '');
456 model.component('mod1').material('mat1').propertyGroup('CaugheyThomasMobilityModel').set('betap1_ct', '');
457 model.component('mod1').material('mat1').propertyGroup('CaugheyThomasMobilityModel').set('betan2_ct', '');
458 model.component('mod1').material('mat1').propertyGroup('CaugheyThomasMobilityModel').set('betap2_ct', '');
459 model.component('mod1').material('mat1').propertyGroup('CaugheyThomasMobilityModel').set('Tref_ct', '');
460 model.component('mod1').material('mat1').propertyGroup('CaugheyThomasMobilityModel').set('alphan0_ct', '1.11');
461 model.component('mod1').material('mat1').propertyGroup('CaugheyThomasMobilityModel').set('alphap0_ct', '1.21');
462 model.component('mod1').material('mat1').propertyGroup('CaugheyThomasMobilityModel').set('vn0_ct', '1e7[cm/s]');
463 model.component('mod1').material('mat1').propertyGroup('CaugheyThomasMobilityModel').set('vp0_ct', '8.37e6[cm/s]');
464 model.component('mod1').material('mat1').propertyGroup('CaugheyThomasMobilityModel').set('betan1_ct', '0.66');
465 model.component('mod1').material('mat1').propertyGroup('CaugheyThomasMobilityModel').set('betap1_ct', '0.17');

```

```

466 model.component('mod1').material('mat1').propertyGroup('CaughyThomasMobilityModel').set('
    betan2_ct', '-0.87');
467 model.component('mod1').material('mat1').propertyGroup('CaughyThomasMobilityModel').set('
    betap2_ct', '-0.52');
468 model.component('mod1').material('mat1').propertyGroup('CaughyThomasMobilityModel').set('
    Tref_ct', '300[K]');
469 model.component('mod1').material('mat1').propertyGroup('SemicondMaterial').label('
    Semiconductor material');
470 model.component('mod1').material('mat1').propertyGroup('SemicondMaterial').set('Eg0', '');
471 model.component('mod1').material('mat1').propertyGroup('SemicondMaterial').set('chi0', '');
472 model.component('mod1').material('mat1').propertyGroup('SemicondMaterial').set('Nv', '');
473 model.component('mod1').material('mat1').propertyGroup('SemicondMaterial').set('Nc', '');
474 model.component('mod1').material('mat1').propertyGroup('SemicondMaterial').set('mun', '');
475 model.component('mod1').material('mat1').propertyGroup('SemicondMaterial').set('mup', '');
476 model.component('mod1').material('mat1').propertyGroup('SemicondMaterial').set('Eg0', '1.12[V
    ]');
477 model.component('mod1').material('mat1').propertyGroup('SemicondMaterial').set('chi0', '4.05[V
    ]');
478 model.component('mod1').material('mat1').propertyGroup('SemicondMaterial').set('Nv', '(T/300[K
    ])^{(3/2)}*1.04e19[1/cm^3]');
479 model.component('mod1').material('mat1').propertyGroup('SemicondMaterial').set('Nc', '(T/300[K
    ])^{(3/2)}*2.8e19[1/cm^3]');
480 model.component('mod1').material('mat1').propertyGroup('SemicondMaterial').set('mun', '1450[cm
    ^2/(V*s)]');
481 model.component('mod1').material('mat1').propertyGroup('SemicondMaterial').set('mup', '500[cm
    ^2/(V*s)]');
482 model.component('mod1').material('mat1').propertyGroup('SemicondMaterial').addInput('
    temperature');
483 model.component('mod1').material('mat1').propertyGroup('LombardiSurfaceMobilityModel').label('
    Lombardi surface mobility model');
484 model.component('mod1').material('mat1').propertyGroup('LombardiSurfaceMobilityModel').set('
    deltan_ls', '');
485 model.component('mod1').material('mat1').propertyGroup('LombardiSurfaceMobilityModel').set('
    deltap_ls', '');
486 model.component('mod1').material('mat1').propertyGroup('LombardiSurfaceMobilityModel').set('
    mun1_ls', '');
487 model.component('mod1').material('mat1').propertyGroup('LombardiSurfaceMobilityModel').set('
    mup1_ls', '');
488 model.component('mod1').material('mat1').propertyGroup('LombardiSurfaceMobilityModel').set('
    mun2_ls', '');
489 model.component('mod1').material('mat1').propertyGroup('LombardiSurfaceMobilityModel').set('
    mup2_ls', '');
490 model.component('mod1').material('mat1').propertyGroup('LombardiSurfaceMobilityModel').set('
    alphan_ls', '');
491 model.component('mod1').material('mat1').propertyGroup('LombardiSurfaceMobilityModel').set('
    alphap_ls', '');
492 model.component('mod1').material('mat1').propertyGroup('LombardiSurfaceMobilityModel').set('
    Tref_ls', '');
493 model.component('mod1').material('mat1').propertyGroup('LombardiSurfaceMobilityModel').set('
    Eref_ls', '');
494 model.component('mod1').material('mat1').propertyGroup('LombardiSurfaceMobilityModel').set('
    Nref_ls', '');
495 model.component('mod1').material('mat1').propertyGroup('LombardiSurfaceMobilityModel').set('
    deltan_ls', '5.82e14[V/s]');
496 model.component('mod1').material('mat1').propertyGroup('LombardiSurfaceMobilityModel').set('
    deltap_ls', '2.05e14[V/s]');
497 model.component('mod1').material('mat1').propertyGroup('LombardiSurfaceMobilityModel').set('
    mun1_ls', '4.75e7[cm^2/(V*s)]');
498 model.component('mod1').material('mat1').propertyGroup('LombardiSurfaceMobilityModel').set('
    mup1_ls', '9.93e7[cm^2/(V*s)]');
499 model.component('mod1').material('mat1').propertyGroup('LombardiSurfaceMobilityModel').set('
    mun2_ls', '1.74e5[cm^2/(V*s)]');
500 model.component('mod1').material('mat1').propertyGroup('LombardiSurfaceMobilityModel').set('
    mup2_ls', '8.84e5[cm^2/(V*s)]');
501 model.component('mod1').material('mat1').propertyGroup('LombardiSurfaceMobilityModel').set('
    alphan_ls', '0.125');
502 model.component('mod1').material('mat1').propertyGroup('LombardiSurfaceMobilityModel').set('
    alphap_ls', '0.0317');
503 model.component('mod1').material('mat1').propertyGroup('LombardiSurfaceMobilityModel').set('
    Tref_ls', '1[K]');
504 model.component('mod1').material('mat1').propertyGroup('LombardiSurfaceMobilityModel').set('
    Eref_ls', '1[V/cm]');
505 model.component('mod1').material('mat1').propertyGroup('LombardiSurfaceMobilityModel').set('
    Nref_ls', '1[1/cm^3]');

```

```

506 model.component('modl').material('matl').propertyGroup('ImpactIonization').label('Impact
    ionization');
507 model.component('modl').material('matl').propertyGroup('ImpactIonization').set('an', '');
508 model.component('modl').material('matl').propertyGroup('ImpactIonization').set('ap', '');
509 model.component('modl').material('matl').propertyGroup('ImpactIonization').set('bn', '');
510 model.component('modl').material('matl').propertyGroup('ImpactIonization').set('bp', '');
511 model.component('modl').material('matl').propertyGroup('ImpactIonization').set('cnii', '');
512 model.component('modl').material('matl').propertyGroup('ImpactIonization').set('cpii', '');
513 model.component('modl').material('matl').propertyGroup('ImpactIonization').set('dn', '');
514 model.component('modl').material('matl').propertyGroup('ImpactIonization').set('dp', '');
515 model.component('modl').material('matl').propertyGroup('ImpactIonization').set('an', '0.426');
516 model.component('modl').material('matl').propertyGroup('ImpactIonization').set('ap', '0.243');
517 model.component('modl').material('matl').propertyGroup('ImpactIonization').set('bn', '4.81E5[V
    /cm]');
518 model.component('modl').material('matl').propertyGroup('ImpactIonization').set('bp', '6.53E5[V
    /cm]');
519 model.component('modl').material('matl').propertyGroup('ImpactIonization').set('cnii', '3.05E
    -4');
520 model.component('modl').material('matl').propertyGroup('ImpactIonization').set('cpii', '5.35E
    -4');
521 model.component('modl').material('matl').propertyGroup('ImpactIonization').set('dn', '6.86E-4'
    );
522 model.component('modl').material('matl').propertyGroup('ImpactIonization').set('dp', '5.67E-4'
    );
523 model.component('modl').material('matl').propertyGroup('SlotboomModel').label('Slotboom model'
    );
524 model.component('modl').material('matl').propertyGroup('SlotboomModel').set('Eref_sb', '');
525 model.component('modl').material('matl').propertyGroup('SlotboomModel').set('Nref_sb', '');
526 model.component('modl').material('matl').propertyGroup('SlotboomModel').set('alpha_sb', '');
527 model.component('modl').material('matl').propertyGroup('SlotboomModel').set('Eref_sb', '
    0.00692[V]');
528 model.component('modl').material('matl').propertyGroup('SlotboomModel').set('Nref_sb', '1.3e17
    [1/cm^3]');
529 model.component('modl').material('matl').propertyGroup('SlotboomModel').set('alpha_sb', '0.5')
    ;
530 model.component('modl').material('matl').propertyGroup('JainRoulstonModel').label('Jain-
    Roulston model');
531 model.component('modl').material('matl').propertyGroup('JainRoulstonModel').set('An_jr', '');
532 model.component('modl').material('matl').propertyGroup('JainRoulstonModel').set('Bn_jr', '');
533 model.component('modl').material('matl').propertyGroup('JainRoulstonModel').set('Cn_jr', '');
534 model.component('modl').material('matl').propertyGroup('JainRoulstonModel').set('Ap_jr', '');
535 model.component('modl').material('matl').propertyGroup('JainRoulstonModel').set('Bp_jr', '');
536 model.component('modl').material('matl').propertyGroup('JainRoulstonModel').set('Cp_jr', '');
537 model.component('modl').material('matl').propertyGroup('JainRoulstonModel').set('Nref_jr', '')
    ;
538 model.component('modl').material('matl').propertyGroup('JainRoulstonModel').set('alpha_jr', ''
    );
539 model.component('modl').material('matl').propertyGroup('JainRoulstonModel').set('An_jr', '3.5e
    -8[V]');
540 model.component('modl').material('matl').propertyGroup('JainRoulstonModel').set('Bn_jr', '0[V]
    ');
541 model.component('modl').material('matl').propertyGroup('JainRoulstonModel').set('Cn_jr', '0[V]
    ');
542 model.component('modl').material('matl').propertyGroup('JainRoulstonModel').set('Ap_jr', '3.5e
    -8[V]');
543 model.component('modl').material('matl').propertyGroup('JainRoulstonModel').set('Bp_jr', '0[V]
    ');
544 model.component('modl').material('matl').propertyGroup('JainRoulstonModel').set('Cp_jr', '0[V]
    ');
545 model.component('modl').material('matl').propertyGroup('JainRoulstonModel').set('Nref_jr', '
    1[1/cm^3]');
546 model.component('modl').material('matl').propertyGroup('JainRoulstonModel').set('alpha_jr', '
    0.5');
547 model.component('modl').material('matl').propertyGroup('RefractiveIndex').label('Refractive
    index');
548 model.component('modl').material('matl').propertyGroup('RefractiveIndex').set('n', '');
549 model.component('modl').material('matl').propertyGroup('RefractiveIndex').set('ki', '');
550 model.component('modl').material('matl').propertyGroup('RefractiveIndex').set('n', {'2.222222
    '0' '0' '0' '2.222222' '0' '0' '0' '2.222222'});
551 model.component('modl').material('matl').propertyGroup('RefractiveIndex').set('ki', {'
    3.3333333' '0' '0' '0' '3.3333333' '0' '0' '0' '3.3333333'});
552
553 model.component('modl').cpl('intopl').label('Integration stirnseite ohne vorgabe');
554

```

```

555 model.component('mod1').coordSystem('sys1').label('Boundary System 1');
556
557 model.common('cminpt').label('Common model inputs 1');
558
559 model.component('mod1').physics('semi2').label('Semiconductor 2');
560 model.component('mod1').physics('semi2').prop('ModelProperties').set('CarrierStatistics', '
    FermiDirac');
561 model.component('mod1').physics('semi2').prop('Continuation').set('
    DopingTrapDensityContinuation', 'UserDefined');
562 model.component('mod1').physics('semi2').prop('Continuation').set('cp_dtd_input', 'cp');
563 model.component('mod1').physics('semi2').feature('smml').set('mun', 'an10(semi2.Na+semi2.Nd)')
    ;
564 model.component('mod1').physics('semi2').feature('smml').set('mup', 'an11(semi2.Na+semi2.Nd)')
    ;
565 model.component('mod1').physics('semi2').feature('smml').label('Semiconductor Material Model 1
    ');
566 model.component('mod1').physics('semi2').feature('smml').feature('mmar1').set('mun0_ref_arora'
    , '1323[cm^2/(V*s)]');
567 model.component('mod1').physics('semi2').feature('smml').feature('mmar1').set('mup0_ref_arora'
    , '429[cm^2/(V*s)]');
568 model.component('mod1').physics('semi2').feature('smml').feature('mmar1').set('
    mun_min_ref_arora', '89[cm^2/(V*s)]');
569 model.component('mod1').physics('semi2').feature('smml').feature('mmar1').set('
    mup_min_ref_arora', '55[cm^2/(V*s)]');
570 model.component('mod1').physics('semi2').feature('smml').feature('mmar1').label('Arora
    Mobility Model (LI) 1');
571 model.component('mod1').physics('semi2').feature('smml').feature('mmar1').featureInfo('info').
    label('Equation View');
572 model.component('mod1').physics('semi2').feature('smml').feature('mmfl1').label('Fletcher
    Mobility Model (C) 1');
573 model.component('mod1').physics('semi2').feature('smml').feature('mmfl1').featureInfo('info').
    label('Equation View');
574 model.component('mod1').physics('semi2').feature('smml').featureInfo('info').label('Equation
    View');
575 model.component('mod1').physics('semi2').feature('ins1').label('Insulation 1');
576 model.component('mod1').physics('semi2').feature('ins1').featureInfo('info').label('Equation
    View');
577 model.component('mod1').physics('semi2').feature('zcl').label('Zero Charge 1');
578 model.component('mod1').physics('semi2').feature('zcl').featureInfo('info').label('Equation
    View');
579 model.component('mod1').physics('semi2').feature('iil').label('Insulator Interface 1');
580 model.component('mod1').physics('semi2').feature('iil').featureInfo('info').label('Equation
    View');
581 model.component('mod1').physics('semi2').feature('cont1').label('Continuity/Heterojunction 1')
    ;
582 model.component('mod1').physics('semi2').feature('cont1').featureInfo('info').label('Equation
    View');
583 model.component('mod1').physics('semi2').feature('init1').set('V', 'PotAnf');
584 model.component('mod1').physics('semi2').feature('init1').set('N', 'ElAnf');
585 model.component('mod1').physics('semi2').feature('init1').set('P', 'BorGes');
586 model.component('mod1').physics('semi2').feature('init1').label('Initial Values 1');
587 model.component('mod1').physics('semi2').feature('init1').featureInfo('info').label('Equation
    View');
588 model.component('mod1').physics('semi2').feature('adml').set('NAc', 'BorTotal+an14(abs(z),z1,
    z2,z3,s11,s12,s13)*(3.8E15[1/cm^3])*(rect1((y-y2)/gauss_dia))+Bor0a/1000*vw2(y/1[m]')');
589 model.component('mod1').physics('semi2').feature('adml').set('NDc', 'BorTotal');
590 model.component('mod1').physics('semi2').feature('adml').label('AnalytDopingModel_constant p
    Doping');
591 model.component('mod1').physics('semi2').feature('adml').featureInfo('info').label('Equation
    View');
592 model.component('mod1').physics('semi2').feature('discl').label('Discretization 1');
593 model.component('mod1').physics('semi2').feature('discl').featureInfo('info').label('Equation
    View');
594 model.component('mod1').physics('semi2').feature('aur1').label('Auger Recombination 1');
595 model.component('mod1').physics('semi2').feature('aur1').featureInfo('info').label('Equation
    View');
596 model.component('mod1').physics('semi2').feature('udg1').set('Gn', 'Geh*cp*(1-Rc)');
597 model.component('mod1').physics('semi2').feature('udg1').set('Gp', 'Geh*cp*(1-Rc)');
598 model.component('mod1').physics('semi2').feature('udg1').label('User-Defined Generation 1');
599 model.component('mod1').physics('semi2').feature('udg1').featureInfo('info').label('Equation
    View');
600 model.component('mod1').physics('semi2').feature('tar1').set('Delta_Et', 'semi2.Ei-0.046[V]');
601 model.component('mod1').physics('semi2').feature('tar1').set('taun', 'SRH2*1[ns]');
602 model.component('mod1').physics('semi2').feature('tar1').set('taup', 'SRH2*1[ns]');

```



```

603 model.component('mod1').physics('semi2').feature('tar1').label('Trap-Assisted Recombination
SRH');
604 model.component('mod1').physics('semi2').feature('tar1').featureInfo('info').label('Equation
View');
605 model.component('mod1').physics('semi2').feature('mc1').set('Phi_B', '0.1[V]');
606 model.component('mod1').physics('semi2').feature('mc1').set('V0', 0);
607 model.component('mod1').physics('semi2').feature('mc1').set('V0_init', '0.0[V]');
608 model.component('mod1').physics('semi2').feature('mc1').label('Metal Contact on zero Voltage')
;
609 model.component('mod1').physics('semi2').feature('mc1').featureInfo('info').label('Equation
View');
610 model.component('mod1').physics('semi2').feature('mc2').set('Phi_B', '0.01[V]');
611 model.component('mod1').physics('semi2').feature('mc2').set('TerminalType', 'Circuit');
612 model.component('mod1').physics('semi2').feature('mc2').set('V0', '0.0');
613 model.component('mod1').physics('semi2').feature('mc2').label('Metal Contact Signal_not at
zero Voltage');
614 model.component('mod1').physics('semi2').feature('mc2').featureInfo('info').label('Equation
View');
615 model.component('mod1').physics('semi2').feature('udr1').set('Rn', 'Se*(semi2.N-semi2.n_eq)*
switsch2');
616 model.component('mod1').physics('semi2').feature('udr1').set('Rp', 'Sh*(semi2.P-semi2.p_eq)*
switsch2');
617 model.component('mod1').physics('semi2').feature('dir1').label('Direct Recombination 1');
618 model.component('mod1').physics('semi2').feature('dir1').featureInfo('info').label('Equation
View');
619
620 model.component('mod1').mesh('mesh3').label('Mesh 3');
621 model.component('mod1').mesh('mesh3').feature('size').label('Size');
622 model.component('mod1').mesh('mesh3').feature('size').set('custom', 'on');
623 model.component('mod1').mesh('mesh3').feature('size').set('hmax', 'Size_max*10');
624 model.component('mod1').mesh('mesh3').feature('size').set('hmin', 'Size_min/10000');
625 model.component('mod1').mesh('mesh3').feature('size').set('hgrad', 1.1);
626 model.component('mod1').mesh('mesh3').feature('ftri1').label('Free Triangular 1');
627 model.component('mod1').mesh('mesh3').feature('swel').label('Swept 1');
628 model.component('mod1').mesh('mesh3').feature('swel').feature('dis1').label('Distribution 1');
629 model.component('mod1').mesh('mesh3').feature('swel').feature('dis1').set('type', 'predefined'
);
630 model.component('mod1').mesh('mesh3').feature('swel').feature('dis1').set('elemcount', 22);
631 model.component('mod1').mesh('mesh3').feature('swel').feature('dis1').set('elemratio', 100);
632 model.component('mod1').mesh('mesh3').feature('swel').feature('dis1').set('method', 'geometric
');
633 model.component('mod1').mesh('mesh3').run;
634
635 model.component('mod1').physics('semi2').feature('smml').set('mun_mat', 'root.mod1.semi2.
mun_fl');
636 model.component('mod1').physics('semi2').feature('smml').set('mup_mat', 'root.mod1.semi2.
mup_fl');
637 model.component('mod1').physics('semi2').feature('smml').feature('mmar1').set('
mun0_ref_arora_mat', 'userdef');
638 model.component('mod1').physics('semi2').feature('smml').feature('mmar1').set('
mup0_ref_arora_mat', 'userdef');
639 model.component('mod1').physics('semi2').feature('smml').feature('mmar1').set('
mun_min_ref_arora_mat', 'userdef');
640 model.component('mod1').physics('semi2').feature('smml').feature('mmar1').set('
mup_min_ref_arora_mat', 'userdef');
641 model.component('mod1').physics('semi2').feature('smml').feature('mmar1').set('
Nn0_ref_arora_mat', 'userdef');
642 model.component('mod1').physics('semi2').feature('smml').feature('mmar1').set('
Np0_ref_arora_mat', 'userdef');
643 model.component('mod1').physics('semi2').feature('smml').feature('mmfl1').set('mun_in_src', '
root.mod1.semi2.mun_ar');
644 model.component('mod1').physics('semi2').feature('smml').feature('mmfl1').set('mup_in_src', '
root.mod1.semi2.mup_ar');
645 model.component('mod1').physics('semi2').feature('smml').feature('mmfl1').set('F1_fl_mat', '
userdef');
646 model.component('mod1').physics('semi2').feature('smml').feature('mmfl1').set('F2_fl_mat', '
userdef');
647 model.component('mod1').physics('semi2').feature('smml').feature('mmfl1').set('Tref_fl_mat', '
userdef');
648 model.component('mod1').physics('semi2').feature('tar1').set('taun_mat', 'userdef');
649 model.component('mod1').physics('semi2').feature('tar1').set('taup_mat', 'userdef');
650
651 model.study.create('std15');
652 model.study('std15').create('param', 'Parametric');

```

```

653 model.study('std15').create('stat', 'Stationary');
654 model.study('std15').create('stat2', 'Stationary');
655
656 model.sol.create('sol125');
657 model.sol('sol125').study('std15');
658 model.sol('sol125').label('Parametric Solutions 4');
659
660 model.batch.create('p1', 'Parametric');
661 model.batch('p1').create('sol', 'Solutionseq');
662 model.batch('p1').study('std15');
663
664 model.result.dataset.create('dset9', 'Solution');
665 model.result.dataset.create('c1n12', 'CutLine3D');
666 model.result.dataset('c1n12').set('data', 'dset9');
667 model.result.dataset.remove('dset1');
668 model.result.numerical.create('gevl', 'EvalGlobal');
669 model.result.numerical('gevl').set('probetag', 'none');
670
671 model.study('std15').feature('param').label('Parametric Sweep');
672 model.study('std15').feature('param').set('pname', {'tschritt'});
673 model.study('std15').feature('param').set('plistarr', {'range
(1.35,0.19999999999999996/40,1.55)'});
674 model.study('std15').feature('param').set('punit', {'s'});
675 model.study('std15').feature('stat').set('useparam', true);
676 model.study('std15').feature('stat').set('sweeptype', 'filled');
677 model.study('std15').feature('stat').set('pname', {'praefakt' 'Bor0'});
678 model.study('std15').feature('stat').set('plistarr', {'10,20,48,50,96,100,200,500,560,800,1000
' '1.9E15,6E14,2E14,6.5E13'});
679 model.study('std15').feature('stat').set('punit', {'' '});
680 model.study('std15').feature('stat').set('pcontinuationmode', 'no');
681 model.study('std15').feature('stat').set('preusesol', 'yes');
682 model.study('std15').feature('stat2').active(false);
683 model.study('std15').feature('stat2').label('Stationary 2');
684 model.study('std15').feature('stat2').set('useparam', true);
685 model.study('std15').feature('stat2').set('pname', {'praefakt'});
686 model.study('std15').feature('stat2').set('plistarr', {'100,300,500,700,1000'});
687 model.study('std15').feature('stat2').set('punit', {'' '});
688
689 model.batch('p1').label('Parametric Sweep 1');
690 model.batch('p1').set('pname', {'tschritt'});
691 model.batch('p1').set('plistarr', {'range(1.35,0.19999999999999996/40,1.55)'});
692 model.batch('p1').set('punit', {'s'});
693 model.batch('p1').set('err', true);
694 model.batch('p1').feature('sol').set('store', true);
695 model.batch('p1').feature('sol').set('psol', 'sol125');
696 model.batch('p1').feature('sol').set('param', {'"tschritt", "1.35" ' "tschritt", "1.355" ' "
tschritt", "1.36" ' "tschritt", "1.365" ' "tschritt", "1.37" ' "tschritt", "1.375" ' "tschritt
", "1.38" ' "tschritt", "1.385" ' "tschritt", "1.39" ' "tschritt", "1.395" ' ...
697 "' tschritt ", "1.4" ' "tschritt", "1.405" ' "tschritt", "1.41" ' "tschritt", "1.415" ' "tschritt
", "1.42" ' "tschritt", "1.425" ' "tschritt", "1.43" ' "tschritt", "1.435" ' "tschritt", "1.44"
' ' "tschritt", "1.445" ' ...
698 "' tschritt ", "1.45" ' "tschritt", "1.455" ' "tschritt", "1.46" ' "tschritt", "1.465" ' "tschritt
", "1.47" ' "tschritt", "1.475" ' "tschritt", "1.48" ' "tschritt", "1.485" ' "tschritt", "1.49"
' ' "tschritt", "1.495" ' ...
699 "' tschritt ", "1.5" ' "tschritt", "1.505" ' "tschritt", "1.51" ' "tschritt", "1.515" ' "tschritt
", "1.52" ' "tschritt", "1.525" ' "tschritt", "1.53" ' "tschritt", "1.535" ' "tschritt", "1.54"
' ' "tschritt", "1.545" ' ...
700 "' tschritt ", "1.55" ' });
701 model.batch('p1').attach('std15');
702 model.batch('p1').run;
703
704 model.result.label('Results');
705 model.result.dataset('c1n12').label('Cut Line 3D 12');
706 model.result.dataset('c1n12').set('genpoints', {'0' '1.3[s]*velo' '0'; '0' '1.4[s]*velo' '0'})
;
707 model.result.dataset('c1n12').set('bndsnap', true);
708 model.result.numerical('gevl').set('expr', {'aveop1(V2)-aveop2(V2)' 'Geom*(aveop1(V2)-aveop2(
V2))' 'Bor0a' 'rho' '(y02-y2)^2^(1/2)'});
709 model.result.numerical('gevl').set('unit', {'mV' 'uV' '1/cm^3' ['ohm' '*cm'] 'um'});
710 model.result.numerical('gevl').set('descr', {'' ' ' 'basic Bor-Doping' ' ' ' '});
711
712 out = model;

```